

SANDIA REPORT

SAND2017-7101

Official Use Only • Skysun, LLC Proprietary

Printed July 2017

Mechanical and Optical Performance Evaluation of the Skysun Tensile Ganged Heliostat Concept

Julius Yellowhair (8823), Kenneth M. Armijo (8823), Charles E. Andraka (8823), Jesus D. Ortega (8823), Jim Clair (Skysun, LLC)

Prepared by Julius Yellowhair
Concentrating Solar Technologies
Sandia National Laboratories
Albuquerque, New Mexico 87185-1127

Sandia National Laboratories is a multimission laboratory managed and operated by National Technology and Engineering Solutions of Sandia, LLC, a wholly owned subsidiary of Honeywell International, Inc., for the U.S. Department of Energy's National Nuclear Security Administration under contract DE-NA0003525.

OFFICIAL USE ONLY

May be exempt from public release under the Freedom of Information Act (5 U.S.C. 552), exemption number and category: 4.Commercial/Proprietary

Department of Energy review required before public release.

Name/Org: NSTTF/8823 Date: 07/10/2017

Guidance (if applicable):

Further dissemination authorized to the Department of Energy and DOE contractors only; other requests shall be approved by the originating facility or higher DOE programmatic authority.



Sandia National Laboratories

OFFICIAL USE ONLY

Issued by Sandia National Laboratories, operated for the United States Department of Energy by National Technology and Engineering Solutions of Sandia, LLC.

NOTICE: This report was prepared as an account of work sponsored by an agency of the United States Government. Neither the United States Government, nor any agency thereof, nor any of their employees, nor any of their contractors, subcontractors, or their employees, make any warranty, express or implied, or assume any legal liability or responsibility for the accuracy, completeness, or usefulness of any information, apparatus, product, or process disclosed, or represent that its use would not infringe privately owned rights. Reference herein to any specific commercial product, process, or service by trade name, trademark, manufacturer, or otherwise, does not necessarily constitute or imply its endorsement, recommendation, or favoring by the United States Government, any agency thereof, or any of their contractors or subcontractors. The views and opinions expressed herein do not necessarily state or reflect those of the United States Government, any agency thereof, or any of their contractors.



Mechanical and Optical Performance Evaluation of the Skysun Tensile Ganged Heliostat Concept

Julius Yellowhair, Kenneth M. Armijo, Charles E. Andraka, Jesus D. Ortega

Concentrating Solar Technologies

Sandia National Laboratories, P. O. Box 5800, Albuquerque, New Mexico 87185-1127

Jim Clair

Skysun, LLC, Bay Village, OH 44140

Abstract

Heliostat collector fields in solar power tower plants make up about 40% of the installed plant cost. The main components of these conventional heliostats are the pedestal, frame structure to hold the mirrors, and drives to move the heliostat in azimuth and elevation angles for sun tracking. Reducing the cost on these conventional heliostats to meet the DOE SunShot cost goal of \$75/m² has been a challenge. The main advantage of ganged heliostats is multiple heliostats can be grouped such that the pedestal, drives and other components are shared. This can drastically reduce the number of components and has potential to reduce cost to meet the SunShot goal.

In this work, Sandia evaluated a novel ganged heliostat concept, developed by Skysun, LLC, that uses suspended guide cables to support multiple heliostats. The guide cables are attached to rotational arms, which are anchored to two end posts. Heliostat tracking motions are provided by rotating the rotational arms at both ends and local heliostat pitch angle drives. A small scale prototype system was installed at Sandia for the evaluation for mechanical and optical performance. The main questions to address were the survivability of the suspended system under heavy wind loads, performance in windy conditions, on-sun tracking capability including the tracking accuracy estimate, and cost feasibility.

The lowest natural frequency (side-to-side sway) of the initial prototype installed at Sandia measured around 1 Hz for different roll angle orientations of the mirror spans. The first torsional mode measured > 2 Hz in the different roll orientations. For stability in windy conditions, dampening is recommended. Damping locations were identified for optimum stability. Manual on-sun tracking was demonstrated on the small-scale prototype setups. With manual angle adjustments, 4 mrad tracking accuracy was estimated. With improved controls on the angles, the tracking accuracy can be improved by 2-3x. The cost study, although not exhaustive, showed an installed cost of about \$74/m². Further cost reductions with alternative materials may be possible. A 10 MW conceptual power tower model was developed, where the ganged heliostat field was compared to a conventional field. Improving on the blocking efficiency for the ganged heliostat field showed comparable annual optical efficiency compared to a conventional field.

ACKNOWLEDGMENTS

The authors would like to thank Joshua M. Christian and Greg Peacock (student) for their mechanical modeling support, John W. Kelton, Daniel A. Ray, and Benson C. Tso for their mechanical hardware and fabrication and electrical support, and Kenneth P. Nunez and William J. Kolb for assisting with acquiring approvals for installation of the prototype ganged heliostat system on the NSTTF site. The authors also thank Sean Milroy (Skysun, LLC) for engineering support and Adam Halperin (Skysun, LLC) for software support. For support of this research, the authors also thank the Small Business Voucher Pilot Program and the U.S. Department of Energy.

Sandia National Laboratories is a multimission laboratory managed and operated by National Technology and Engineering Solutions of Sandia LLC, a wholly owned subsidiary of Honeywell International Inc. for the U.S. Department of Energy's National Nuclear Security Administration. With main facilities in Albuquerque, N.M., and Livermore, C.A., Sandia has major R&D responsibilities in national security, energy and environmental technologies, and economic competitiveness.

OFFICIAL USE ONLY

TABLE OF CONTENTS

1.	Introduction.....	7
2.	Work Scope.....	10
3.	Small-Scale Prototype Development and Evolution.....	11
3.1.	LCCC Installation (Evaluation by Skysun and NASA GRC)	11
3.2.	Sandia Installation.....	12
3.2.1.	Prototype 1	12
3.2.2.	Prototype 2	13
3.2.3.	Prototype 3	14
4.	Mechanical Analysis.....	16
4.1.	Cable Sag Modeling and Description	16
4.1.1.	Methodology	16
4.1.2.	Modeling Results	19
4.1.3.	Future Work on Cable Modeling	21
4.2.	Modal Analysis	21
4.2.1.	Skysun Small-Scale Prototype Overview and Evaluation	23
4.2.2.	Computational Model.....	29
4.2.3.	Experimental Results	31
4.2.4.	Modeling and Dampening Analysis Results	46
4.2.5.	Discussion	49
4.2.6.	Conclusions and Future Work on Vibrational Studies.....	50
5.	Optical Analysis.....	52
5.1.	10 MWe Power Tower Plant Modeling and Simulation	53
5.2.	Optical Performance Evaluation	57
5.2.1.	Field Configuration for Minimal Blockage with Constraints	62
5.3.	Alternative Field Layouts	63
5.3.1.	Layout Over Actual Terrain	65
5.4.	On-Sun Tracking Evaluation	67
5.5.	Future Work on Tracking Development	72
6.	Cost Analysis of the collector field (Skysun)	74
6.1.	Cost Tables.....	75
6.2.	Heliostat Weight Reduction and Cost Savings	80
7.	Preliminary Commercialization Plan.....	82
8.	Conclusions.....	85
9.	Future Work.....	87
	References	89
	Appendix 1: Prototype 1 Mode Shapes from Analytical Fits to Experimental Data.....	92

OFFICIAL USE ONLY

ACRONYMS

Abbreviation	Definition
BLS	Bureau of Labor Statistics
CPI	Consumer Price Index
CPV	Concentrating Photovoltaic
CSP	Concentrating Solar Power
DAQ	Data Acquisition
DLR	German Aerospace Center
DNI	Direct Normal Irradiance
DOE	Department of Energy
LCOE	Levelized Cost of Energy (or Electricity)
NEPA	National Environmental Policy Act
NSTTF	National Solar Thermal Test Facility
O&M	Operations and Maintenance
PPI	Producer Price Index
PV	Photovoltaic
SBV	Small Business Voucher
TRL	Technology Readiness Level

1. INTRODUCTION

Concentrating Solar Power (CSP) is a promising technology for producing low-cost, clean energy. It uses thermal energy collected from sunlight to produce clean utility-scale electricity. When coupled with thermal energy storage, it can provide uninterrupted or dispatchable energy. Currently, there is approximately 1.7 GW deployed CSP plants in the U.S. and 4.8 GW worldwide [1]. The main drawback, however, is the large initial capital needed to install and deploy such plants. Thus, wide spread deployment has been limited. To address this, the U.S. Department of Energy (DOE) SunShot initiative started in 2011 placed aggressive techno-economic targets on solar technologies including CSP systems to reach grid parity (with fossil fuel electricity) at \$0.06/kWh levelized cost of energy (LCOE) by 2020 [2], where kWh units is kilowatt-hour. To meet SunShot goals, costs must be reduced and/or performance increased on all subsystems of a CSP plant. The collector field (i.e., heliostat field) subsystem in power tower systems make up about 40% of the installed plant cost [2-4], thus reducing the field cost immediately impacts the LCOE. The SunShot program currently has a heliostat field cost target of \$75/m². Industry has been working to reduce collector cost since, and it has acknowledged this is a challenging cost target. The current heliostat cost has been stated to be between \$120-150/m² using conventional heliostats [5]. Novel and disruptive heliostat concepts are needed to further drive down the cost.

Conventional heliostats use large mirrors mounted on a frame that rotates independently in azimuth and elevation angles to track the sun daily and seasonally [6]. The heliostats reflect and concentrate the sunlight onto a receiver located on a central tower. Each heliostat requires a fixed pedestal, two independent rotational drives for azimuth and elevation tracking, and structures to hold the mirror facets and allow for the angle rotations. Of the collector field cost, the pedestal and rotational drives make up 40-50% of the cost [7]. Designs of conventional heliostats have been varied to reduce cost, improve optical performance or both [8-7]. In one case, reflective mirror area on heliostats have been increased (e.g., > 70 m²) with the goal to reduce the number of pedestals and drives and consequently reduce the cost on those components. The large reflective areas, however, increase torques due to larger mirror weight and wind load impacts. Larger motors and drives must be used to accommodate the higher torques, thus negatively impacting the economic gains. To improve on optical performance, the opposite may be true where the mirror reflective areas are reduced (e.g., < 20 m²) for better control of the heliostat pointing and tracking and less mirror facets to align on the frame. For smaller heliostats, weight and wind loads are reduced, but many more must be added to provide sufficient solar flux at the receiver. Even after these trade-off studies [6-9], there is no clear cost advantage of one heliostat design over other designs.

To address the cost impacts, some ganged heliostat concepts have been proposed [4,10-14]. In ganged heliostat concepts, multiple heliostats are combined such that they share structures and components, particularly the pedestals and rotational drives. The reduced number of pedestals and drives can reduce the overall cost since these make up the majority of the heliostat cost at 40-50%. Several ganged heliostat concepts and designs have been proposed typically utilizing linkages between two actuators and multiple heliostats. Linkages may be flexible steel bar, cables or chains. The German Aerospace Center (DLR) proposed a large ganged facet approach which was initially touted as having potential for 500 m² surface area [9]. In a revised concept, DLR proposed the torque tube heliostat where the mirrors are mounted on a torque tubes to simplify the coupling mechanism for the elevation angle [10]. One coupled configuration can hold multiple mirrors with a 288 m² of reflective surface area. Another grouped heliostat approach is the triangular heliostat pods where six heliostats are mounted on a common pod system with the aim to reduce to reduce

materials and cost [14]. Optimization studies on geometries and field layouts are ongoing. To our knowledge, the different ganged heliostats concepts has not yet been demonstrated or realized for commercial deployment.

The advantage of ganged heliostats is clear in that the cost savings can be realized through the reduction of the components for the same total reflective area. Some of the disadvantages identified and listed are the increased complexity in linkage between actuators and the many heliostats, difficulty in maintaining optical alignment including on-sun tracking (i.e., heliostat normal vectors vary differently), and probable operations and maintenance (O&M) cost increases to maintain the large number of connection points, which is in reference to the linkage type systems. An aimpoint strategy has also been listed as something difficult to implement with ganged mirrors since the normal vectors for each heliostat is different but move as a group.

Skysun, LLC (Skysun) has developed a unique cable-supported, tensile ganged heliostats concept to significantly reduce the heliostat cost by reduction in the number of components and amount of structure needed. Skysun's design concept eliminates individual supporting posts and dual-axis drive units for each heliostat. Flexible members, or steel cable, support many heliostats from 6 and up to 16 heliostats (64 m^2 each) on 125-200 m horizontal cable spans depending on the cable tension constraints and blocking/shading considerations. Flexible member supports are static steel post/foundations. Four single-axis actuators, two at each supporting post manipulate cable tensions and rotational orientation (or roll angle). Additionally, each heliostat employs one single-axis actuator, rotating the heliostat about its neutral axis (or pitch angle). Potential cost benefits through infrastructure reduction are augmented by rapidity of installation and decreased O&M costs could be realized by simplified robotic cleaning. The hybrid ganged heliostat method is new and novel, and as such, has not been previously implemented commercially.

Skysun approached the problem of reducing collector cost first as an economic problem. Positing that since the energy input is free, albeit at low density, the collector field should be as large and inexpensive as possible, initially without regard to optical aberrations or focal distance. This lack of constraint lead to a large tensile-based ganged heliostat, where the heliostat array is similar to a linear Fresnel concentrator array but on a catenary profile and with an additional angle degree-of-freedom in roll motion. The design was inexpensive but suffered from astigmatism and a non-fixed focus. The next step was to solve the optical aberrations and focal plane location problems, and perform an initial assessment of the survivability in high winds. The initial assessments showed that these challenges could be solved economically.

The linear reflective surface array, which can be deformed by cable and heliostat orientation, provides an efficient means to form a large concave collecting surface laying principally horizontally. Reflected incident rays, being non-normal, suffer from astigmatism. Novel deformations of the reflective surfaces eliminate astigmatic aberration. A toric-shaped deformation of the linear reflective strip reduces the size of a chosen astigmatic focus, yielding higher concentrations. Latitudinal and longitudinal deformations maintain focus on a fixed receiver located on the tower. In the ideal, the astigmatic focus is reduced to a point.

Earlier research by Skysun (2009 to 2010) showed that a cost-effective concave concentrator could be tensile-based, but substantial optical aberrations would need to be addressed [11]. Chief among the optical aberrations is the resultant astigmatism from obliquely reflected rays. Tensile methods to eliminate astigmatism were then incorporated. Small-scale prototype models demonstrated that aligning six reflectors, increasing later to 12 reflectors, could be improved with additional adjustments. Further research with the prototype demonstrated that 24 reflectors, controlled by six actuators including vertical actuation of the end cable anchor points, could be

focused to a fixed receiver while eliminating astigmatism. However, Skysun determined that the cost of vertical actuation, requiring two of the six actuators, of the ganged heliostat reflective surface would increase rapidly with increasing scale. Next a method to eliminate the need for vertical actuation was developed. This improvement was demonstrated by the prototype proving that 24 reflectors, controlled by four ganged actuators and one single-axis actuator per reflector, could focus all reflectors to a fixed receiver while eliminating astigmatism. This hybrid style of ganged heliostat implies substantial cost reduction when compared to the current art of heliostats and has potential to achieve the SunShot goal of \$75/m² of collecting field installed cost. In addition to reduced cost, the hybrid ganged heliostat can also orient all panels to be simultaneously parallel with each other and all perpendicular to solar radiation, and maintain this orientation as the sun moves throughout the day. This capability also has applications in photovoltaics (PV), concentrating photovoltaics (CPV) and beam down heliostat field designs.

For any tensile-based and cable suspended structure, stability is usually a concern especially in windy conditions. The tensile-based ganged heliostats, using suspended guide cables, is no exception. The structure stability can be a concern since the individual heliostats are no longer anchored to the ground but supported by guide cables which are suspended by support posts. Here, wind loads can disrupt structural and optical stability, and in some cases may cause oscillations over the cable spans depending on the modal behavior, or frequency response, of the system. Therefore, proper system damping has to be considered to ensure system stability and optimal performance. In addition, for ganged heliostat designs, tracking becomes non-trivial because the number of rotational drives (degrees of freedom) are now limited for multiple heliostats since the grouped heliostat share the motors and drives. Accurate tracking also becomes a challenge. These were addressed as part of this work.

In 2016 SkySun was awarded a DOE Small Business Voucher to receive assistance from Sandia National Laboratories (Sandia) to evaluate and model the tensile ganged heliostat concept. Sandia was tasked with the optical and mechanical modeling of the proposed tensile ganged heliostat concept and developing some understanding on the performance. The main questions we wanted to address in this project were the survivability of the suspended system under wind loads, performance in windy conditions, on-sun tracking capability, and tracking accuracy estimate, and cost feasibility. This report discusses the findings after 11 months of study. To help develop an understanding, SkySun installed their small-scale “Prototype 1” (Figure 2) ganged heliostat at Sandia, which consisted of 21 mirrors, representing heliostats, of size 30.48 cm × 30.48 cm (12 inch × 12 inch) with a cable span of about 9 m (29.5 feet). The 21 mirrors were later replaced with 13 mirrors sized 15.24 cm × 30.48 cm (6 inch × 12 inch) that had independent pitch angle adjustments which became the “Prototype 2” system, which is shown in Figure 3. Both Prototypes 1 and 2 had butted PVC pipes which provided the structural support and spacing between the mirrors. In Prototype 3, the PVC pipes were cut short. In Section 3, the evolution of the prototype systems is further described.

2. WORK SCOPE

The work scope was developed in collaboration with Skysun. The tasks listed below lays out the work plan that was executed during the period of performance from April 2016 to March 2017.

Task 1: Install current prototype system at Sandia

As part of its cost share, Skysun shipped its initial small-scale prototype to Sandia and installed the system at the NSTTF near the rotating platform. This work included developing a work package which includes developing safety protocols for installation and operation, and addressing NEPA requirements.

Task 2: Evaluate the prototype system

Once the small-scale prototype system was installed, Sandia performed various testing including modal and vibrations testing under external loads such as impulse impacts and wind, on-sun tracking testing, tracking accuracy evaluations, and evaluating changes in cable tensions during on-sun tracking experiments. These experiments helped understand the mechanical and optical performance of the prototype system.

Task 3: Develop mechanical, optical models of the ganged heliostat system

Small- and large-scale systems were modeled using mechanical and optical modeling tools. The results from testing the small-scale system were used to validate the models.

Task 4: Optimize system model, and design conceptual >5 MW CSP plant

The modal behavior under external loads was determined, and damping at strategic locations along the heliostat strip was determine that will assist in stabilizing the system. A 10 MW power tower plant was modeled using the large-scale ganged heliostats, and the layout of the ganged heliostats were semi-optimized for high optical field efficiency.

Task 5: Develop cost models and commercialization/manufacturing plan

A cost model was developed by Skysun for a 10 MW plant size to show meeting of the DOE SunShot cost goal for collectors, and the initial commercialization plan was developed.

Deliverables

This report is part of the final deliverable. In addition, the 10 MW plant layout (i.e., collector field) and results of the model were delivered to the Skysun.

The tasks listed in the work plan were addressed during the period of performance. The results are detailed in this report in subsequent sections. Detailed designs of the heliostats, interfaces to the cable, end posts, and interfacing hardware, such as rotations arms, were not addressed in this project. As the system concept matures, the detailed designs will be developed and addressed in future work.

3. SMALL-SCALE PROTOTYPE DEVELOPMENT AND EVOLUTION

In developing an understanding on the performance of the tensile ganged heliostat concept, the small-scale prototype system was iterated on a few times. In this section, the evolution of the prototype system is described.

3.1. LCCC Installation (Evaluation by Skysun and NASA GRC)

The initial small-scale prototype system was installed in 2014 at the Lorain County Community College (LCCC), Elyria, OH, and evaluated through the NASA Adopt a City Program [11]. The system was evaluated by Skysun and a NASA Glenn Research Center (GRC) team headed by Dr. Paul Bartolotta. The program was administered by MAGNET (The Manufacturing Advocacy and Growth Network, Cleveland, Ohio). The prototype (shown in Figure 1) operated over the course of one year in an exterior unprotected environment, and functioned as a demonstrative subsystem of a collecting field. Hardware was not lab certified; sourcing was commercially available off-the-shelf hardware. Baseline findings for the prototype are shown in Table 1 below.

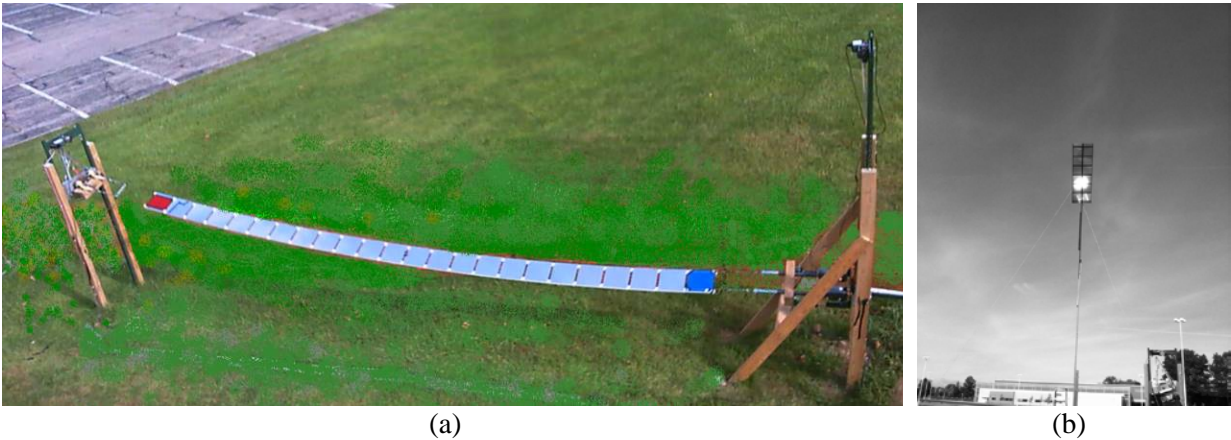


Figure 1. (a) Image of the initial prototype system installed and operated at LCCC campus [June, 2014 to June 2015]. The safety fence was edited out for clarity of the heliostat system. (b) Reflection of the sun from the ganged heliostat onto a flat plate target.

Table1. Skysun, LLC initial prototype characteristics.

Parameter	Value
Heliostat aperture, single flat mirror	0.09 m ²
Heliostats per gang	24
Ganged heliostat aperture	2.1 m ²
Accuracy, winds calm to 15 mph*	4.2 to 9 mrad
Accuracy, wind gusts ~ 33 mph**	37 mrad
Actuators per gang with vertical displacement	6
Actuators per gang: 2 per gang and 1 per heliostat (hybrid)	26
Concentration: ganged aperture/focal area x cosine of zenith angle (max achieved)	14
Gangs per array (geometry of prototype constructed offset – gang to tower implied)	15 to 30
Focal ratio ganged heliostat astigmatism	1.12
Focal ratio array	0.38
Fixed focus maintained, hours post local noon	6.02

*No wind mitigating (e.g., vortex shedding) hardware was employed. Maximum wind gusts of ~66 mph was experienced.

**Accuracy measured geometrically from video of flat plate receiver. Receiver movement during wind gust was substantial, actual accuracy likely greater.

Link to video: http://youtu.be/MTw_jusumKg.

3.2. Sandia Installation

A small-scale prototype (named Prototype 1) was installed at Sandia NSTTF on March 27-28, 2016. The prototype system was then modified twice (i.e., Prototype 2 and 3). The initial prototype and the changes made to the subsequent systems are described below.

3.2.1. Prototype 1

The majority of components comprising Prototype 1 (shown in Figure 2) were the same components from the LCCC prototype described above. The main difference between the LCCC prototype and Prototype 1 at Sandia NSTTF was that the LCCC design was supported by posts set into a foundation (4 inch x 4 inch wood posts in foundation 12 inch diameter by 36 inch deep back-filled with concrete), whereas the NSTTF design used a support structure which was ballasted. Approximately 270 kg (600 lbs.) of weight were used to weigh down the support structure to keep the distance fixed between the support structures, otherwise the structures would get pulled towards each other when the cables were tensioned. The ballasted structure eliminated the need for ground penetration. Additionally, the support structure rested on casters so the system was mobile. A flat-plate receiver was also constructed on site which was about 12 m to the southwest of the prototype system (can be seen in Figure 3).

The installed Prototype 1 system, a hybrid design with four actuators, is shown in Figure 2. On the north end of the heliostat strip, three linear actuators were installed. One actuator (mounted vertically) provided the angular rotation adjustments to the cross beam (also referred to as rotation

arm) which rotated the cable pair providing rotations on the mirrors in the azimuthal direction (for north-south orientation of the heliostat strip) or roll angle. Two actuators were in line with the cables, and these provided tensioning on the cables. On the south end, one actuator was installed which provided rotations to the cross beam, similar to the north-end actuator. For cable tensioning, the cables were attached to two ratchet straps, which provided gross cable tensioning. The cables used were steel cables 3/8 inch diameter. The mirrors (representing heliostats) were attached to 1/2 inch PVC pipes with adhesive which rode over the cables, thus the mirror positions were not fixed to the cables. Prototype 1 allowed for independent pitch adjustments on five of the 21 the mirrors installed. In practice, the prototype system utilizes flat mirrors (12 inch x 12 inch), but are canted through the available actuators: roll actuation on the cables at both ends, pitch actuation on the individual mirrors, and cable tension adjustments with actuators at both ends. Initially the strip is oriented horizontally with the reflective surfaces pointing up. The surface of the strip forms a catenoid. A relatively shallow catenoid approximates a spheroid or paraboloid. At one end of the strip both flexible members terminate to tension actuators. Varying the cable tension in unison changes the focal length of the strip. Varying the tension asymmetrically warps the strip imposing a toric surface contour. The need for vertical displacement of the reflective strip was eliminated with the hybrid design comprising one actuator per reflective panel, and two actuators per ganged heliostat controlling the rotational motions. Cable tensioning adjustment was not necessary while utilizing the hybrid design. However, cable tensioning may be used for improved accuracy. The hybrid design heliostats, implemented in 5 of the 21 facets of the heliostat gang of the prototype, were non-motorized. Typically, 3 of the 5 were utilized - one at each end of the reflective strip and one located near the middle of the strip. A manually adjusted ball/screw mechanism rotates each heliostat about an axis perpendicular to the supporting cables (from coincident with the cables to approximately 60° inclination). The mechanical vibration and modal measurements were performed on this prototype



Figure 2. Image of small-scale Prototype 1 system. The horizontal distance over the cable span was about 9.1 m. The flat-plate receiver is located about 12 m to the right (not seen in the picture).

3.2.2. *Prototype 2*

In Prototype 2 (shown in Figure 3), the 21 mirrors in Prototype 1 were replaced with 13 mirrors by Skysun (on May 16, 2016), each allowing for independent pitch angle control. When the two cables are leveled (i.e., when the rotation arms are at 0° or horizontal), the pitch angles allow the mirrors to move in pure elevation. The pitch angle control consisted of concentric PVC tubes with set screw on the outer tube to lock the angle position. The PVC tubes, which support the mirrors were increased in length to 45.72 cm (18 inch) each increasing the mirror spacing. Individual

mirror size was reduced to 15.24 cm \times 30.48 cm (6 inch \times 12 inch). A removable wind fence was also constructed on site.



Figure 3. Image of Prototype 2 set up with a few mirrors put on-sun and the wind fence (covered with canvas tarp) to the west of the heliostat strip.

3.2.3. *Prototype 3*

In Prototype 3 (shown in Figure 4), the PVC tubes that rode over the cables were cut short, and additional weights were added to the mirrors. In the previous prototypes the PVC tubes were long and butted up against each other. This created the spacing between mirrors. However, two drawbacks were identified with this configuration: 1) The butted-up PVC pipes created a natural dampening effect which impacted the vibration and modal behavior, and 2) for large rotation angles of the rotation arms, the PVC tubes chafed at the contact points sometimes changing the pointing angles of the mirrors (particularly for the mirrors at the bottom of the cable sag) which impacted the on-sun tracking accuracy.

The additional weight added per each mirror was determined from scaling down the 175 m span used in the 10 MWe power tower model. For the 175 m spans, the weight of one heliostat was estimated to be 1500 kg (3,300 lbs.). This included the weight of the glass, back support, and support frame. This was scaled down to 9.4 m span of the prototype set-up arriving at approximately 4 kg (9 lbs.) on each mirror. Previously, the mirrors alone with the PVC tube weighed about 0.5 kg (1 lb.) each. The objective for the modifications in Prototype 3 was to scale the large-scale heliostat concept down to the small-scale prototype system. However, the size of the heliostat (64 m²) was not scaled down. The would have required perhaps custom sized mirrors.

After the modifications, it was observed that the mirror strip became more sensitive, although small, to wind perturbations. That is, increased motions across the cables were observed in light winds. This is further discussed in the mechanical analysis section.



Figure 4. Image of Prototype 3 set-up with another wind fence on the east side.

The Prototype 3 configuration including the target board (flat-plate receiver) was surveyed with a theodolite (CST 302R Total Station). The measurements were incorporated into the SolTrace optical modeling tool. The layout and the flux on the target board are shown in Figure 5.

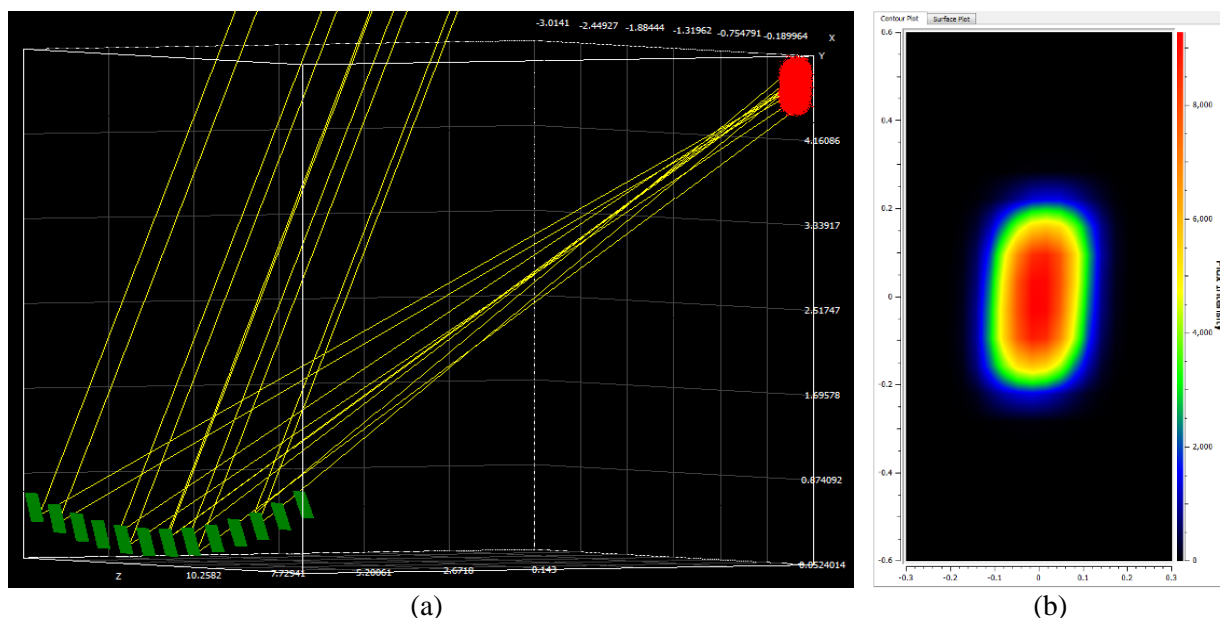


Figure 5. (a) Optical model of Prototype 3 set-up including the (b) fluxmap for Day 40 at solar noon. The fluxmap is showing about 9.5 suns peak and 500 W from the 13 mirrors attached the guide cables (assumes ideal tracking).

The mechanical and optical modeling and analyses on the prototypes installed at Sandia are described in the next sections. In addition, a 10 MW conceptual power tower system is modeled with large-scale ganged heliostats (64 m^2 reflective areas) which is described in the Optical Analysis section (Section 5).

4. MECHANICAL ANALYSIS

In the first section, the cable(s) mechanical behavior is described and Matlab code is developed to model the mechanical behavior. The model (when completed) can then be used to describe the cable profile changes with added weight on the cables including uneven weight distributions on the guide cables and help develop the tracking algorithm for the ganged heliostats. In addition, the model can be used to update the optical model in terms of heliostat catenary profile; initial assumption for the optical models of the field is an ideal catenary profiles.

In the second section, the modal/vibration measurements and the mechanical modeling of the prototype systems are described, and the results are provided.

4.1. Cable Sag Modeling and Description

A free-hanging cable supported at the ends will naturally follow a catenary profile due to gravity. To describe this behavior, custom MATLAB code was developed which incorporates a cable-element methodology presented by Yang, et al. [15]. This methodology presents an enhanced two-node catenary cable element developed for geometric nonlinear analysis of spatial cable-supported structures. The methodology is governed by the following assumptions:

1. Hooke's law is applicable to the cable material.
2. The cable element can undergo a large deformation but the strains are sufficiently small to maintain the section properties unchanged during deformation.
3. The cable element is perfectly flexible and can only undergo a pulling force but not pushing forces or bending moments.
4. Every cable element is of small sag of span

The Matlab code allows the computation of the profile of the heliostat array based on the heliostat distribution on the guide cables, and can determine the heliostat surface normal vectors based on its position on the guide cables. Currently, a single cable with two end supports, which are considered fixed. However, this problem is not considered to be statically indeterminate. Commonly, catenary equations would be used to compute the cable profiles but the equations are limited only to consider the uniform weight of the cable only. This approach was developed and described below with considerations to the uneven heliostat distribution cases. In future studies, the two cables will be incorporated to study the impact of the differential rotations, on one or both of the ends, on the heliostat profile.

4.1.1. Methodology

Figure 6 shows the description of the cable element with its respective reaction nodal forces. The element is defined by two nodes with an element described by the catenary equations instead of a rigid truss or beam.

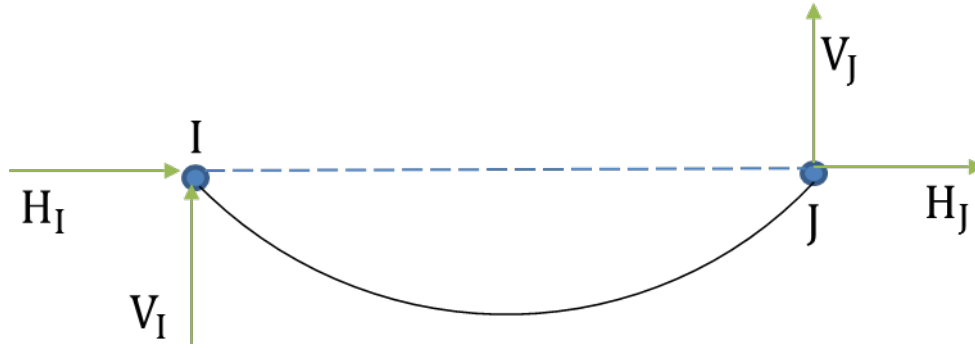


Figure 6. Nodal forces of cable element.

The first step is to define the natural shape of the cable under its own weight. This requires knowledge of two of the three elements depicted in Figure 7. The sag, h , is measured from the horizontal line connecting the end points to the lowest point on the cable, while the cable length, l , is measured when it is unstressed. Typically, by maintaining the span, s , and the span-to-sag ratio (s/h) constant, the length of the cable required for the heliostat array can be determined using the catenary equations.

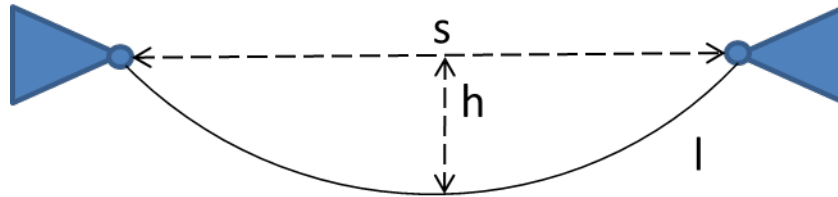


Figure 7. A free-hanging cable element showing the horizontal distance, or span, (s), the sag (h), and the cable length (l).

The catenary equations are a series of hyperbolic equations which describe a hyperbola that is sufficiently far away from the x -axis on an xy -plane, where the x -axis is the horizontal axis. Equations 1 and 2 are used to calculate the cable length and the cable sag as a function of the horizontal position. Note that the parameter c can be computed numerically if h and s are known through measurement or priori.

$$l = c * \sinh\left(\frac{s}{2c}\right) \quad (1)$$

$$h = c * \cosh\left(\frac{s}{2c}\right) - c \quad (2)$$

The second step is to discretize the cable by placing nodes in the locations where forces are applied. The position of the nodes is initially a function of the natural shape of the cable, but they will vary as the model iterates to find its stressed profile. Figure 8 shows an example of the nodes representing forces located along the curve. For our work, each heliostat was taken as a point load along the cable.

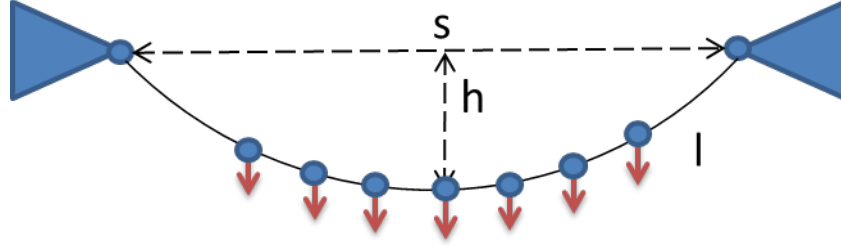


Figure 8. Uniform distribution of seven forces (red arrows) along the cable with a large gap from the end points to the first heliostat, representing the small-scale prototype set up.

The third step is to let the code iterate to calculate the taut cable length and sag as shown in Figure 9. The property matrix is created and derived from the virtual work increment equation of the updated Lagrangian formulation using the catenary equations. The formulation and matrices maintain a similar shape as the truss-beam element formulation as shown in Equations 3 to 5. The variables notation is defined in the appendix in Yang, et al. [15].

$$[k_0] = \frac{EA}{L} \begin{bmatrix} \alpha_1 & 0 & 0 & -\alpha_1 & 0 & 0 \\ & 0 & 0 & 0 & 0 & 0 \\ & & \alpha_2 & 0 & 0 & -\alpha_2 \\ & sym & & \alpha_1 & 0 & 0 \\ & & & & 0 & 0 \\ & & & & & \alpha_2 \end{bmatrix}$$

$$[k_\sigma] = \frac{T_N}{L} \begin{bmatrix} \alpha_3 & 0 & 0 & -\alpha_3 & 0 & 0 \\ & 1 & 0 & 0 & -1 & 0 \\ & & 1 & 0 & 0 & -1 \\ & sym & & \alpha_3 & 0 & 0 \\ & & & & 1 & 0 \\ & & & & & 1 \end{bmatrix} \quad (3)$$

$$[K] = \sum_n [R_1][k_e][R_1] = \sum_n [R_1][k_0 + k_\sigma][R_1] \quad (4)$$

$$[K]\{U\} = {}^{T+\Delta T}\{F\} + {}^T\{\psi\} \quad (5)$$

The fourth and last step is to use the deformed profile (i.e., orange nodes in Figure 9) to determine the heliostat surface normal vectors (green arrows) as shown in Figure 10. These heliostat normal vectors will be used as the initial position of the mirrors in an array. The heliostats pointing angle can then be adjusted to the required position in the aiming strategy section.

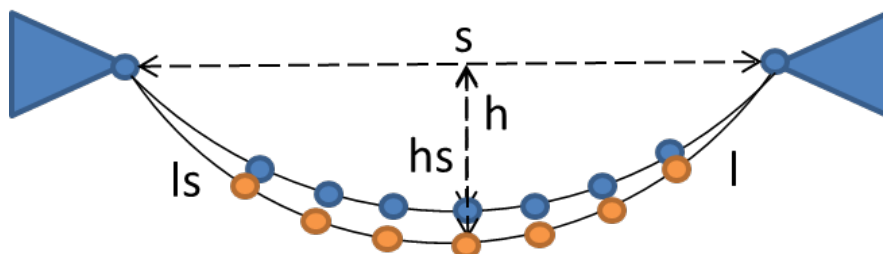


Figure 9. The horizontal distance, or span (s), the unstressed sag (h), the stressed sag (hs), the cable length (l), and the stressed cable length (ls).

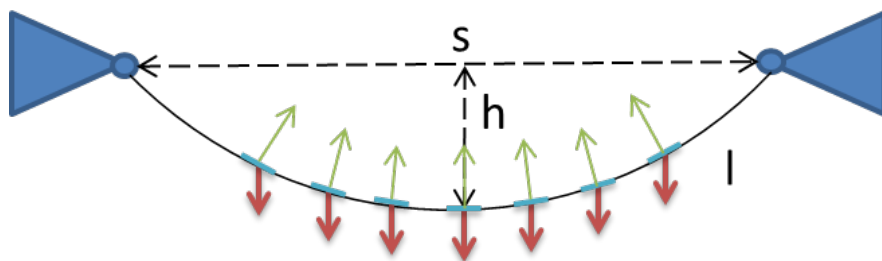


Figure 10. The slope of the points in the deflected shape is used to compute the heliostat surface normal vectors of the mirrors as they would sit in their initial position.

4.1.2. Modeling Results

A scaled-down prototype was installed at the Sandia, and the cable profiles with 13 mirrors attached were measured and compared to the profiles computed analytically. The weight of each facet is approximately 30 N (~3 kg) which is divided in half assuming the weight is supported by two guide cables. The results obtained from the code shown in Figure 11 are compared to the measured positions in the prototype. The calculated cable profile matches the measured profile with an average difference of ~2.5%. Thus the calculated results agree with the measured values very well. The positions of the mirrors were measured two times with the theodolite. The measurement uncertainty in the mirror positions is < 1 mm. The targets (masking tape with a mark on it) placed on the sides of the mirrors were placed to within ± 1 mm of the center point. Table 2 shows the two-dimensional surface normal components along the catenary profile at nodes 1-13.

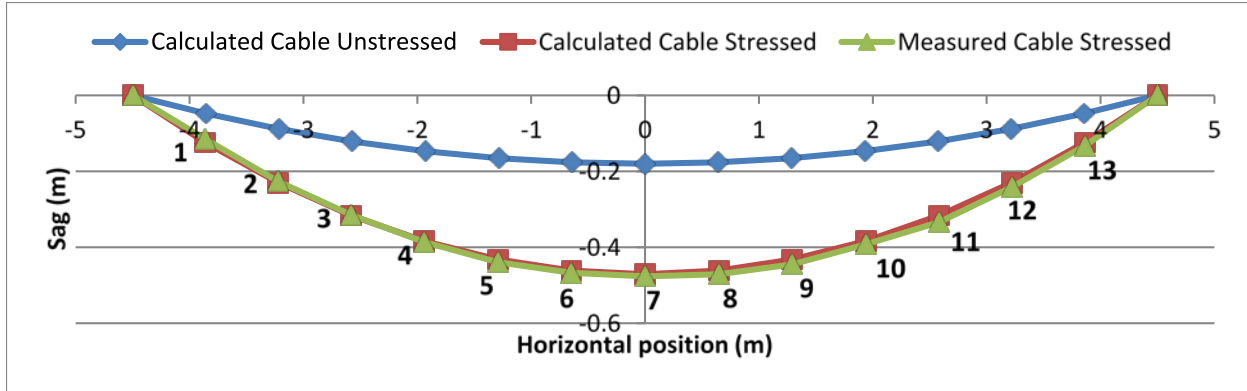


Figure 11. Profile for a uniform heliostat distribution across the guide cables. The blue profile represents the calculated cable profile with no external loads. The red profile represents the calculated cable profile with external loads of 15 N. The green profile represents the measured cable profile with external loads of 15 N.

Table 2. Surface normal components for heliostats on uniform distribution array. Reference to Figure 11.

Node #	\hat{N}_x	\hat{N}_z
1	0.164	0.986
2	0.146	0.989
3	0.122	0.993
4	0.093	0.996
5	0.063	0.998
6	0.031	1.000
7	0.000	1.000
8	-0.030	1.000
9	-0.060	0.998
10	-0.090	0.996
11	-0.122	0.993
12	-0.158	0.988
13	-0.202	0.979

Figure 12 shows the profiles of the cable with non-uniform point loads. Unfortunately, as the writing of this report we had not measured a profile on the prototype with an uneven weight distribution using the theodolite. Nonetheless, the cable profile for uniform weight distribution shown in Figure 11 validates the MATLAB code used. For the non-uniform weight distribution case, the shift can be observed (from the calculated model) towards the left as the heliostats are shifted in the same direction. The uneven heliostat distribution comes about from optimizing the field layout, which is described in the optical analysis section.

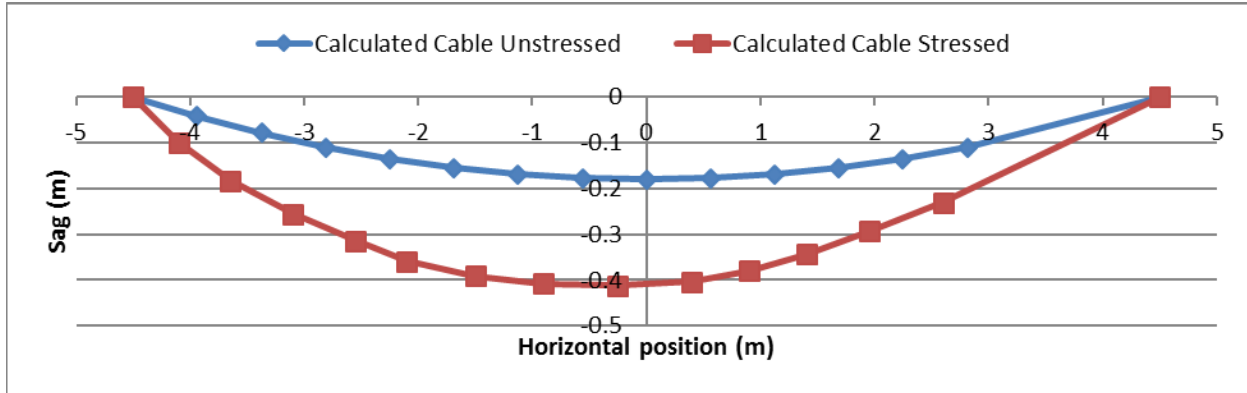


Figure 12. Profile for a non-uniform heliostat distribution. The blue profile represents the calculated cable profile with no external loads. The red profile represents the calculated cable profile with external loads of 15 N at each point load.

4.1.3. Future Work on Cable Modeling

The model we developed is simplified for a single cable case. Modeling two cables and their interactions proved to be challenging which is left for future study and development. The one-cable model developed here assumed that end supports are fixed, whereas the two-cable model will have their end points non-fixed and can influence each other. Initially the weight will be uniformly distributed in both cables. For future study, the topics listed below can be addressed further and incorporated into the model developed so far. These topics were outside the scope of the current work.

- Interaction of both support cables interconnected
 - This will allow us to incorporate rotations and differential tensioning to adjust the heliostat aiming.
- Account for the rotations in the mirror array
 - Rotations on the supports are required to move though out the day, however, this motion is complex to model.
- Account for differential tensioning in the mirror array
 - Differential tensioning of the cables will provide an extra degree of freedom to adjust the heliostat array throughout the day.
- Account for the elevation changes on the individual heliostats
 - The elevation of the heliostats will provide an extra force due to the wind pressure.
- Coupling with the optical analysis
 - This will couple the heliostat array deformation based on non-uniform heliostat distributions that are optimal for optical performance.

4.2. Modal Analysis

Suspension cable systems are used as structural elements in various contexts at various scales and are often prone to quite large transverse loads that can induce vibrations due to their low inherent damping. Structural analyses of cabled bridges have had much research performed to determine impacts of loading on stress distributions. Traditionally catenary formulations have been applied to cabled structures which were often applied to bridge structures that were meant to be oriented

horizontally, with distributed, no-point external loads. However, for the ganged heliostat concept these types of formulations do not apply considering angular movements that are necessary during solar tracking, which induce non-linear loading, and stress distributions throughout the cable structures and heliostats. Additionally, the discrete loading of large heliostats impacts the non-uniformity of the load distribution across the ganged-heliostat system, which can also impact utility of traditional structural methodologies for assessing cable dynamics, especially with regard to vibrational excitation and dampening. This investigation explores the impacts of vibrational impacts using non-linear computational methods for assessing structural loads and system dampening.

Cable dynamics can be complex and has attracted extensive research, especially regarding the effects of geometric nonlinearities, as reviewed by Nayfeh and Pai [16], Rega [17-18] and Ibraim [19]. The dynamic behavior of cables is greatly influenced by the static sag, as addressed by Irvine and Caughey [20] and quantified by Irvine's parameter λ^2 , whereby the sag increases the natural frequencies in the plane of the sag (in-plane) relative to those of a taut cable in the out-of-plane direction. Additionally, ganged heliostat cables can be prone to potentially damaging large amplitude vibrations due to wind loads. As an example, the Tacoma Narrows Bridge collapsed due to wind loads that induced a 0.2 Hz torsional oscillation, with wind speeds up to approximately 80 km/h (50 mph) [21]. The bridge was originally designed to withstand 161 km/h (100 mph) wind provided that the oscillation would have been longitudinal. However, since unexpected torsional oscillations appeared, this considerably lowered the critical speed of the wind. Therefore, it is important to assess a wide variety of mode shapes and oscillatory motions during analysis to develop a comprehensive perspective of potentially damaging vibrations from wind. The dynamic excitation may be from external loading or motions of the rotations arms that the cables are attached to, the latter including direct excitation, normally from components of end motion transverse to the cable, and parametric excitation induced by axial components of end motion causing dynamic tension variations [22]. Geometric nonlinearity can be important, causing stiffening behavior and nonlinear modal coupling. For ganged heliostat cable assemblies with small sag values, the natural frequencies can be close to a harmonic series. Therefore, for primary parametric excitation of any one mode, at twice its natural frequency, the excitation frequency is close to the natural frequency of another mode. Therefore, inputs at an angle to the cable axis (e.g., vertical end motion to an inclined cable) can cause simultaneous direct excitation and parametric excitation of at least two modes, which are nonlinearly coupled [23]. The response of the directly excited mode can modify the dynamic stability and response amplitudes of other modes. These modal excitations, particularly under angled conditions, can impact cable stability where induced vibrations can be quite destructive. The vibrations induced from wind loads can increase substantially with intermittent gusts and wind speed, where a central aim of this paper is to provide an assessment of a ganged heliostat system to provide damaging natural frequency modes based on varying wind speed, cable-structure rotation and facet loading. Additionally, this paper will consider experimentally, multiple excitations in vertical, horizontal and torsional modes to determine potentially destructive excitation motions and frequencies.

The employment of ganged heliostat has been shown to decrease the number of drives and components to reduce costs [10]. However, the tensile-based ganged heliostats concept can be subject to oscillation and vibration affects from wind loads that can facilitate performance losses as well as structural damage. In a study by Moya et al. [24] the impacts of dynamic wind loads and vibration on traditional two-axis mounted heliostats were assessed. The investigators found that the majority of modes excited in a windy environment were under 10 Hz with two low

frequency rigid body modes related to the azimuth and elevation motors. Their results enabled improved designs for the heliostats studied to mitigate the impacts of dynamic wind loads on structural fatigue and optical performance. Similarly, in this investigation assessment of dynamic modal vibrational impacts on ganged heliostats will be conducted to optimize the design for reliable operation. Here, it is important to study vibrational effects, where even small local displacements on the order of a few millimeters, may cause the reflected beam to travel distances that are orders of magnitude larger to reach its target, potentially facilitating significant offsets or flux spillage. This vibration induced error can lead to non-optimized system optics as the aim point of the heliostat can be spread across its intended centroid on the receiver reducing the maximum flux. Additionally, wind induced vibration not only leads to reduced optical performance, but can also lead to structural damage as well. Additionally, although the linear [20] and nonlinear dynamics [17] of suspended elastic cables have been widely investigated, due to their extensive use in engineering design, few studies have ever considered rotated cable vibrational motions, particularly for solar energy applications. This work provides a novel approach to heliostat design which however can be susceptible to oscillation damage at particular frequencies. This research investigated dynamic vibrational modes through the study of the natural frequencies and mode shapes of a small-scale prototype ganged-heliostat system.

Performance under wind loads need to be carefully considered since they affect structural stability and optical performance. To address wind load stability challenges, performance degradation due to wind loads can be mitigated by adding vortex shedding, wind fences, or utilization of a windward outer array as wind block. Other examples of wind mitigating devices such as movement limiting cables/tie-downs and stop posts will also be explored. In this work, we looked only at wind fences and stop posts which showed inconclusive results and will need further study in the future.

4.2.1. Skysun Small-Scale Prototype Overview and Evaluation

Modal tests were conducted on three ganged heliostat prototype configurations installed at the NSTTF to evaluate their unique optical-mechanical design characteristics and examine how various modes of vibration may be excited during wind events. Here, mechanical and excitation modal frequency tests were conducted on two of the three prototype configurations. The ganged heliostat is designed to operate in a number of different angular orientations for solar tracking, where for this investigation specific azimuth and 0° mirror pitch test scenarios were selected to be representative of an operational system. The same 1/8-inch diameter braided stainless steel wire cabling was used for each respective prototype where linear actuation was carried out on the north end for cable tensioning, and rotational actuation was carried out on both the north and south ends of the suspended structure. During stow, each heliostat system was oriented in a 0° orientation (mirrors in-line or parallel with the cables) and held in place by a weighted dampener located at the center of each system.

Prototype 1

From the start wind induced oscillation has been of particular concern; this is true with any tensile structure. Skysun with assistance from NASA Glenn Research Center and MAGNET determine the natural frequencies of the first small-scale prototype (pre-Sandia Prototype 1). Three tri-axial accelerometers were placed at various locations on the reflective strip. Induced vibration data were collected with the strip operating at its high and low extremes of tension. The results were

favorable for wind survivability. This was repeated on the Prototype 1 system at Sandia. The results are documented in a separate report by Moya et. al and summarized below.

The first ganged heliostat prototype (Prototype 1) was oriented at 0° (face up), 45° and 90° azimuth orientations for the modal tests. The design, as illustrated in Figure 13, features a number of mirrors (representing heliostats) that were allowed to slide on two guide wires 1/8-inch thick which can be tensioned and rotated to align with a given receiver target. This prototype consisted of 22 individual mirror facets, each at 30.48 x 30.48 cm square (1 x 1 feet square), fixed to two approximate 1.5 ft. sections of PVC pipe. Two guide wires were strung through these individual pipe sections to allow for manipulation of the facets by controlling the tension and rotation of the wires at either of the two support structures. The support structures, which consisted of a wood blocks and Unistrut-assembled frame, were each weighed down with concrete blocks and sandbags, which each weighed over 315 kg (700 pounds) in total exceeding the tension in the guide cables. Two rotational actuators, as shown in Figure 13, on either end of the ganged heliostat span controlled rotation arms of the cables, while two separate linear actuators controlled the cable tensions. However, there was no measurement instrument available during the test to measure the tension in the wires, and thus the low and high-tension configuration mentioned are qualitative and kept constant by arbitrary marks on the linear actuator. There were various modal vibrational tests conducted to determine resonant frequencies and the first few dominant mode shapes. A computational model was developed to validate the experimental natural frequency observations, as well as to qualitatively evaluate resonant mode shapes. The ganged heliostat does not have a traditional free-free nor a fixed-base boundary condition as the installed prototype was not a final design, thus the boundary condition was considered to be “pseudo-fixed.”



Figure 13. NSTTF ganged heliostat Prototype I installed at Sandia. Twenty-two mirrors, representing heliostats, are supported on two 1/8-inch guide wires.

Again, the supports on either end were weighed down which allowed for a relatively accurate assumption that the ground is fixed. While this assumption is good for test purposes, it is noted that it can be very difficult to obtain a true infinite stiffness “fixed” boundary condition as any structure or base will have some small compliance. Fixed-base modal testing was accomplished through specialized sub-structuring routines using an in-house Matlab algorithm, however this was not performed on the ganged heliostat prototype.

The experimental test setup for acquiring the first fundamental modes of the structure included a total of 20 PCB 356A33 100mV/g accelerometers glued to strategic mirror facets and on the wood support structures on either end as shown in Figure 14a. The accelerometers were glued to the mirror facets with super glue while using an intermediary layer of Kapton tape for protection of the mirror surface. Excitation for the stand-alone modal tests were performed using an instrumented modal hammer with a nominal sensitivity of 100 mV/lbf (Figure 14b). Initially,

challenges were found with the hammer having trouble exciting lower frequency modes of interest, where consequently a square section of foam was taped to the hammer head. This modal technique helps provide lower frequency energy needed to excite the modes of interest.

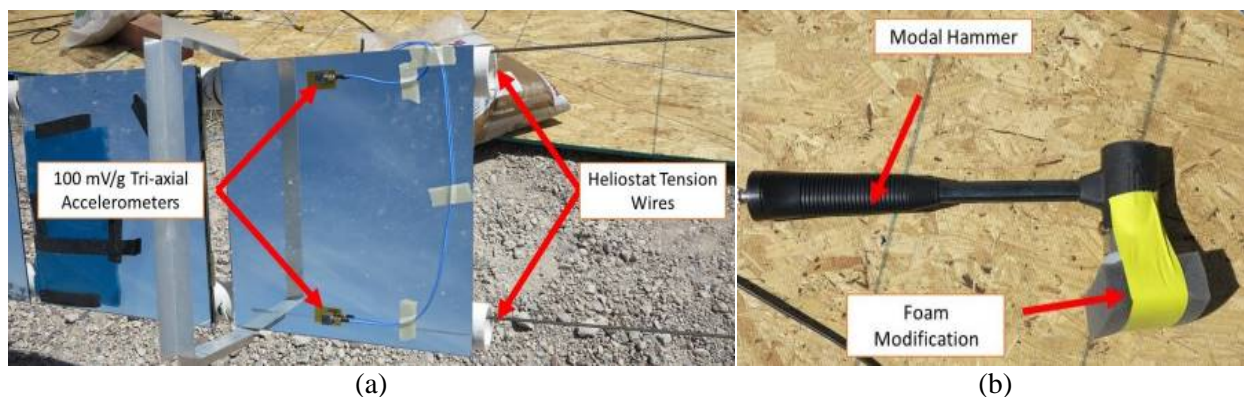


Figure 14. Experimental a. facet accelerometers and b. modal hammer with foam modification.

Prototype 2

After the vibration and modal analysis were performed, Skysun replaced the mirrors with mirrors that have independent pitch angle adjustments. The number of mirrors mounted were reduced to 13. The second ganged heliostat prototype (Prototype 2) included the same linear and rotational motor controls as well as the 1/8-inch braided steel wire cabling. However, the 13 mirrors within the prototype (Figure 15) consisted of smaller 15.24 cm x 30.48 cm (6 in. x 12 in) facets, where again the PVC pipe ends were held adjacent to each other by gravity. Further inspection of these joints displayed chaffing and added dampening during modal vibrational testing which provided inconsistent results, Figure 16, where the team decided to develop a more structurally conservative third prototype.



Figure 15. Experimental ganged heliostat Prototype 2, containing 13 rotatable facets.



Figure 16. Prototype 2 ganged heliostat system under a 45° orientation demonstrating notable chaffing between adjacent facets at point of contact between upper PVC pipes pictured.

Prototype 3

The third prototype was a modification of Prototype 2 to provide more discrete mirror facets that could be approximated as point load sources, which could be validated by the mechanical models developed in this investigation. This prototype was developed to be a scaled representation of a 10 MW ganged heliostat system, capable of facilitating up to 13, 64 m² individual heliostats. For the third prototype, Figure 17, the 13 mirrors were erected with a cable horizontal span of 9.1 m. In this configuration the smaller mirrors could all be adjusted in south-facing pitch for more intricate optimization. The individual facets also had PVC arms that were reduced to 4 in. lengths, which were clamped to the cables using ferrying washers and cable clamps.



Figure 17. Prototype 3 with 13, 4 kg (9 lbs) facets, with a 9.1 m span and a 20:1 span to sag ratio, as well as with four respective clamps per facet.

OFFICIAL USE ONLY

To facilitate modal excitation for this prototype configuration, a low-cost approach was devised where an operator manually moved the structure in an approximately consistent rhythmic fashion as shown in Figure 18 in slow and fast: 1) side to side (horizontal), 2) up and down (vertical) and 3) torsional motions. The tests were each conducted for approximately 60 seconds where the 1/8-inch cable was allowed to come to a steady mode shape. The two ends of the ganged heliostat were adequately weigh down with sandbags and concrete to ensure stiffness at the ends while the lowest point of the cable remained at least 12.7 cm (5 inch) from the ground during each respective test.

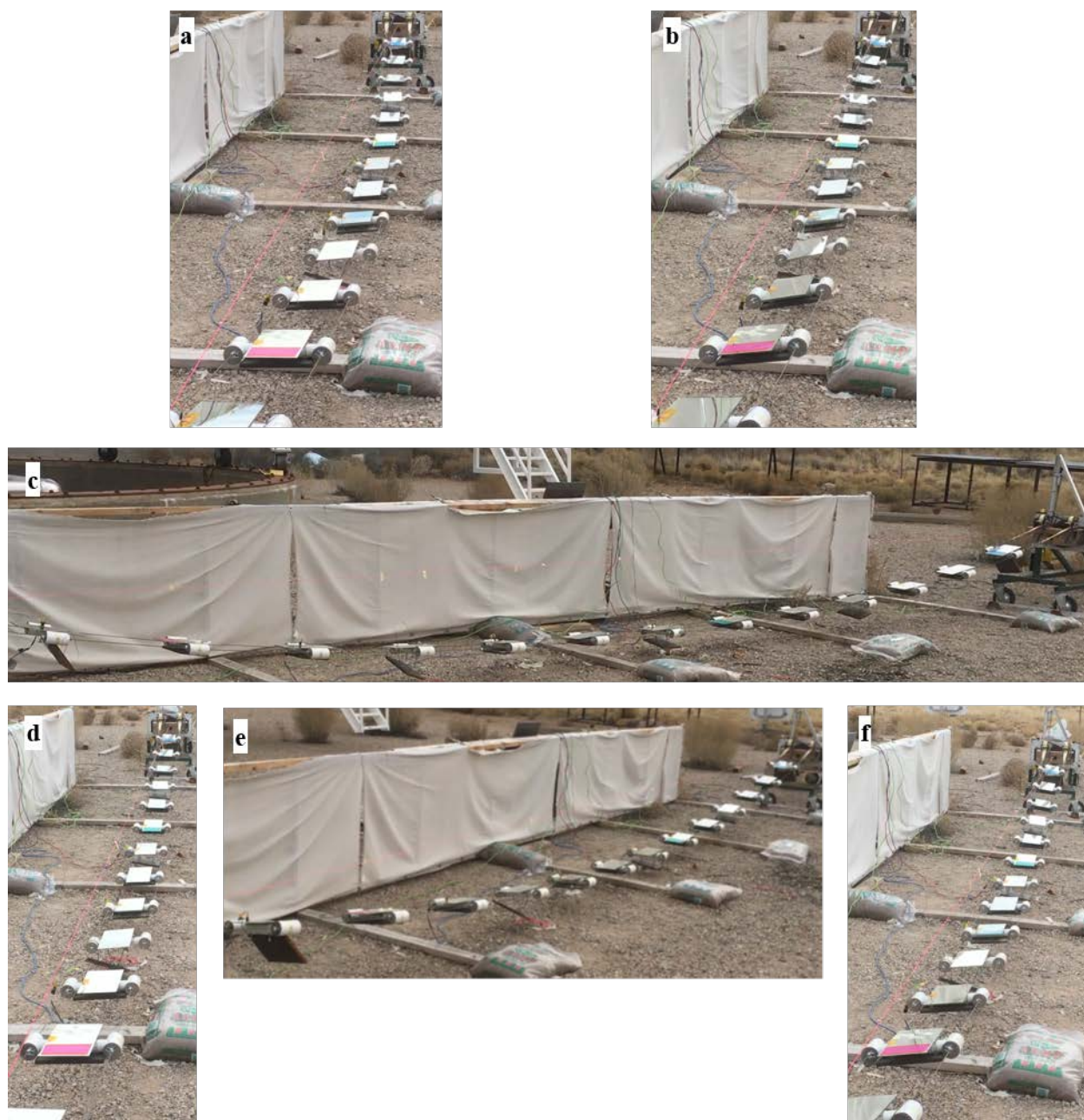


Figure 18. Prototype three excited modes from north-end cables in a. slow - side to side (horizontal), b. fast – side to side (horizontal) c. slow - up and down (vertical), d. fast – up and down (vertical), e. slow – torsional and f. fast torsional motions.

This design was facilitated to provide a scaled prototype of a 10 MW system, where in that system the cables will span 175 m with up to 13, 64 m² heliostats each weighing approximately 1500 kg (3,300 lbs.). To provide proper scaling, weights up to 4 kg (9 lbs.) (based on calculated span-to-sag and facet size scaling factors) were added to each mirror facet with a small footprint to model the facets as point-load sources.

Coordinate System and Measurement Locations

Prototype 1 heliostat was instrumented with 20 total tri-axial accelerometers. Of these 18 accelerometers were glued to the center top and bottom portion of the mirrors and labeled as nodes 101-109 and 201-209 as seen in Figure 19a. In addition to these mirror locations, a single tri-axial accelerometer was glued to the wood supports (rotation arms) on either end of the cable end supports: nodes 301 and 302. It was found that force inputs on either side of the wood support provided good controllable excitation of the low frequency modes of interest and thus node 302 location was used for a drive-point.

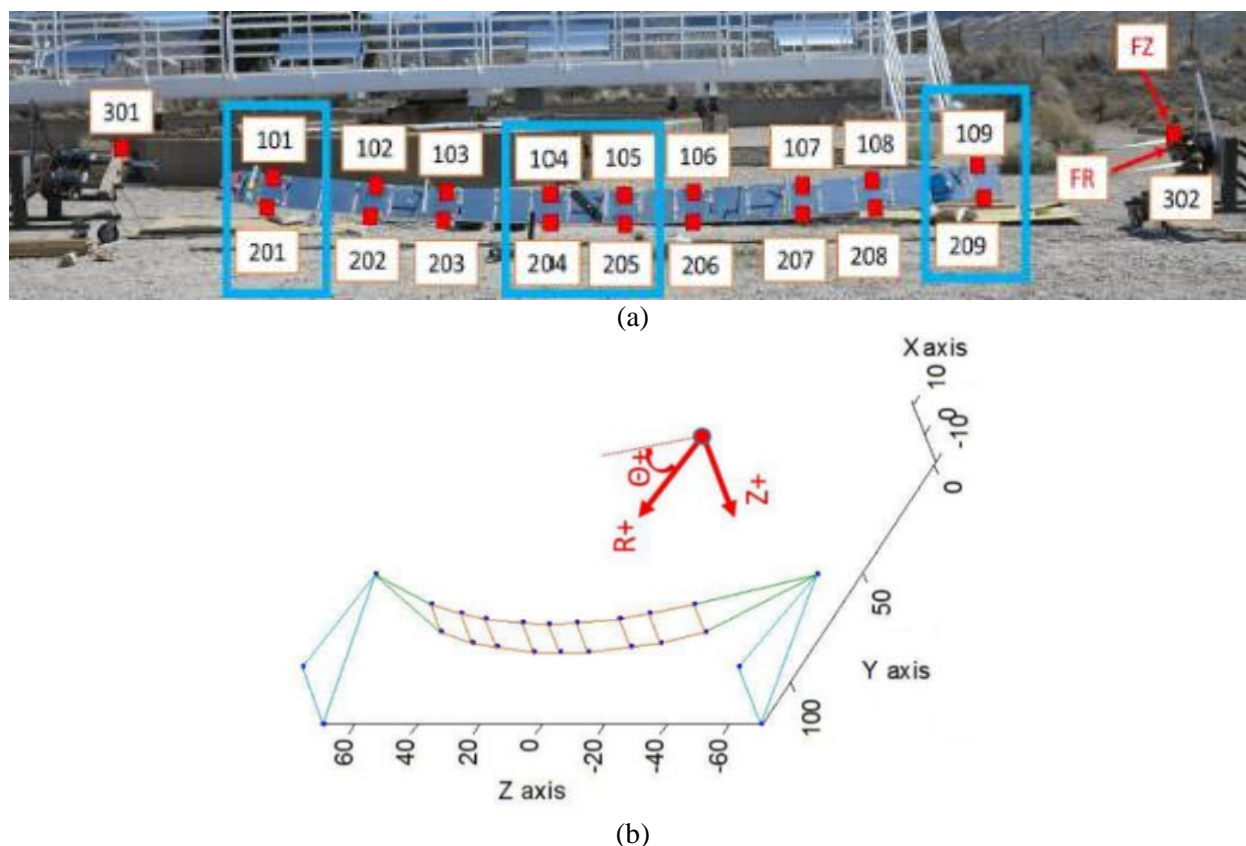


Figure 19. a) Accelerometer and force input locations on Prototype 1, and b) illustration of an example 0° ganged heliostat orientation modal geometry in Matlab.

Prototypes 1 and 3 DAQ Setup and Uncertainties Descriptions

The experimental geometry was first recreated in Matlab for Prototype 1 mode shape animation purposes. Figure 19b illustrates the relative coordinate system used within the 45° orientation framework, where the modal geometry is rotated using a simple transformation matrix. A Brüel

& Kjær data acquisition (DAQ) system was used for the tests and set up to measure data between zero and 50 Hz, with a frequency resolution of 0.0625 Hz and a frame length of 16 seconds. No windows were applied to either the data from the reference excitation or the accelerometers as the response of the unit completely decayed within the time frame. Data was averaged over five different impacts at each node location. End-to-end system uncertainty was estimated by recording the DAQs response to a 1 V sine source signal on all channels used in a test described by Hensley [25]. All channels were within a standard deviation of 1.9%, which was well below the 5% standard reported for accelerometer calibrations.

For Prototype 3, low-cost tri-axis accelerometers (ADXL 335) were mounted to the center lines of seven mirror facets (one accelerometer per facet), equally spaced along the ganged heliostat as shown in Figure 20. For these tests, an Arduino MEGA 2560 MOTE device with SparkFun® tri-axis accelerometers were employed along the centerline of each respective facet during operation. The acceleration data collected was then processed in Matlab where a Fast Fourier Transform (FFT) was taken for the respective directional acceleration data over a 60 second period. The results were then compiled to determine the most dominant modal frequencies observed for vertical, horizontal and torsional motions. The accelerometers were not calibrated for response and accuracy. However, static testing showed the accelerometers measured the gravity axis well in all three axes, which was deemed sufficient. In the future, calibrated accelerometers will be used.



Figure 20. Prototype 3 accelerometer sensor positions.

4.2.2. Computational Model

To validate the experimental results, a 3D solid model was developed to simulate respective natural frequencies and mode shapes. Expanding on modeling efforts [26] a model for the experimental prototype was developed using SolidWorks for analysis within the finite element analysis (FEA) framework using SolidWorks Simulation. For this analysis, facet position coordinates were collected from the prototype and used to model the prototype as illustrated in Figure 21, with a

gravitational load applied and where the ends were fixed and rotated according to the respective validation boundary conditions. To ensure computational accuracy, a mesh refinement optimization analysis was first performed until consistent results were achieved between each successive mesh discretization. For the two orientations (i.e., 0° and 45° orientations), ten and nine respective frequencies were calculated, where respective mode shapes were also determined and compared.

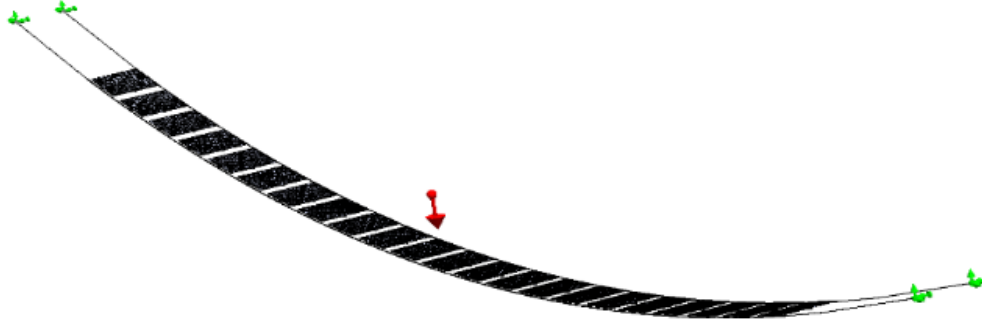


Figure 21. 3D simulation model and constraints for the prototype ganged heliostat system.

The model developed here is based on simple a finite element system where a system that obeys Newton's law of motion leads to the differential equation of motion in terms of displacement as a function of time, $X(t)$. This equation can be specified by specified degrees of freedom (DOF), which generalizes to a displacement vector interacting with a square mass matrix M , stiffness matrix K , damping matrix C , with the form prescribed by Equation 6 [27].

$$M d^2X/dt^2 + C dX/dt + Kx(t) = F(t), \quad (6)$$

where $F(t)$ is the externally applied force vector. For a simple harmonic motion, or free vibration mode ($C=0$, $F=0$) a generalization can be made that $X(t) = A \sin(\omega t)$ where amplitude A , is the mode shape vector at a specific frequency, ω . For this analysis the investigators will be calculating respective frequencies, ω_k and mode shape vectors, A_k for each degree for freedom k , and determining their correspondence to experimentally determined results under zero-velocity wind conditions. For Prototype 3, the experimental geometry was recreated within SolidWorks based on the measured 3D coordinates of the mirror facets using a theodolite. Figure 22 shows this model where the PVC pipes were approximated to be concentric with the cable as well as the facets oriented horizontally.

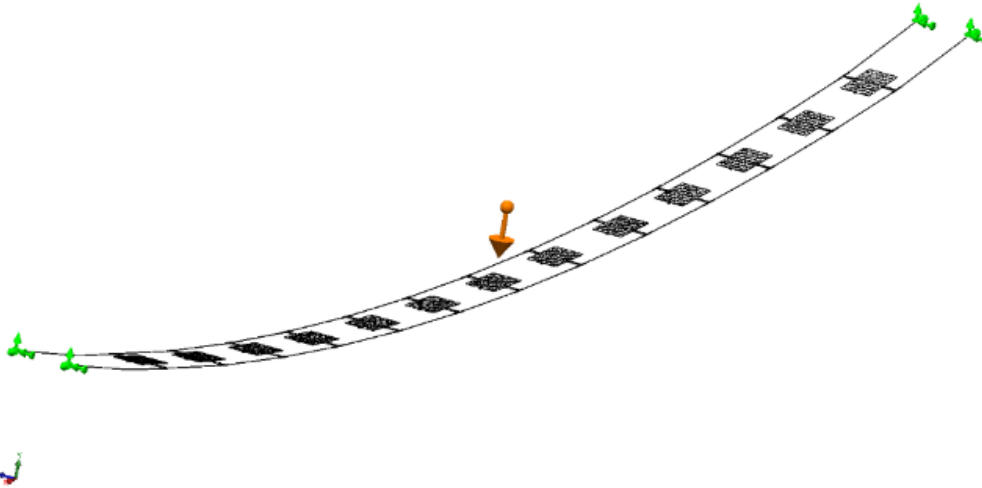


Figure 22. Computational model of Prototype 3 experimental geometry.

4.2.3. Experimental Results

Prototype 1

Vibration and modal analysis on the Prototype 1 configuration was performed by Moya et al [28]. There were 22 mirrors mounted when the analysis was performed. The analysis showed the dominate low-frequency vibration modes. During the Prototype 1 experimental measurements, hammer excitation was provided in both radial and Z+ axis directions at node 302 (Figure 19a). The force input was repeated five times in each orientation and averaged for the results presented. The force auto spectra shown in Figures 23a through 23c for 0°, 45° and 90° orientations respectively, shows the hammer input properly excites the structure beyond the recorded bandwidth or 50 Hz, however all modes were determined to be below 6 Hz.

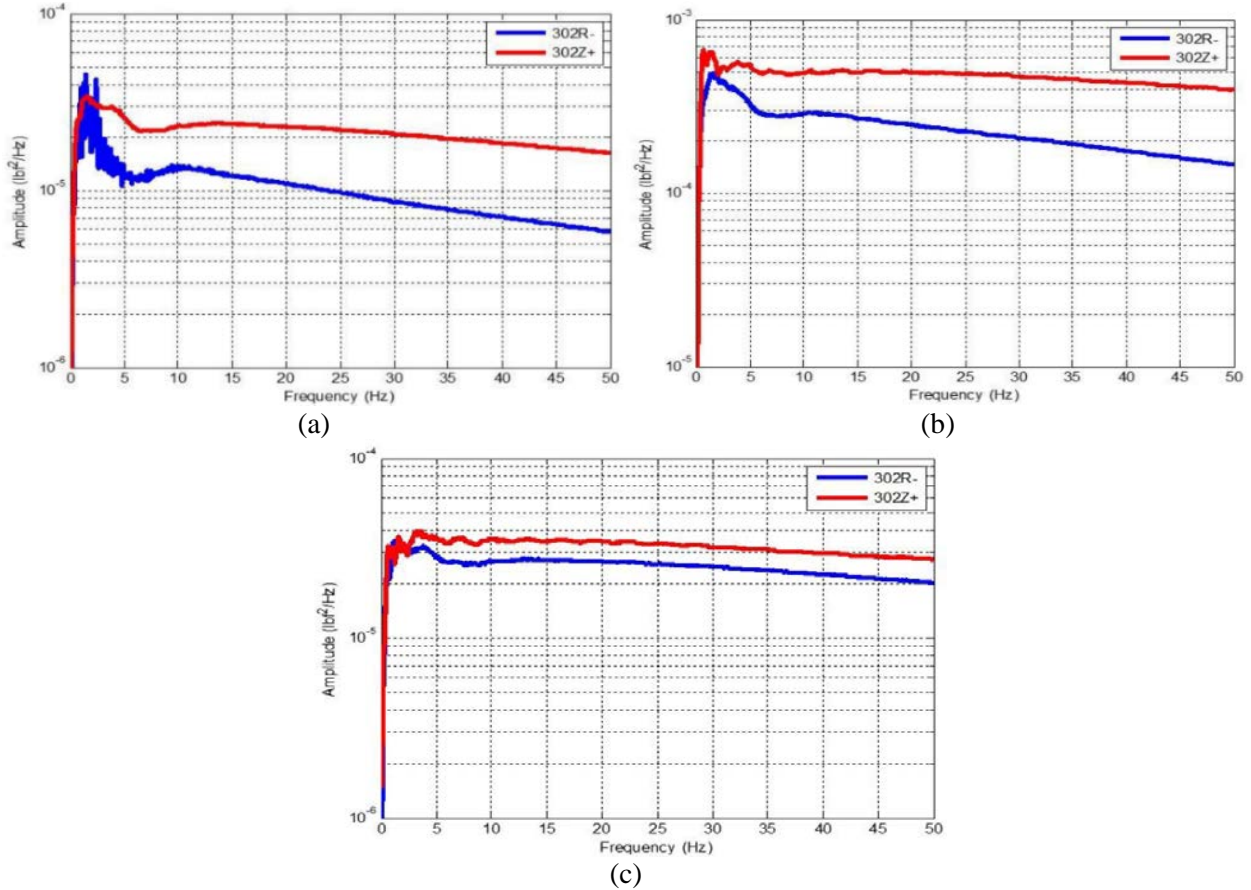


Figure 23. Auto spectrum hammer excitation for a) 0° orientation, b) 45° orientation and c) 90° orientation of the cable rotation arms.

Since some mode shapes have a higher propensity for destruction than others, an analysis was performed to determine the position similarity from one test to the next, with respect to the most destructive mode shapes. Here, a self-MAC (modal assurance criterion) analysis was performed to illustrate the similarity between all mode shapes for each test configuration based on non-dimensional values between 0 and 1 (0 representing completely unique modes and 1 signifying identical shapes). For a complete set of unique modes, the MACs should be close to the identity matrix. Figure 24 provides MAC analysis plots for 0°, 45° and 90° orientations. Also plotted is the complex mode indicator function (CMIF) [25] calculated from measured data and their corresponding curve fits synthesized from extracted modal parameters. These plots provide a measure of how well the extracted data represents the actual data. Note that the modal extraction for this structure was difficult due to data acquisition limitations restricting the frequency resolution.

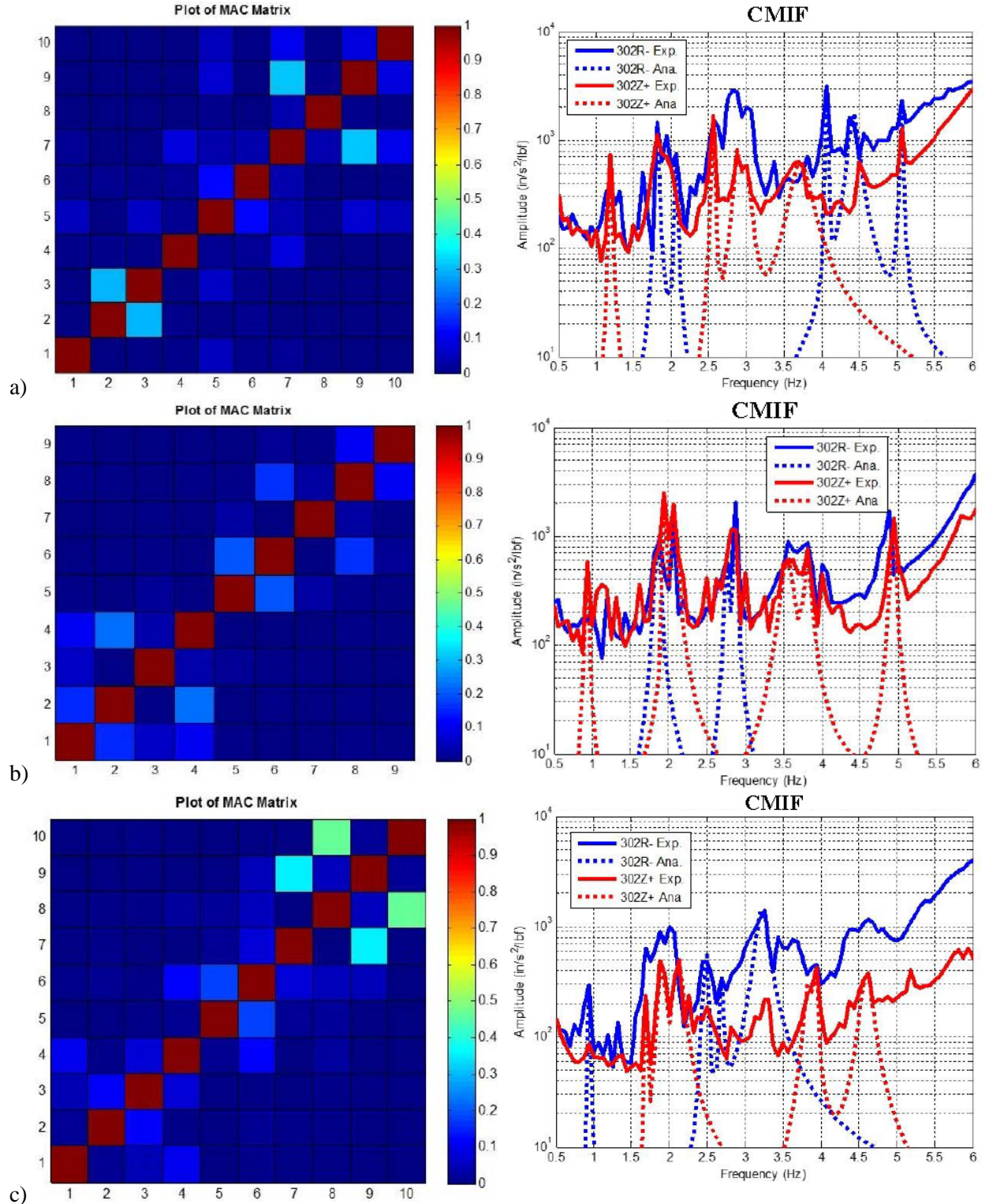


Figure 24. Self-MAC configuration analysis and experimental and analytical CMIF comparisons for a) 0°, b) 45° and c) 90° orientations, where 302R, and 302Z locations correspond to heliostat end locations.

A comprehensive list of resultant mode shapes for Prototype 1 can be found in Appendix 1. The modes were found to be repeatable in the different orientations giving confidence with the modal fits, which provided similar frequencies to what was seen in the wind excited data [23]. The experimental results from the 0° orientation can be seen in Table 3 where ten modes were calculated with respective mode shapes and natural frequencies ranging between 1.19 and 5.06 Hz. Also, included in Table 3 are natural frequencies determined from the computation model where relatively good agreement was found between the two data sets within 10% error. This was found to be especially true for mode 7 where approximately identical frequencies of 3.71 Hz were found for this mode pertaining to a torsional twist mode shape which has been previously found to facilitate damage to suspended structures [22]. Both experimental and model mode shapes for this mode frequency are presented in Figure 25. From the resulting mode shapes analysis, identification of the highest amplitude locations that could result in structural failure were determined. On average the largest amplitude (for both 0° and 45° orientations) was found to be located at the center of the heliostat strip. This can be significant as mechanical perturbations can impact the optical performance and CSP system performance.

Table 3. Experimental and computational modal results comparison for 0° orientation ganged heliostat Prototype 1.

Mode Number	Mode Description	Modal Test Frequency (Hz)	Computational Model Frequency (Hz)
1	In-plane sway rigid body	1.19	1.29
2	1 st pinned bending	1.82	1.87
3	1 st free bending	2.06	2.13
4	1 st in-plane torsion/bending	2.55	2.57
5	Rigid body rotation	2.89	2.91
6	2 nd free bending	3.0	3.17
7	2 nd in-plane torsion twist	3.71	3.71
8	3 rd free bending	4.07	4.21
9	1 st torsion	4.43	4.49
10	4 th free bending	5.06	5.15

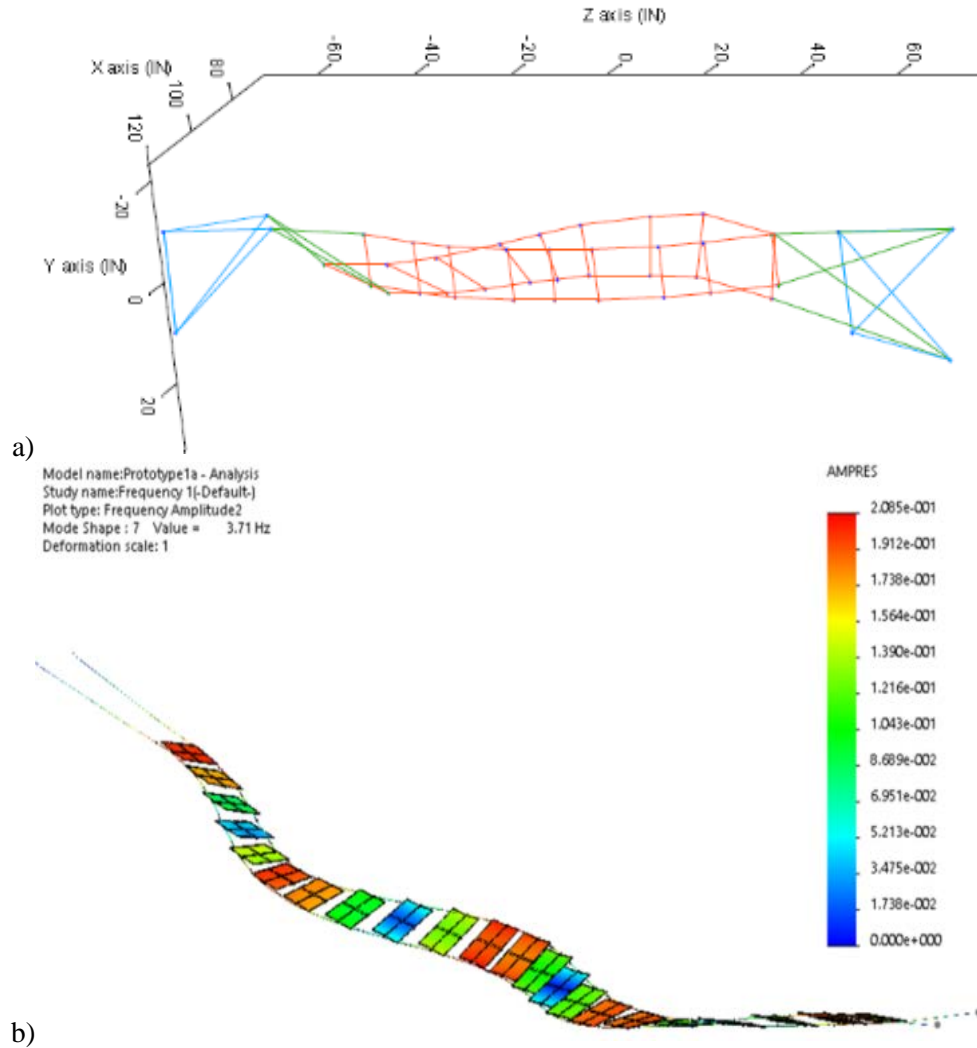


Figure 25. Natural frequency mode shape determined from a) experimental measurements and b) computational model for torsional twist.

Similarly, experimental results from the ganged heliostat prototype in a 45° orientation can be seen in Table 4 against computationally determined frequencies. Here, nine modes were measured and calculated with respect to mode shapes and frequencies ranging between 0.93 and 4.92 Hz. For the 90° orientation (Table 5), 10 modes were measured and can calculated within the range of 0.94 to 4.60 Hz, where the average percent difference between the computational model and the experimental results was 3.2%, where uncertainties could be explained based on measurement error with the attached accelerometers and DAQ system, as well as computational approximations with respect to the mesh and facet geometries.

For the 45° orientation results, mode 3 was not attained possibly due to proper excitation or facet weight, which could contribute to dampening for facilitating a well-excited state. Additionally, mode 3 may not have been identified by the system computational algorithm as it is a closely spaced mode.

Table 4. Experimental and computational modal results comparison for 45° orientation ganged heliostat.

Mode Number	Mode Description	Modal Test Frequency (Hz)	Computational Model Frequency (Hz)
1	Rigid body sway / 1 st bending	0.93	1.09
2	2 nd free bending	1.85	1.82
3	1 st torsion / twist	1.94	---
4	Rigid body sway / twist	2.07	2.25
5	2 nd torsion / twist	2.75	2.73
6	2 nd free bending	2.86	2.99
7	3 rd free bending / twist	3.55	3.72
8	3 rd torsion twist	3.81	3.85
9	4 th free bending	4.92	4.90

Table 5. Experimental and computational modal results comparison for 90° orientation ganged heliostat.

Mode Number	Mode Description	Modal Test Frequency (Hz)	Computational Model Frequency (Hz)
1	Rigid body sway	0.94	0.90
2	2 nd free bending	1.68	1.77
3	Rigid body in-plane sway / bending	1.90	---
4	Rigid body twist	2.10	2.02
5	3 rd free bending	2.48	2.48
6	2 nd in-plane bending	2.68	2.79
7	1 st torsion	3.22	3.17
8	4 th free bending	3.84	3.69
9	2 nd torsion	3.93	4.10
10	Bending / torsion	4.60	4.55

However, this mode, whose behavior is weakly dependent on orientation, was identified to be very similar to mode 2 in the 0° orientation results. For this orientation, the 2nd through 4th torsion twist and free bending mode predictions were in reasonably good agreement with each other, to within 12%. Of these frequencies for this orientation, mode 5 was found to have the closest agreement where respective experimental and computed mode shapes are shown in Figure 26. Based on analysis of multiple data sets, for both 0° and 45° orientations, and viewing of experimental mode shapes, it was believed that the cause of the discrepancies between the experimental and computational results may be due to rigid body modes associated with the linear system drive, which was not modeled for analysis in SolidWorks. Here, computational approximations were made for the geometry of the facet to ensure that the ends were concentric about the two cables to improve the quality and simplicity of the mesh. Additionally, the facets themselves extended to

the cable concentric contact geometries to also aid in mesh quality, where the density of the entire facet was adjusted to get to the total facet measured weight of 9 lbs. Additionally, other sources of discrepancy could be that these final modes depend strongly on the stiffness of the rotational motor, which again were not modeled.

It is important to note this low frequency error of the data is to be used for FEM model correlation as some of the modes may not exist and be an artifact of the noisy hammer input at low frequencies. For this prototype demonstration the experiments performed by the group provided natural frequencies that could be used a scaled-up 10 MW system. The results suggested that the mode shapes with the largest displacements were isolated and shown to be excited in a very windy environment which produced low natural frequencies.

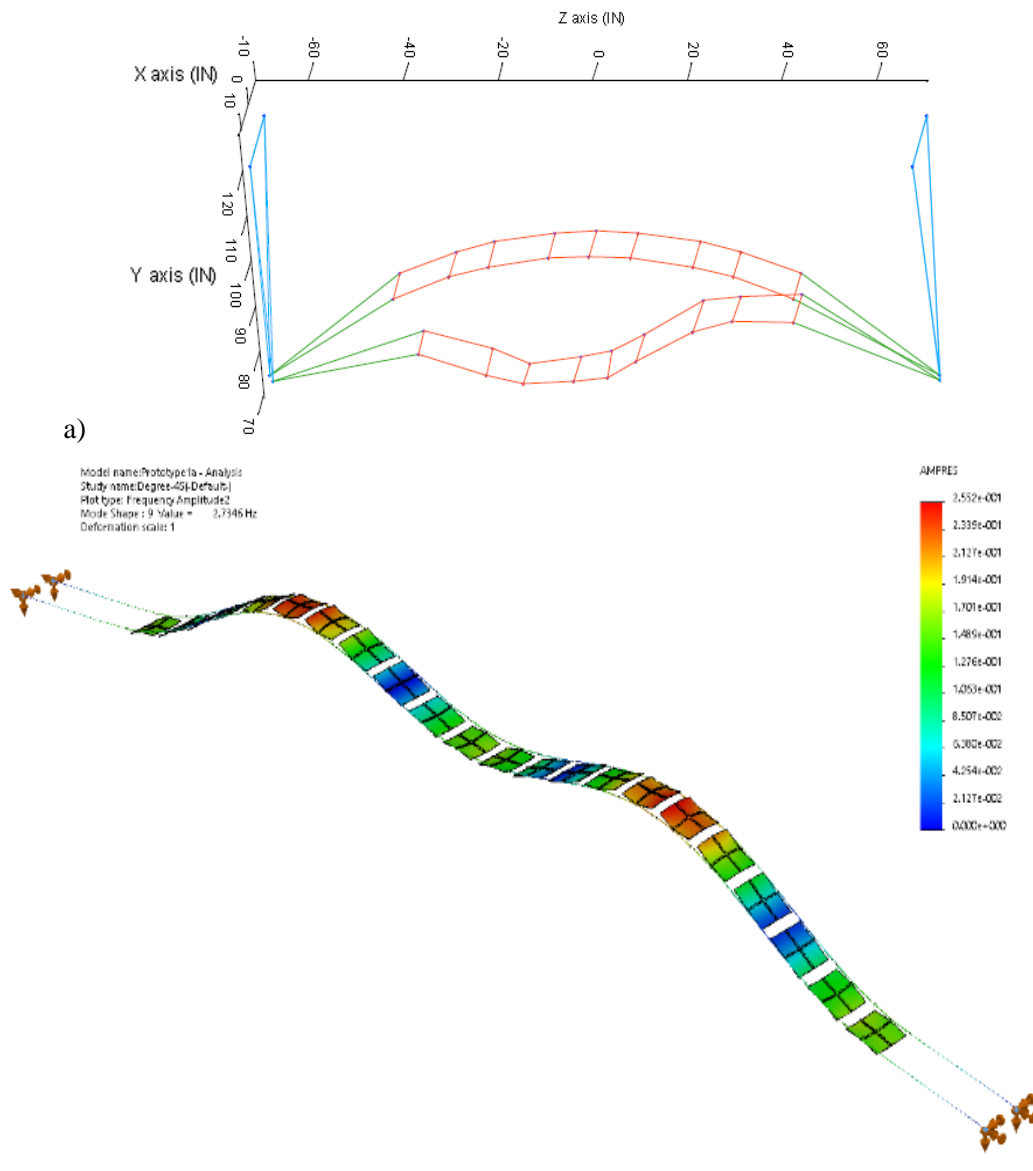


Figure 26. 45° orientation Mode 5 shapes determined from a) experimental measurements and b) computational model.

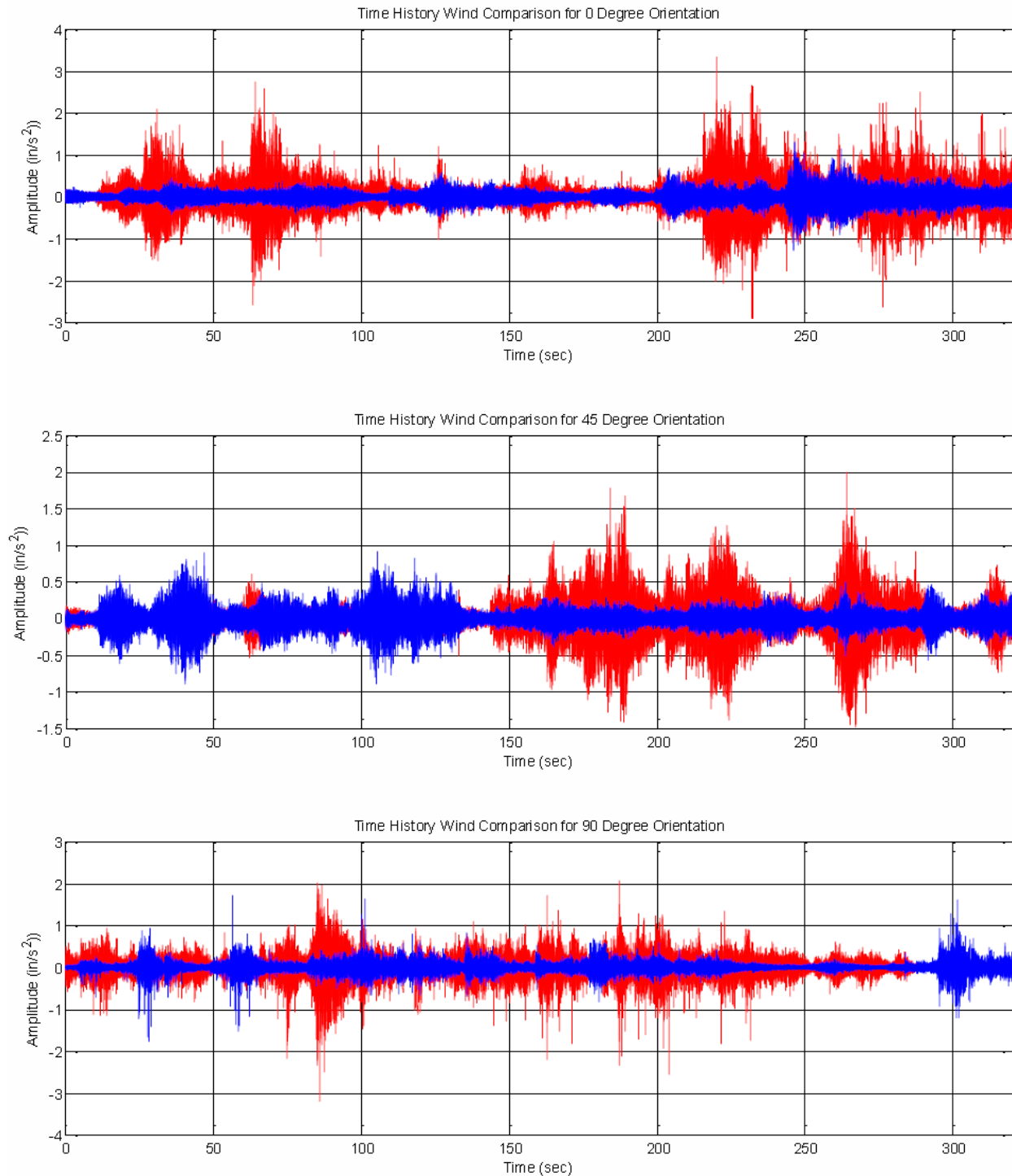


Figure 27. Prototype 1 time histories for low vs. high wind excitation during testing.

An effort was made to capture wind excitation in the three orientations, however the timing proved somewhat difficult. There was no available method of recording wind speed and direction along with the data, and thus a hand held anemometer was used to approximate wind speed for each data set. Data was recorded during a low wind speed and a higher wind speed to examine the amplification of the low frequency modes presented in the above section. The low wind speed data was taken during 3-6 mph gusts while the higher wind speed contained 10-18 mph gusts. Figure 27 above displays the time histories for the maximum responses in the three orientations for the low wind speed (blue), and the high wind speed (red), where accelerometer amplitude data is provided in units of in/s^2 . The spikes in each acceleration time history represents the individual wind gusts. Note that the low wind speed data in the 45° orientation is initially higher than the higher wind speed. This was found to average out during the frequency analysis and thus the red dataset was labeled as the high wind speed.

Figure 28 displays the averaged autospectra frequency data, obtained from the accelerometers, for the low vs. high wind speed data presented in Figure 27. This analysis was performed to compare facet amplitude movement between low and high wind speed. These plots show that the higher wind speed correlates to a higher amplitude in low and high frequency responses as well as a shift in the lower modes to a higher frequency. This is intuitively true as the static load of the wind on the mirror facets would increase the tension in the wires which leads to a higher natural frequency. For this case, the modes of interest are below 5 Hz and show a significant response to the wind. The higher frequency data is also excited, but these modes have smaller displacements and do not impact the heliostats performance as much.

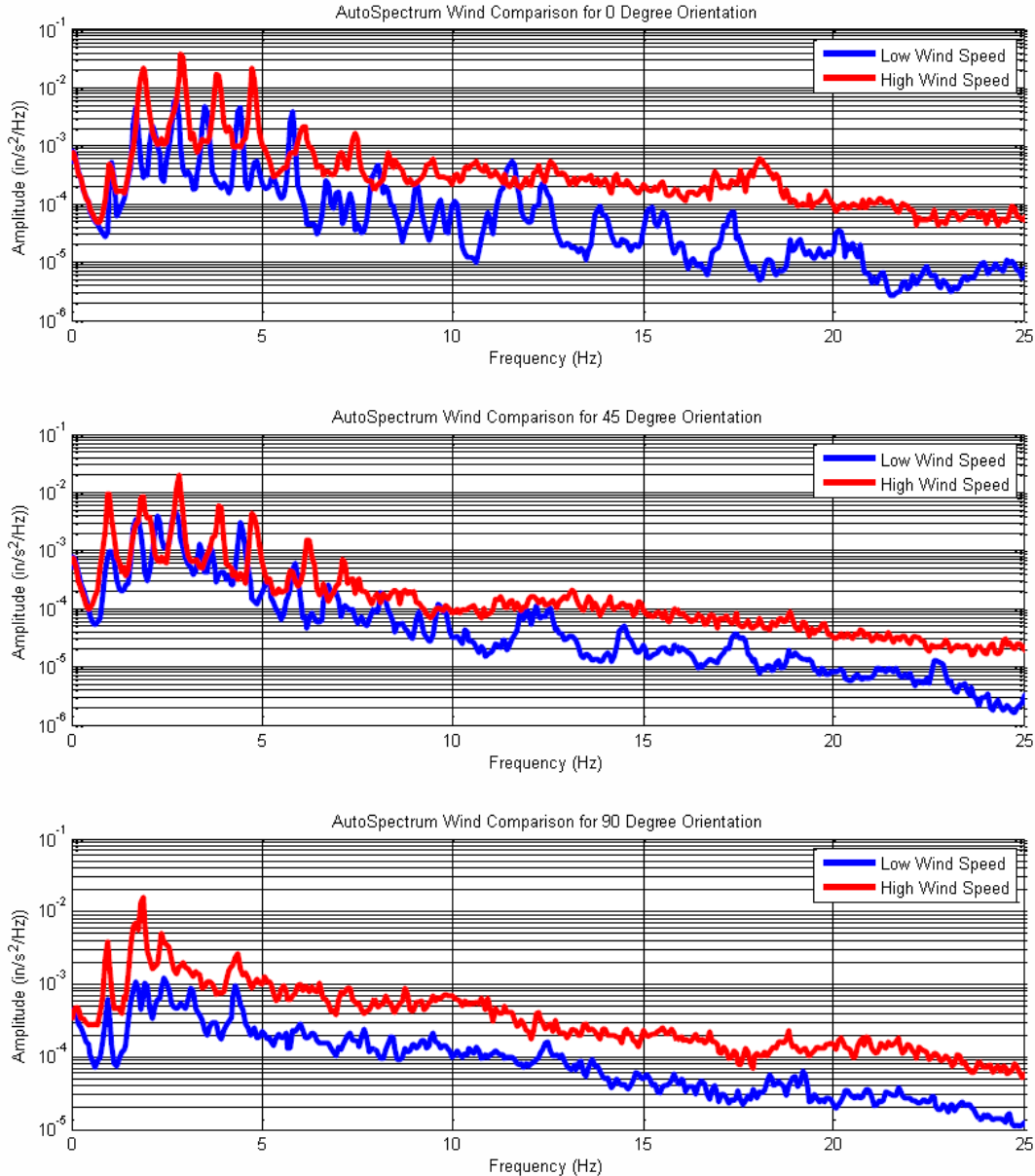


Figure 28. Prototype 1 experimental autospectra for low vs. high wind excitation.

To mitigate the excitation due to wind, a makeshift wind fence was constructed out of wood and canvas, and positioned west of the ganged heliostat system, as shown in Figure 29. The wind fence was placed approximately three feet west of the heliostat prototype. Data was acquired in the same 0° , 45° , and 90° orientations presented in previous sections. It was immediately noticeable that the wind changes directions enough to hit either side of the wind fence making direct correlation of wind blockage to decreased dynamic excitation difficult. The results obtained in this leads one to believe the single wind fence makes no difference in wind excitation, however the application of a second on the east side of the heliostat could potentially facilitate improvements. Though due to time-constraints this was not performed in this investigation.



Figure 29. West-facing wind fence adjacent to heliostat.

Figure 30 provides the averaged accelerometer frequency autospectra response across the heliostat for a fence versus no fence comparison to assess facet amplitude movement. These results seem to show the frequency response shifted slightly to the left when the wind fence was installed, and the amplitudes have increased slightly. For one mode for the 90 case around 3 Hz, the amplitude increased with the wind fence. The increase in amplitudes could be due to a possible facilitation of vortices by the fence. However, the fence seems to have shifted the modes to lower frequency. This could be an anomaly. Additional instrumentation and testing are needed to say with higher certainty the impacts of the wind fence.

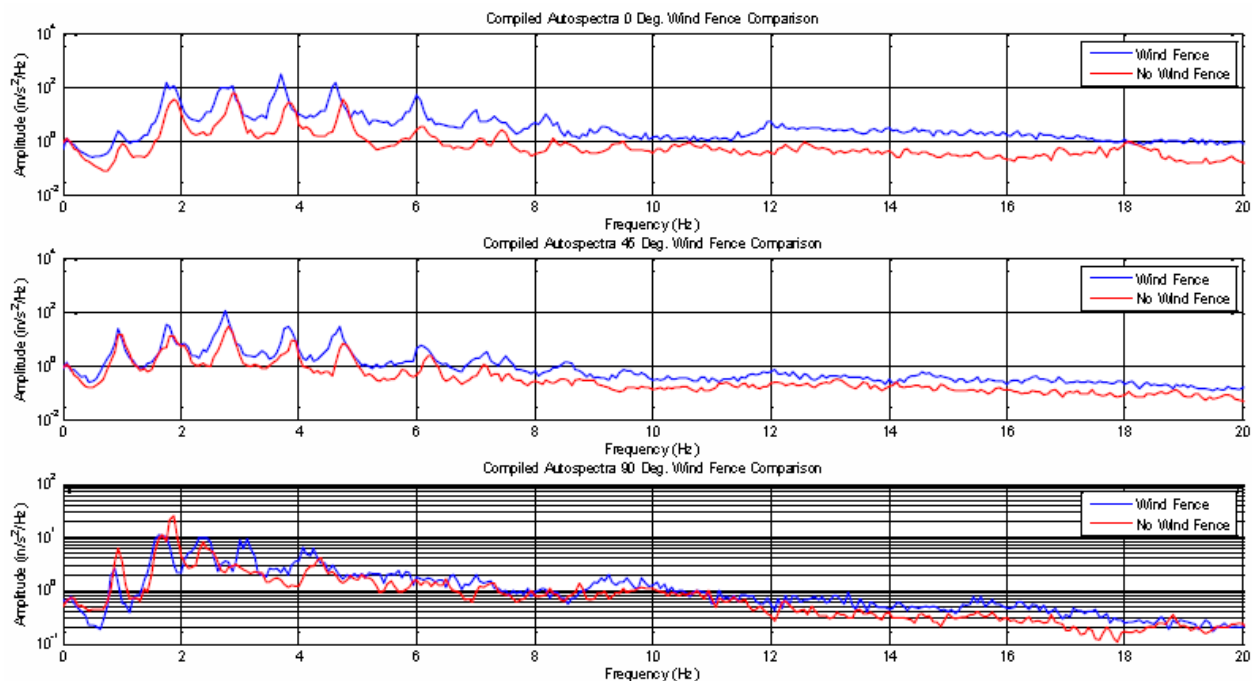


Figure 30. Prototype 1 experiment compiled wind excited autospectra responses for fence versus no fence configurations.

Figure 31 provides the time histories (Blue = Fence, Red = No Fence) and displays a similar trend of increased excitation with the wind fence. Despite these results being indicative of a wind fence

not providing any benefit, further experimentation would be needed to make this conclusive. Future testing would benefit from wind speed and direction measurements, and multiple orientations of the wind fence with respect to the heliostat.

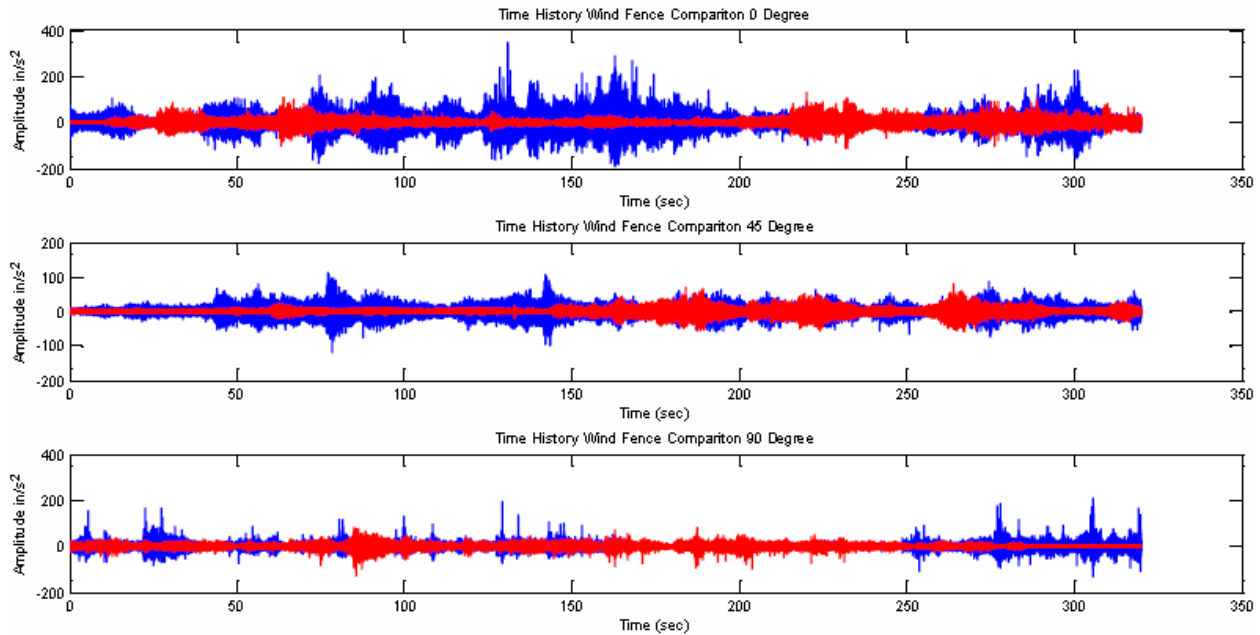


Figure 31. Prototype 1 experiment time histories from wind fence vs. no wind fence comparison.

Prototype 3

The results of the second set of experiments provided modal frequencies based on side-to-side, up and down and rolling motions of the two guide cables. Table 6 shows the modes with the highest amplitudes. In this case, although the frequency responses were measured in all three axes of the accelerometers, only the magnitudes of the modes are reported. That is, the frequency response in the three axes were combined by a root sum square. The mode oscillation directions were not quantified due to limited number of accelerometers used.

Table 6. Resultant aggregate measured modal frequencies.

Mode Number	Modal Test Measured Frequency [Hz]
1	0.74
2	1.16
3	1.43
4	1.47
5	1.48
6	1.92
7	2.33
8	2.34
9	2.39
10	2.87
11	2.93
12	2.97
13	3.72
14	4.31
15	4.71
16	5.76

To obtain these values, two sets of position data were collected for five accelerometers placed in seven equal distance locations along the ganged heliostat, as shown in Figure 32. The respective data sets were converted to acceleration values, which were then used to determine respective natural frequencies. For the two tests in each respective motion, accelerometers were placed in the 1, 4 and 7 locations, which showed good agreement to within 5% difference for all large peaks, where Figure 32 provides an example for accelerometer 1 in the slow, up and down motion. From the results the team concluded that much of the mismatch between tests could have been due to reflected vibrations from the south-end post of the ganged heliostat system, as well as wind impacts and operator error, where increased error was found for increasing frequencies measured.

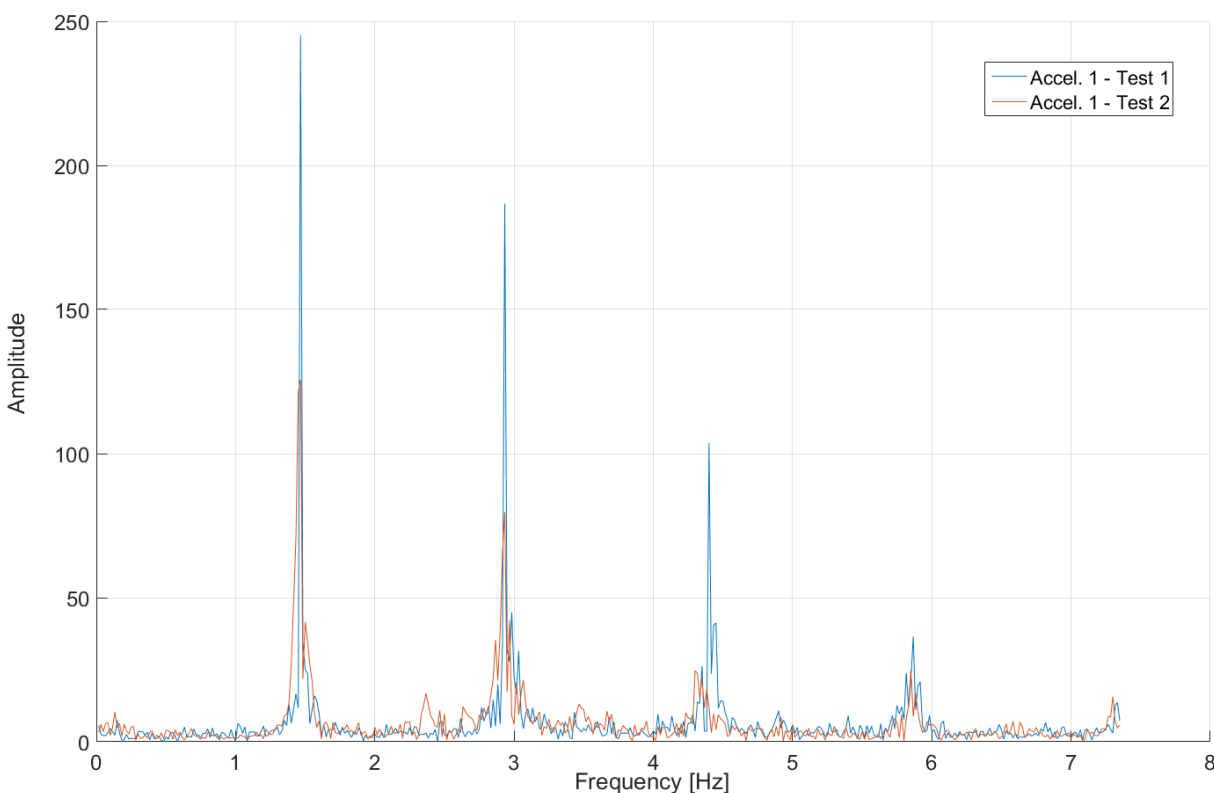


Figure 32. Representative accelerometer comparison between two accelerometer #1 data sets where large frequency peaks showed good agreement.

For each test, data was obtained over a 60 second period where each test had approximately 884 data points collected. Since the saved data were not timestamped, these values were then taken together to obtain the sampling frequency, which was found to be about 14.88 Hz. A Fast Fourier Transform (FFT) function was then employed to process each respective data set to obtain the frequency response, where the respective responses with the largest amplitudes are presented in Table 7. Figure 33 provide the resultant frequencies for the modal motion tests conducted where the largest frequencies respectively are:

Table 7. Largest modal frequencies for each respective motion test.

Modal Motion	Modal Test Measured Frequency (Hz)
Slow – Horizontal	1.48
Fast – Horizontal	1.42
Slow – Vertical	1.47
Fast – Vertical	2.34
Slow – Torsional	2.31
Fast – Torsional	2.36

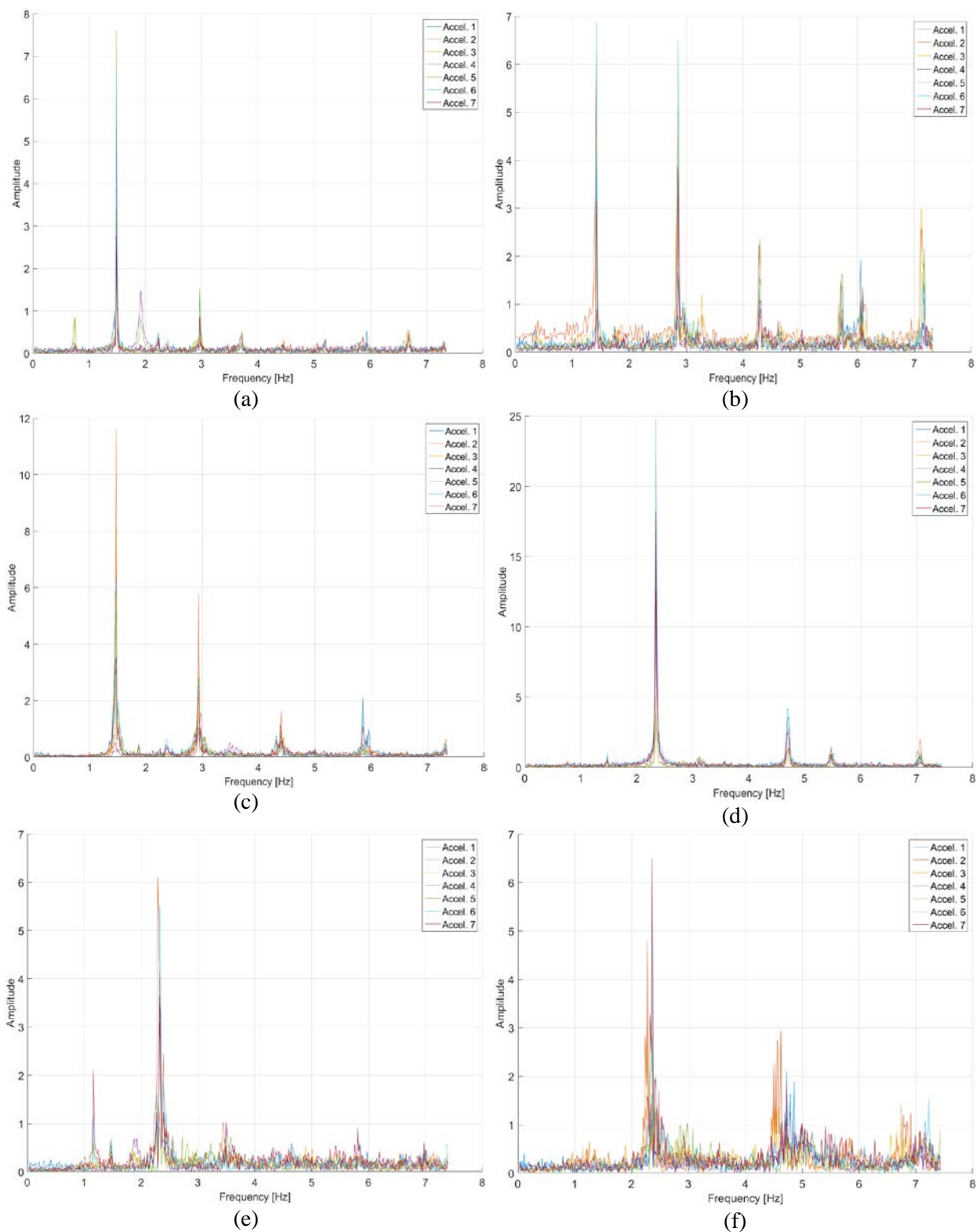


Figure 33. Resultant frequency response measured data for motions: a. slow - horizontal, b. fast – horizontal c. slow - vertical, d. fast – vertical, e. slow – torsional and f. fast torsional.

4.2.4. Modeling and Dampening Analysis Results

Frequency analysis models were developed using SolidWorks Simulation and FlowSimulation to assess mode shapes for both Prototypes 1 and 3. The simulations were developed using the respective geometries of the two prototypes for both cables and facets as shown in Figure 34, where the cable ends were modelled with cable concentric design assumptions (for proper meshing) were made to the PVC pipes.

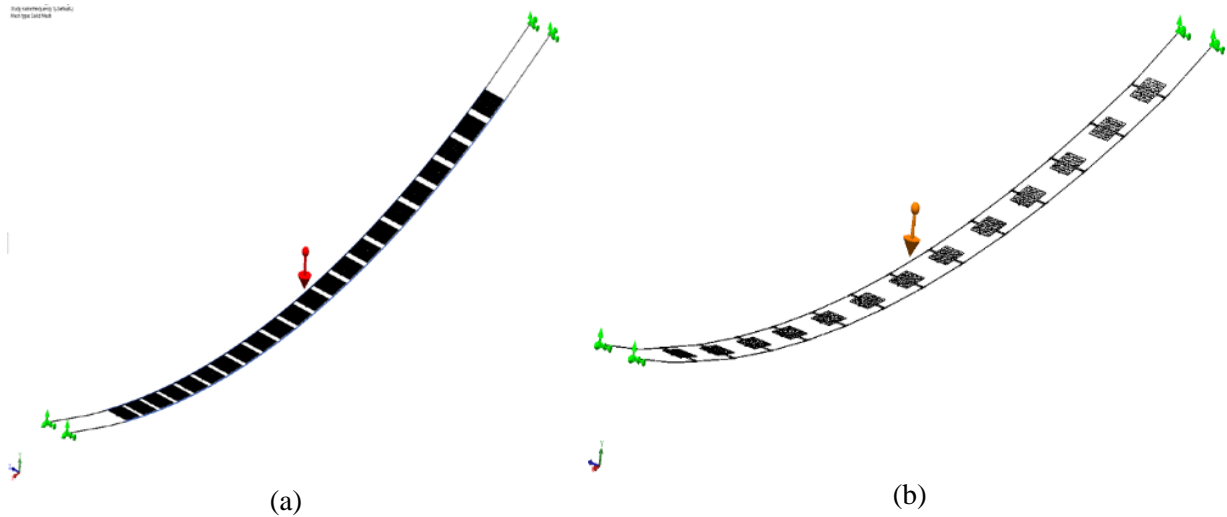


Figure 34. Solid models of a) Prototype 1 with 22 facets, and b) Prototype 3 ganged heliostats, with 13 facets, with applied gravity loads and standard fixed geometries at cable ends.

Modal analysis was conducted parametrically for three different ganged system rotation angles of 0° , 45° and 90° , as well as for wind speeds of 0 mph, 30 mph, 35 mph, 50 mph and 90 mph. The lower wind speeds of 30 and 35 mph were chosen as they are typical stow values for heliostats, where 50 mph and 90 mph represent higher typical operational and destructive limits respectively. Although the results found little variation for each respective orientation with respect to wind speed, the resulting modal frequencies were found to decrease overall from the 0° orientation. These results indicate that easier attainable excitations at lower frequencies are more easily achieved as the ganged heliostat rotates, however increasing steady wind speeds facilitates the same modal responses. Table FF provides the calculated modal frequencies for this study up to 5 Hz excitation, where larger values contain error due to reflected waves and wind harmonic impacts.

OFFICIAL USE ONLY

Table 8. Prototype 3 computed modal frequencies for varying ganged heliostat orientation angle.

Mode Number	0 Orientation (Hz)	45 Orientation (Hz)	90 Orientation (Hz)	Measured (Hz)
1	0.83	0.69	0.71	0.74
2	1.60	1.12	1.22	1.47
3	2.15	1.50	1.53	1.92
4	2.47	1.92	1.83	2.34
5	3.14	2.36	2.30	2.39
6	4.09	2.88	2.45	2.97
7	4.33	3.04	2.84	3.72
8	4.61	3.70	2.99	4.31
9	4.86	4.29	4.32	4.71

As demonstrated by Figure 35, more excitable frequencies tend to have higher mode shape amplitudes, which can have an increased probability of facilitating structural failure within the ganged heliostat system. For the measured frequencies, computed values in the 0° orientation of 1.60 and 2.47 were found to be closest matched. Figure 35 provides mode shapes found for these two frequencies where the highest amplitudes were found at 2.55 m, 4.76 m and 7.2 m along the 9.1 m horizontal span of the cables for a 1:20 sag to span ratio.

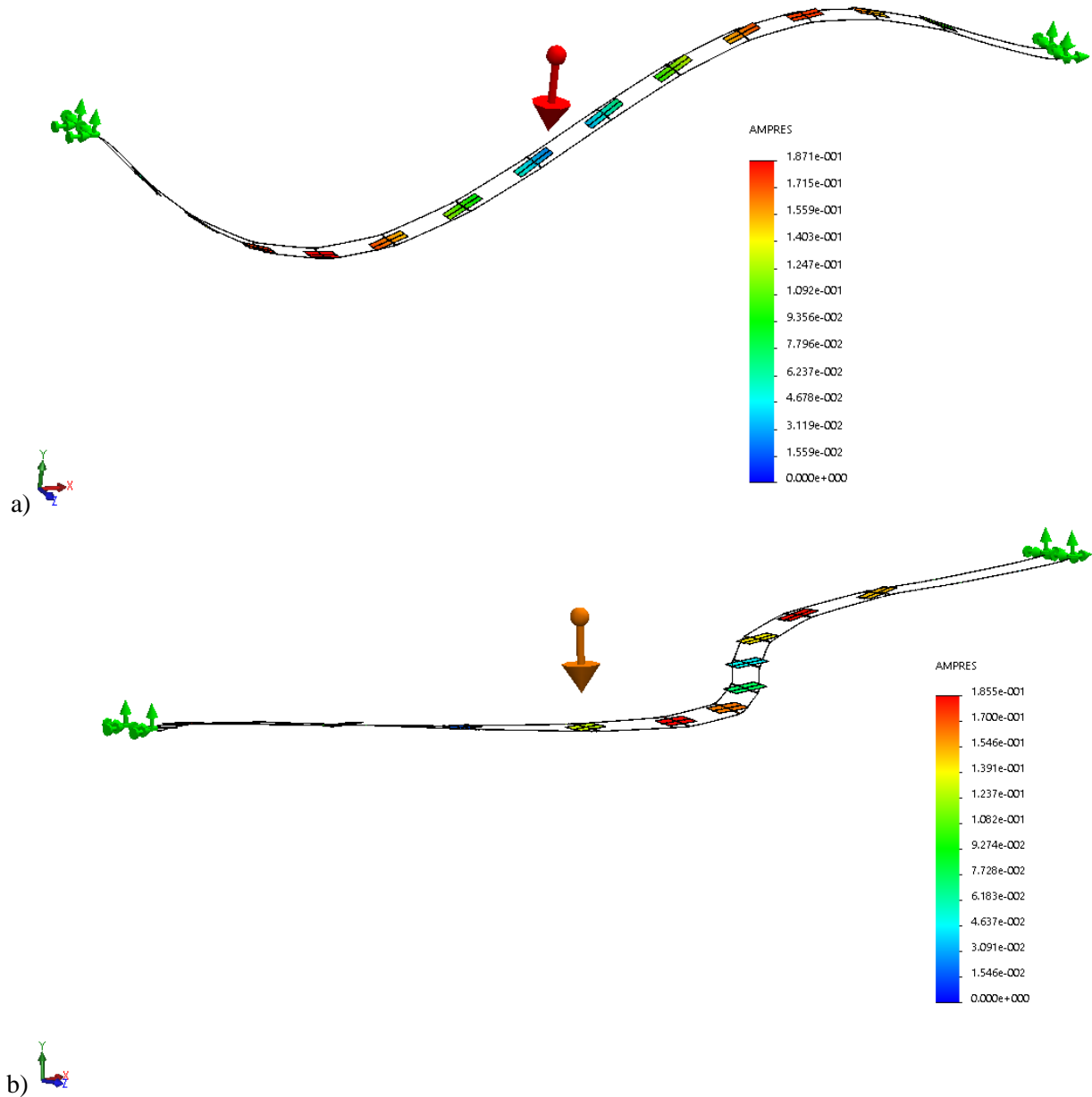


Figure 35. Prototype 3 modes shapes for a) 1.60 Hz and b) 2.47 Hz resonant frequencies in a 0° orientation and under 0 mph wind conditions.

These results indicate the need for dampening for both the Prototype 3 system and its scaled 10 MW counterpart, to avoid destructive modal responses. To address this dampening issue, an analysis was conducted for each respective prototype III orientation where Table GG provides the respective modal maxima locations for the 0° orientation, where dampening can be applied to increase the natural frequency of the system and reduce the risk of modal excitation damage. Similar values were also found for the 45° and 90° orientations as well. Of these the largest amplitudes were on average found at approximately 3.1 m and 4.76 and 7.4 m locations along the ganged heliostat.

OFFICIAL USE ONLY

Table 9. Prototype 3 modal maxima locations for 0°, 45° and 90° orientations determined from the modal analysis.

Mode Number	0° Orientation Frequency (Hz)	Modal Maxima Location (m)	45° Orientation Frequency (Hz)	Modal Maxima Locations (m)	90° Orientation Frequency (Hz)	Modal Maxima Location (m)
1	0.83	4.76	0.69	1.47, 4.50, 7.82	0.71	1.47, 4.09, 6.16, 8.76
2	1.60	2.55, 7.60	1.12	1.07, 2.78, 4.76, 7.18, 9.19	1.22	1.2, 2.77, 4.15, 5.96, 7.47, 8.81
3	2.15	1.34, 4.76, 8.14	1.50	1.69, 3.05, 4.76, 6.75, 8.36	1.53	0.96, 2.22, 3.44, 4.91, 6.16, 7.42, 9.1
4	2.47	1.47, 4.76, 8.14	1.92	0.84, 1.77, 2.92, 4.76, 6.26, 7.42, 9.37	1.83	0.74, 2.12, 3.38, 4.12, 5.46, 6.78, 8.05, 9.1
5	3.14	0.94, 3.41, 5.8, 8.3	2.36	0.80, 2.06, 3.51, 4.77, 6.24, 7.42, 8.91	2.30	1.42, 2.03, 2.94, 4.02, 4.79, 5.57, 6.72, 7.45, 8.36, 9.26
6	4.09	0.8, 2.71, 4.82, 6.79, 8.81	2.88	0.81, 1.35, 2.26, 3.32, 4.18, 5.35, 6.17, 7.25, 8.13	2.45	0.74, 1.47, 2.71, 3.41, 4.40, 5.49, 6.11, 7.42, 8.04, 9.12
7	4.33	1.05, 2.75, 7.42, 8.09	3.04	0.74, 1.75, 2.77, 4.02, 4.86, 6.10, 6.89, 8.14, 8.92	2.84	1.01, 2.01, 2.76, 3.36, 4.12, 4.76, 5.48, 6.18, 6.91, 7.90, 8.61, 9.28
8	4.61	1.69, 3.84, 5.07, 6.73, 8.71	3.70	0.75, 1.42, 3.28, 4.09, 4.82, 6.79, 7.42, 8.14, 9.26	2.99	0.75, 1.41, 2.06, 2.72, 3.50, 4.76, 5.46, 6.05, 6.87, 7.37, 8.13, 9.05
9	4.86	0.8, 2.12, 3.38, 4.82, 6.11, 7.47, 8.76	4.29	2.61, 3.09, 3.80, 4.31, 4.76, 5.49, 5.83, 6.59, 7.12, 7.72	4.32	2.08, 3.52, 4.74, 5.46, 6.02, 6.96, 7.59

4.2.5. Discussion

Modal Structural Implications with Historical Context

The modal excitation of 0.2 Hz, facilitated torsional vibration of two halves of the Tacoma Narrows Bridge to be 180° out of phase with one another, which led to its destruction. Strong winds, which were initially 35 mph excited the bridge's transverse vibration mode, with an amplitude of 0.46 m (1.5 feet) [22]. As the wind subsequently increased to 42 mph, the amplitude

rose to 8.53 m (28 feet) with a 0.69 G peak acceleration. As previously mentioned, the Tacoma Narrows Bridge was originally designed with respect to longitudinal motion and not for torsional motion. For this investigation torsional motion as considered in addition to longitudinal motion, where the lowest modal frequency recorded during tests for Prototype 1 and 3 was 1.19 and 0.74 Hz, respectively. It was determined that the larger PVC pipe arms for each Prototype 1 facet, which were pressed against each other by gravity, facilitated dampening which increased the natural frequency higher than that of Prototype 3. However, both low frequencies were found to be higher than 0.2 Hz where the peak acceleration for both tests was determined based on Equation 7 to be 0.23 G, a third the value of the Tacoma Narrows Bridge.

$$\text{Displacement} \times \omega^2 = \text{Acceleration} \quad (7)$$

$$\omega = 2\pi f \quad (8)$$

where f is the measured natural frequency and the displacement was determined peak-to-peak for a respective mode shape. To further reduce the propensity of the Tacoma Narrows Bridge modal failure within ganged heliostat systems would be to include dampening in strategic locations, which would likely increase the modal frequencies. Finally, another parameter that can be applied in future modal analysis is vortex shedding where prior research by Von Karman [29] showed that blunt bodies within bridge or ganged structures could also shed periodic vortices in their wakes and induce oscillations.

4.2.6. **Conclusions and Future Work on Vibrational Studies**

A rigorous analysis between field-tests of a ganged heliostat and a computational finite element analysis model was performed for three different ganged heliostat prototype configurations. The field modal tests showed good agreement with the system frequency models to within 2.8% for Prototype 1 and 5.6% for Prototype 3, respectively. The Prototype 3 system was developed as a scaled version of a 10 MW ganged heliostat system, capable of facilitating up to 13, 64 m² heliostats over a horizontal span of 175 m. Modal analysis for the 9.1 m span prototype found low-order frequency modes at 1.42, 1.47, 1.48 and 2.34 Hz, which were found to be in close agreement with the Prototype 3 model using SolidWorks Simulation software. These types of tests and validated models can demonstrate the methodology to design a useful modal test for use in characterizing the dynamic response, including both elastic and rigid body modes. Improvements in the models and experimental tests could result in a more accurate predictive model to improve dampening requirements, sensor placement and reduce experimental uncertainty in identifying the most dynamic failure modes for the 0°, 45° and 90° orientation configurations.

There are areas for improvement in this investigation that can be carried out in future work. Prototypes 1 and 2 had issues with facet connections to the cabling, which was adapted to an adjustable fixed connection for better location control of the facets as well reduced azimuth angular variation between the heliostat ends and the center portion of the structure. However, the impact of these fixtures, along with the applied tension values during tracking was not taken into account during modal analysis. Future work would need to consider these features along with applied dampening solutions, based on the prescribed locations from simulation, to determine if the natural frequencies can be increased for vertical, horizontal and torsional modal excitations. Since low levels of wind was present intermittently during testing, an improved wind wall will need to be erected with wind-generation equipment to validate wind-excitation models for all three

OFFICIAL USE ONLY

orientations. Additionally, the experimental modal excitation methodology used during Prototype 1 testing will need to be applied to the next subsequent prototypes to reduce measurement error and for assessing a larger, more comprehensive set of mode shapes and frequencies. Finally, future experimentation work will need to investigate the coupling between modal excitation with mechanical stress distributions and structural failure, as well as with optical performance over a range of operational system rotations, facet pitch levels and cable tension levels.

5. OPTICAL ANALYSIS

This section describes the optical modeling and analyses performed, which includes developing conceptual 10 MW electric power tower plants, one with conventional heliostats and the other with ganged heliostats. For both models the subsequent subsystems after the collector field were kept the same. The optical efficiencies were then compared between the conventional heliostat and ganged heliostat fields. The ganged heliostat field was semi-optimized for high optical efficiency. Due to time constraints, a global optimization was not performed which perhaps would have included optimizing on the tower height, cable spans, cable span-to-sag ratio (i.e., cable tensions), incorporating the ganged heliostats cost parameters, and alternative field configurations such as East-West spans, radial spans, or circumferential spans. The ganged heliostat field is cost efficient when constructed on natural rolling hills terrain where no land modifications are needed. Several locations in the US Southwest were identified with such terrain that potentially could support deployment of a ganged heliostat field. Conceptual field layouts are also provided over two of the locations identified.

The tracking performance on the small-scale prototypes was also evaluated. As described in previous sections, the tracking control mechanisms were crude adjustments with linear actuators for rotation arms adjustments and cable tensions, and manual hand adjustments on the mirror pitch angles. We assumed with better control mechanisms the tracking accuracy can be improved by 2-3x. A full tracking algorithm was not developed since it was outside the scope of the work, but the initial study performed and the learning developed in this work will provide the foundation for developing a tracking algorithm in future work.

In the concept for a deployed system, the grouped heliostats are supported by two parallel cables (e.g., 31.75 mm diameter, 6 x 37, steel), spaced approximately 4.5 m apart. The horizontal cable spans can range from 150-250 m and hold 8 to 14, 64 m² heliostats, depending on the span lengths, cables used to maintain 3-4 safety factors on the cable tensions, and their position relative to the tower. A schematic of one span of heliostats concept, forming a catenoid, is shown in Figure 36. Each heliostat will be actuated in local pitch angle by a linear actuator with approximately 1500 kg thrust. The cables will terminate at a rotational arm supported by a post at each end. The rotational arms will rotate about horizontal axles, which are parallel to the supporting cables, and are located at the top of the posts. Each rotational arm could be actuated by a gear-reduced electric motor or something similar. As shown in the optical model in Figure 37, a total of six posts support five ganged heliostats in each column, the inner four posts share support of five ganged heliostats. Posts are 2-4 m high, which assumes the proper terrain (i.e., rolling hills).

Three optical modeling tools were used. First is the System Advisor Model (SAM) [33], which models the complete power tower system, evaluates the model performance and calculates the levelized cost of energy (LCOE) based on the system performance and cost parameters that are input. The second tool used is SolarPilot, a ray tracing tool, which was used to evaluate the heliostat field optical performance. The third tool is SolTrace [34], which is another ray tracing tool used for flux evaluations at the receiver location and 3D visualizations of the field layouts.

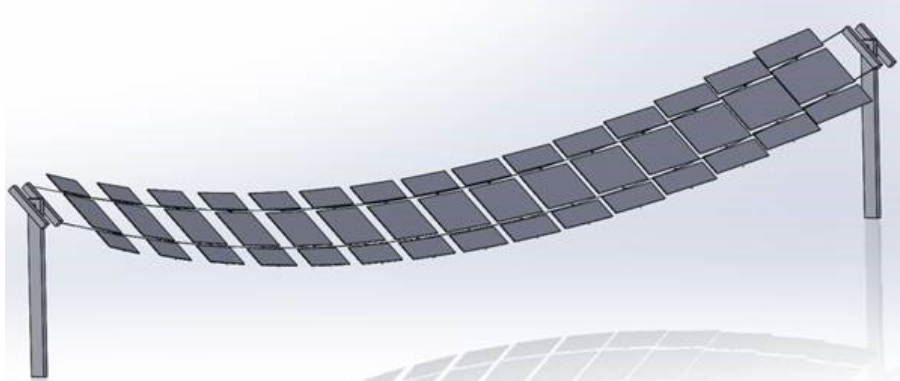


Figure 36. Schematic of a single span of the large-scale tensile ganged heliostat concept.

5.1. 10 MWe Power Tower Plant Modeling and Simulation

A heliostat field size (surround field) sufficient for providing input flux to a 10 MW-electric power tower plant was modeled in the SAM, first using conventional heliostats and then using the tensile ganged heliostats. For the conventional heliostat field, the SAM optimization algorithms were used which balances the costs and optical performance to establish an optimum field layout; typically, it will be a radially staggered surround field (see Figure 40). A north field with a cavity receiver was considered, but currently SAM does not support cavity receivers, and therefore an external cylindrical receiver with a surround field was used for comparisons between the two different heliostat field configurations.

For the ganged heliostats, the collecting field is an array of 41 parallel rows of heliostats, each row comprising five ganged heliostats (see Figures 37 and 41). Each ganged heliostat reflective strip (or horizontal span) is 175 m long with 8 to 14 heliostats per strip. The cable span-to-sag ratio is 20, or 8.75 m sag to the bottom of the catenoid. In the first iteration of the field layout design, the heliostats were equally spaced along the cables with the same number of heliostats per strip without regard to shading, blocking and other optical losses. The heliostats are single-axis actuated mirror modules of 64 m² aperture each. Initially it is assumed that the cables supporting the heliostats follow a parabolic profile. Mechanical modeling determined the actual profiles of the cables. For the case when the heliostats were equally spaced, the optical performance evaluation in SolarPilot showed significant blocking losses, which reduced the overall optical field efficiency to 25-30%. The next step was to reduce the blocking losses (i.e., blocking the receiver's view from neighboring heliostats). Since there are no algorithms in existent for optimizing tensile-based ganged heliostats, custom code was developed in Matlab that eliminated the blocking losses. The development of this code is discussed in the section below. After the algorithm was applied, the new field was evaluated in SolTrace and SolarPilot. The blocking efficiency increased to > 90%, and the overall optical field efficiency improved to > 60% (at solar noon on equinox) almost matching that of the conventional heliostat field. The SolTrace model of the 10 MW plant using tensile ganged heliostats is shown in Figure 37.

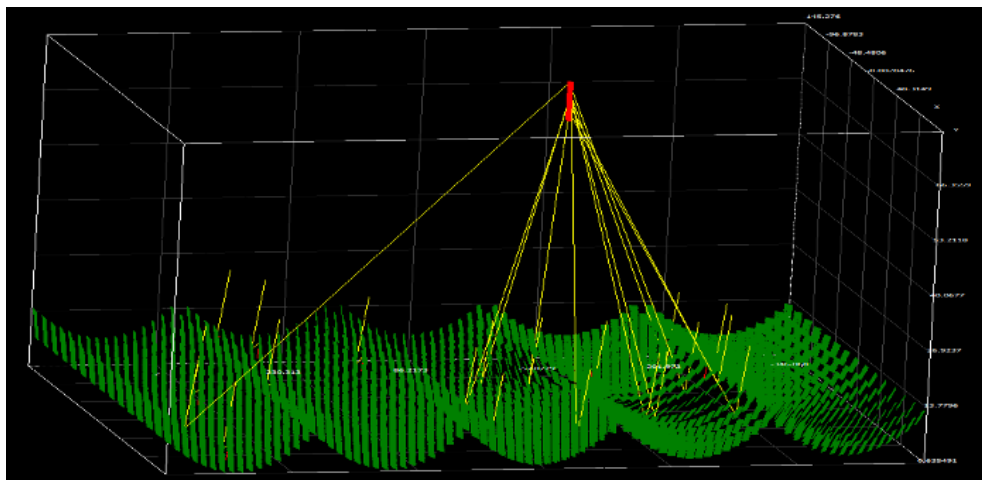


Figure 37. 10 MW field modeled in SolTrace for cable-suspended ganged heliostats. A few traced solar rays (yellow lines) are shown.

The SolTrace field model of the ganged heliostats was transferred to SAM. The SAM model with the conventional heliostat field was taken and the field was replaced with the ganged heliostat field, thus keeping the rest of the subsystem (i.e., receiver, power block, etc.) unchanged, except for the tower height. The initial results of the comparisons between the two field configurations are provided here and discussed in the next section.

Using the SAM field optimization algorithms, the baseline model with the conventional heliostat field optimized to a tower height of 62 m, which yielded the lowest LCOE. The ganged heliostat field layout was optimized to a tower height of 75 m, which was initially specified by Skysun. An optimization on the tower height was not performed in this study, but could be performed in future work. The trade-off is a taller tower will alleviate the blocking and shading losses for a set field size; a shorter tower will have lower cost but blocking and shading losses will increase necessitating an increase in the field size and land area, which will increase cost. Table 10 shows the parameters used for the two models. Since the tracking algorithm for cable-suspended heliostats was not developed as part of this work, an assumption was made on the ganged heliostats. That is, the suspended heliostats were assumed to have independent azimuth and elevation tracking axes.

Table 10. Parameters for the 10 MW_e power tower model.

Parameter	Conventional Heliostat Field	Ganged Heliostat Field
Location (default)	Daggett, CA	Daggett, CA
Optical Slope Error per Axis (mrad)	1.53*	2
Heliostat cost (\$/m ²)	120**	75***
Heliostat Reflective Area (m ²)	64	64
Mirror Reflectivity	0.9	0.9
Canting Strategy	On-Axis	On-Axis
Number of Heliostats	1919	1988
Tower Height (m)	62.8	75
Tower Cost (\$M)	6.08	6.98
Land Area (acre)	216	288
Field Annual Optical Efficiency (%)	47.8	44.7
Total Installed Cost (\$M)	85.97	80.90
Total Annual Energy Produced (GWh)	53.49	51.00
LCOE (real) (¢/kWh)	10.63	10.58

* SunShot target for optical slope error.

** Estimated current heliostat cost, or cost goal for 2018 Power Tower Roadmap.

*** Skysun cost estimate.

In SAM the Annual Optical Efficiency is calculated as the kWh (kilowatt-hour) thermal incident on the receiver in a full year, divided by the number of kWh incident on the field in a full year. Also the second number is stated as the product of direct normal irradiance (DNI) and the area of the heliostats, which is the kWh that would fall on the field if the heliostats tracked the sun rather than a point in between the sun and the target. This allows capture of cosine loss, the largest loss in a heliostat field. Note that this calculation also puts DNI in the denominator when the winds are too high, and when the DNI has not been high long enough to run the plant, so it is a fairly simplified number.

The optical slope error parameter accounts for all the optical errors: mirror slope error, tracking errors, canting errors, and stability (e.g., wind induced). The 1.53 mrad value listed in Table 10 is the SunShot target in both tracking axes. The ganged heliostat field was assigned 2 mrad because it was assumed the tracking error is will slightly be higher; this will need to be better quantified on future prototype systems that have better tracking control (i.e., actuation) mechanisms. The prototypes evaluated in this study had crude adjustments as described previously, which did not accurately quantify the tracking accuracy; the estimated tracking accuracy was approximately 4 mrad on the Prototype 3 set up. It was assumed a system with better control mechanisms would be better by 2-3x in tracking accuracy.

Figure 38 shows the how the two field configurations compare on the annual energy produced and total installed cost. The plot shows that the cost is higher but the energy production is also higher for the conventional plant. Figure 39 shows the cost breakdown of the subsystems of the plant. Note that only the heliostat and tower cost are different, and the rest of the subsystems

and other costs are essentially the same. Also note that for the ganged heliostat field, a global optimization was not performed. A global optimization may show additional improvements.

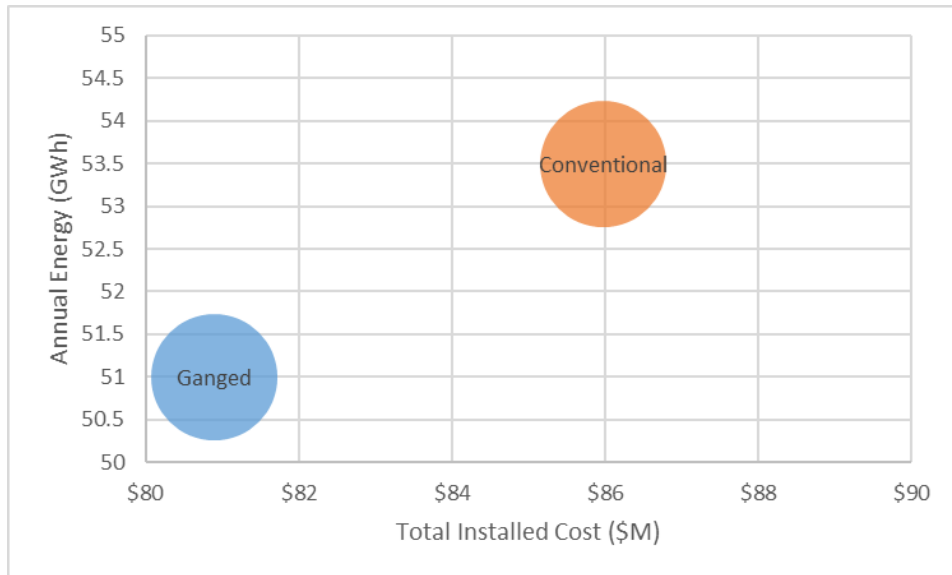


Figure 38. Comparison on annual energy production vs. installed cost.

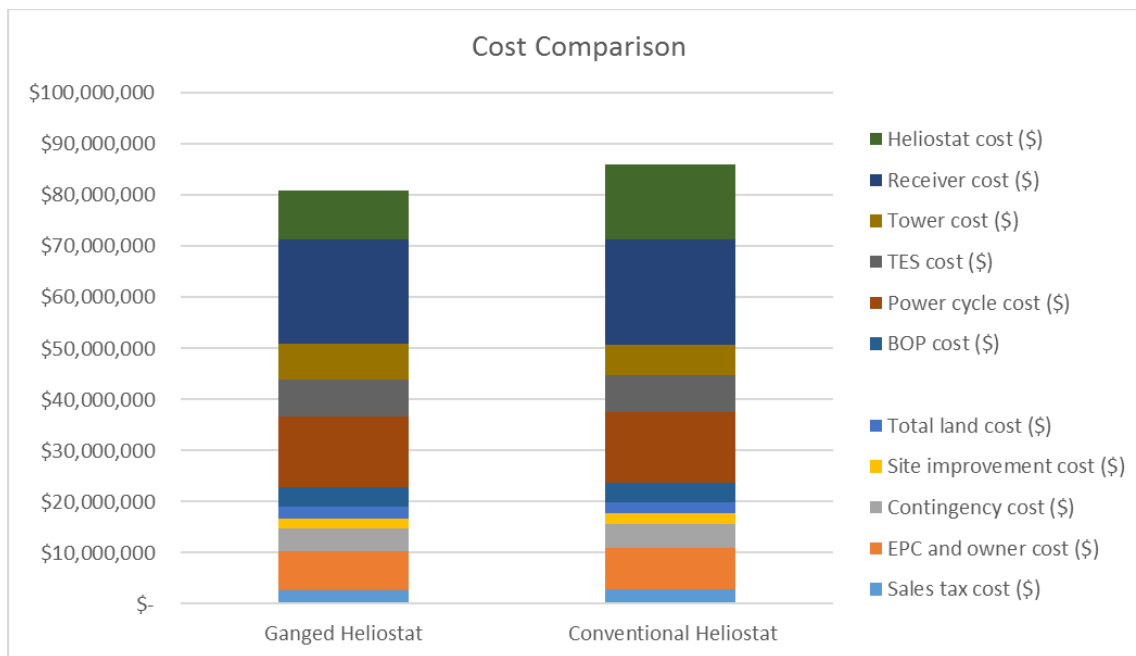


Figure 39. Plant cost breakdown for the two field configurations.

The LCOE is virtually unchanged, because the reduced cost of heliostats (\$75/m² compared to conventional \$120/m²) is offset by the reduced performance of the ganged heliostats, estimated in this study at 2 mrad in each direction compared to conventional 1.53 mrad. In order to meet SunShot goals, performance must be maintained while cost is reduced. The ganged heliostat field would benefit from optical error improvements, which mostly means the tracking accuracy needs to be on par with a conventional heliostat. The tower cost is slightly higher for the ganged heliostat

due to the taller tower to avoid shading and blocking. Again, a global optimization, which would include optimizing on the tower height, might improve on the tower height and cost.

5.2. Optical Performance Evaluation

The field optical performance typically includes the blocking, shading, intercept, cosine loss performance and the mirror reflectivity. Blocking is defined as the rays being blocked by neighboring heliostats from reaching the receiver surface, while shading is defined as the neighboring heliostats blocking the sun rays from reaching the target heliostat surface. The intercept loss accounts for the reflected rays that do not reach the receiver surface. Cosine loss accounts for the reduced useful heliostat reflective area (i.e., its projected area) due to its orientation while tracking the sun. The south side heliostats in a surround field (for latitudes $> 0^\circ$) typically have high cosine losses compared to the north side heliostats.

Figure 40 shows the radially staggered heliostat surround field (conventional field) optimized in SAM for 10 MW_e plant for comparison to the ganged heliostat field, which is shown in Figure 41. The parameters for the heliostat fields are listed in Table 10. The colorbar scale in the plots show the overall optical efficiency where the average is 63.8% for the conventional field at equinox, solar noon. The conventional field assumes flat land.

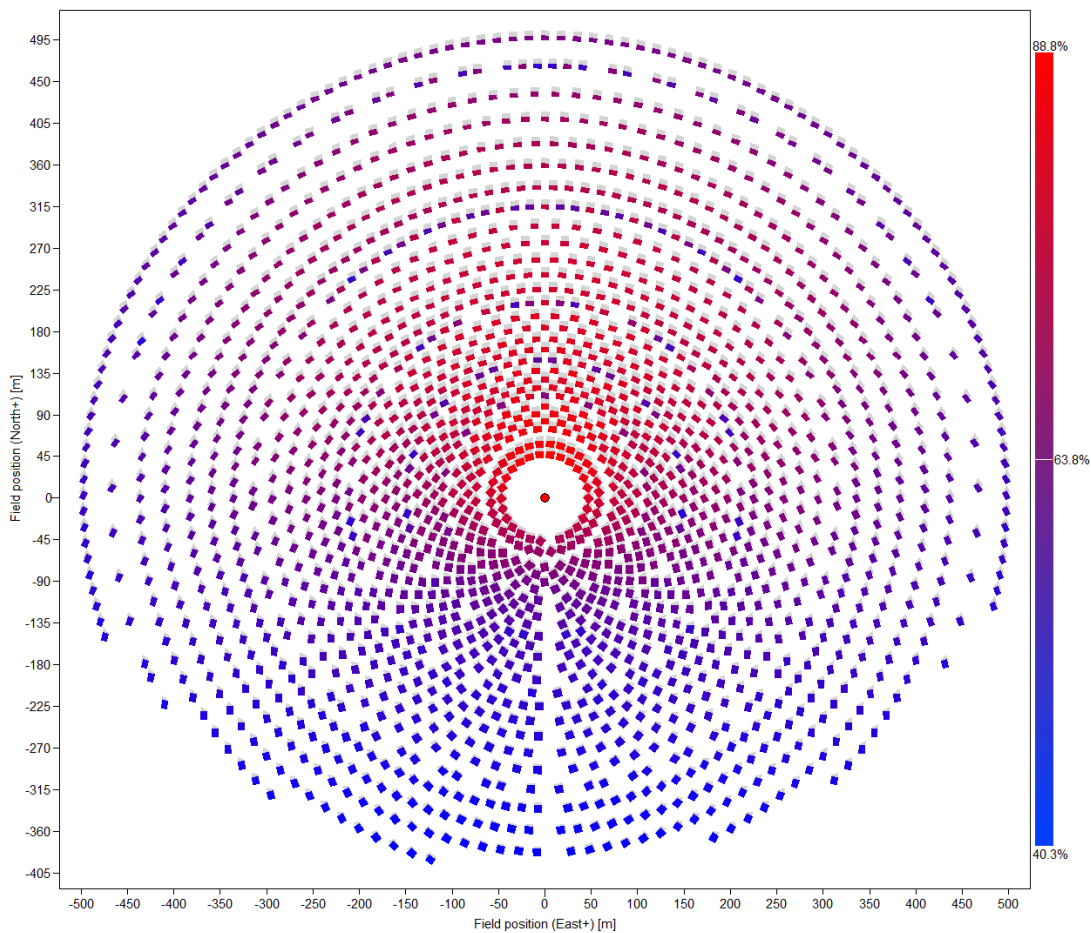


Figure 40. Radially staggered heliostat field optimized for a 10 MW_e plant using SAM optimizer routine. The average heliostat efficiency is 63.8% for solar noon at equinox.

In the initial field layout of the ganged heliostats, the heliostats on the cable spans and the columns of heliostats were equally spaced and the same number of heliostats was mounted on a span, which showed high blockage drastically reducing the total optical field efficiency. Since blockage was dominant, custom Matlab code was developed to place heliostats for reduced blockage. The resultant field plotted in SolarPilot is shown in Figure 41. The heliostats are now unequally spaced along the cable spans, the number of heliostats per span range from six on the north end to 14 on the east and west ends of the field, and column spacings are also staggered. This arrangement reduced the blocking impacts and made more efficient use of the land. After improvements on the blocking, the annual field efficiency increased to 62.2% for the equinox, solar noon design point, almost matching that of the conventional field.

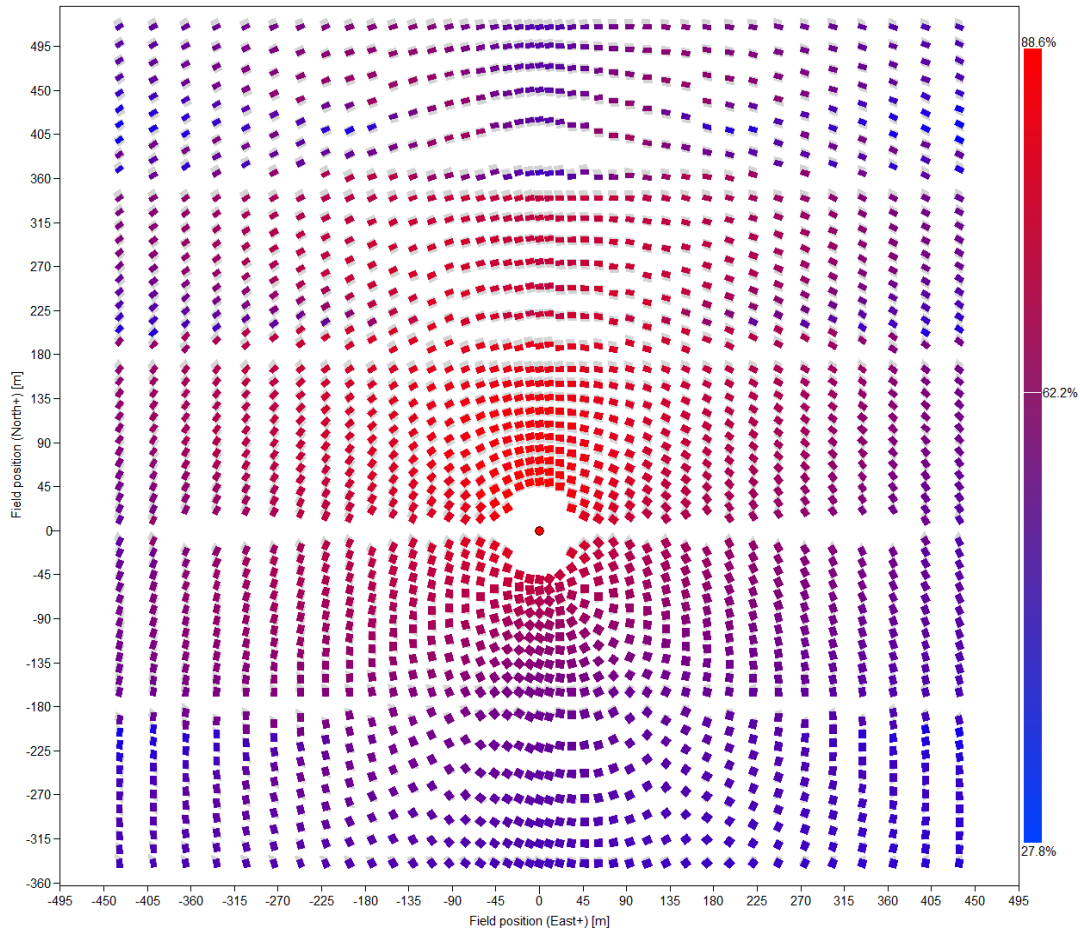


Figure 41. Cornfield type heliostat field layout optimized for minimal blockage. There are five rows and 41 columns of ganged heliostats. The average heliostat efficiency is 62.2% for solar noon at equinox.

In Figures 42-46, optical efficiency and components of the optical efficiency (blocking, shading, intercept efficiency, etc.) are provided for several days in the year, namely the solstices and equinox. Each plot is evaluated from 4 am to 8 pm solar time for Daggett, CA location.

The total optical efficiency of the ganged heliostat field slightly lags the conventional field (baseline). However, this is only after improving on the blocking efficiency. A global optimization may improve on the optical efficiency of the ganged heliostat field further. In

December, the ganged heliostat field lags conventional more around solar noon. However, performs slightly better in the early morning and late afternoon.

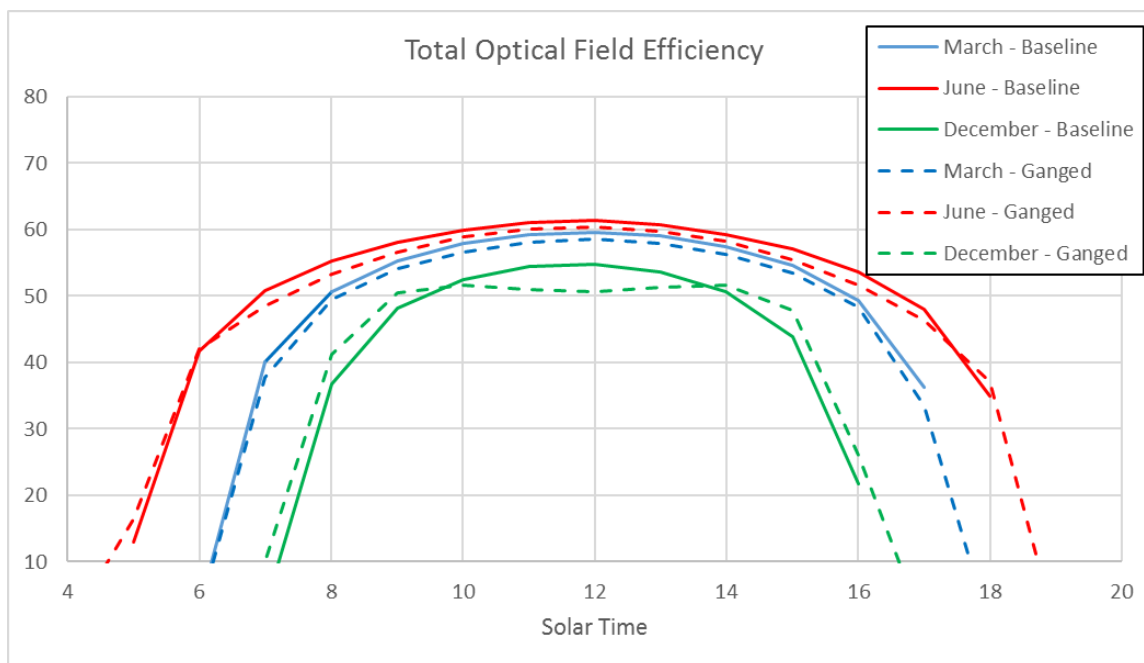


Figure 42. Total optical field efficiency for conventional and ganged heliostat fields.

The blocking efficiency of the ganged heliostat field lags the conventional field. However, the blocking efficiencies for both fields are relative high ($> 95\%$). The blocking efficiency for the ganged heliostat field may further be improved, however, a trade-off was considered between cost and performance. When blocking losses were eliminated, some heliostat spans (especially on the north end of the field) ended up with low density heliostats (< 6 per span). From the cost analysis, it was determined that to maintain a cost advantage, six heliostats per span would be the minimum. For the spans with low heliostat density, blockage up to 15% was allowed to add more heliostats within a span until a minimum of six heliostats per span was achieved.

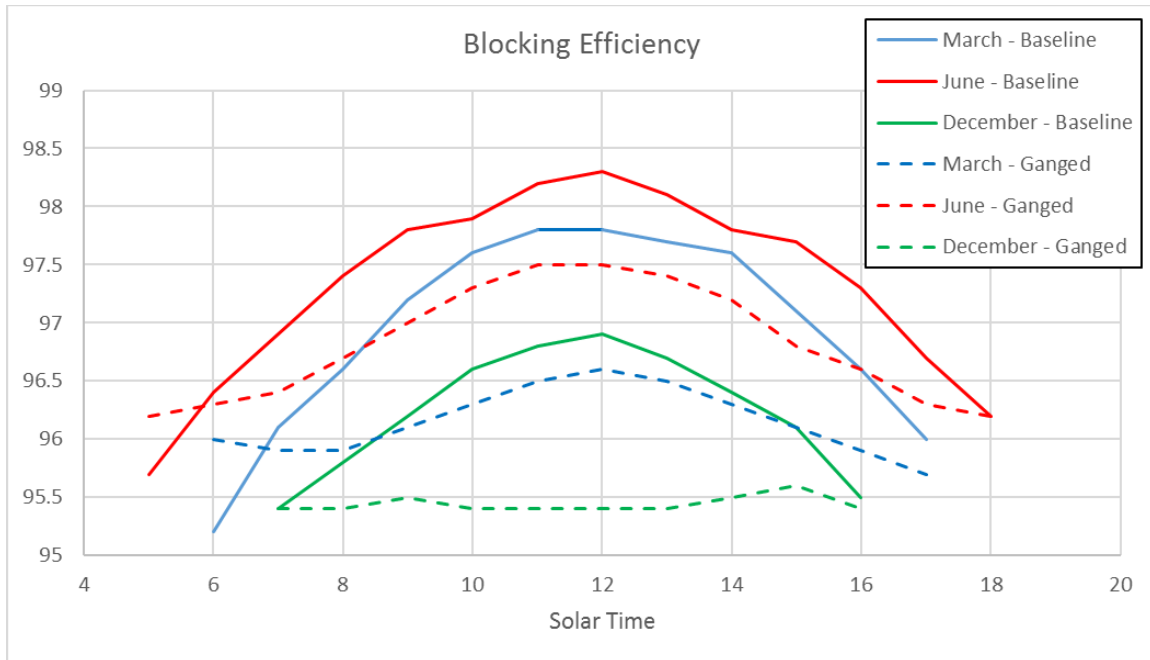


Figure 43. Blocking efficiency. Blocking of reflected rays to tower. Slightly greater impact in winter for the ganged heliostats.

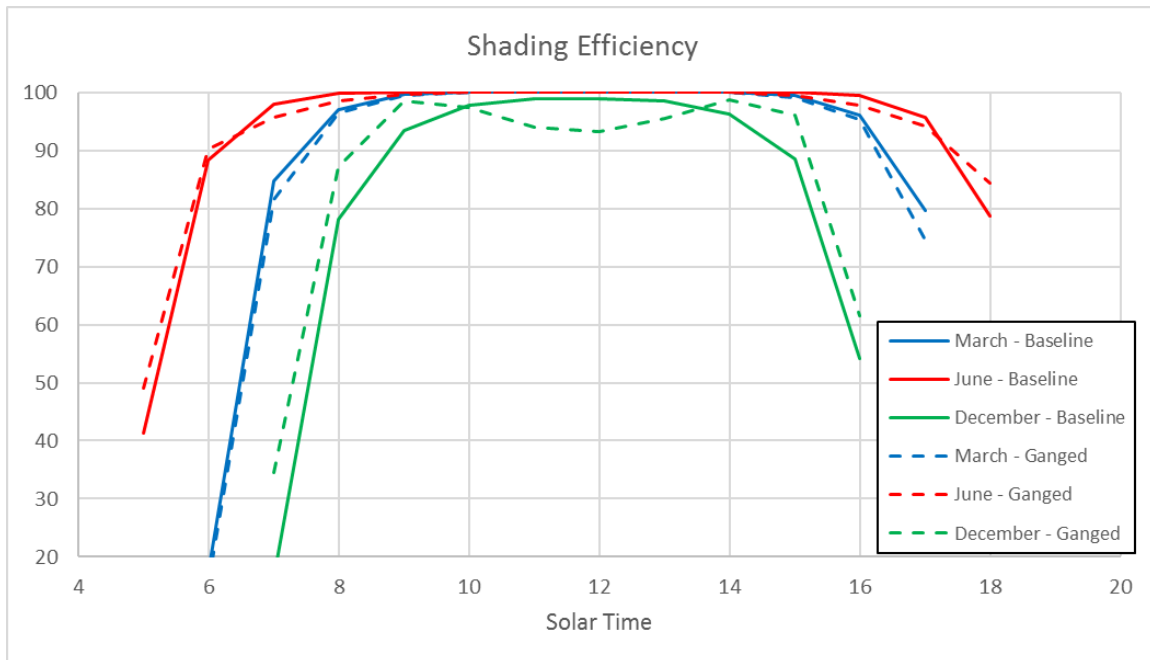


Figure 44. Shading efficiency. Blocking of sun rays to the heliostats.

The intercept efficiency for the ganged heliostat field lagged the conventional field mostly because of the assumed higher slope error (2 mrad) for the ganged heliostat field. The higher slope error is due to the assumption that the tracking for the ganged heliostat would be higher. If the tracking error is proven to be better in future prototypes, then the intercept factor can be improved on.

The cosine efficiency depends on the placement of the heliostats in the field relative to the receiver. Typically, in a surround field the south side of the field will experience higher cosine

losses. Figure 46 shows slightly better cosine efficiency performance for the ganged heliostat field because of the taller tower at 75 m.

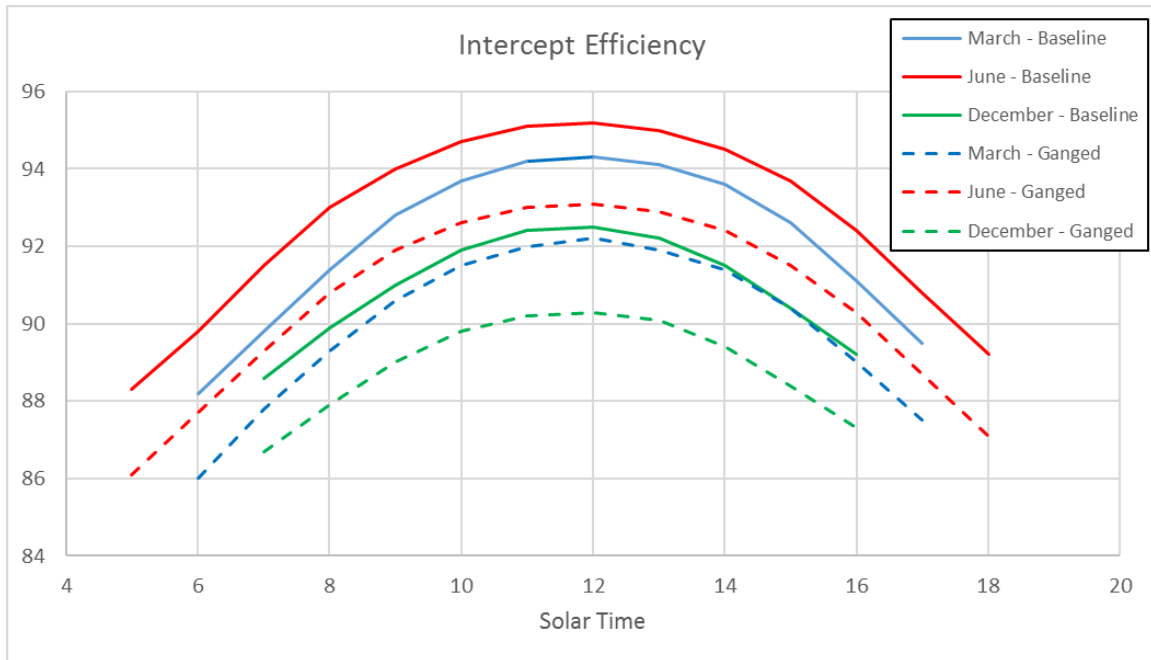


Figure 45. Intercept efficiency. Intercept of reflected rays by the receiver.

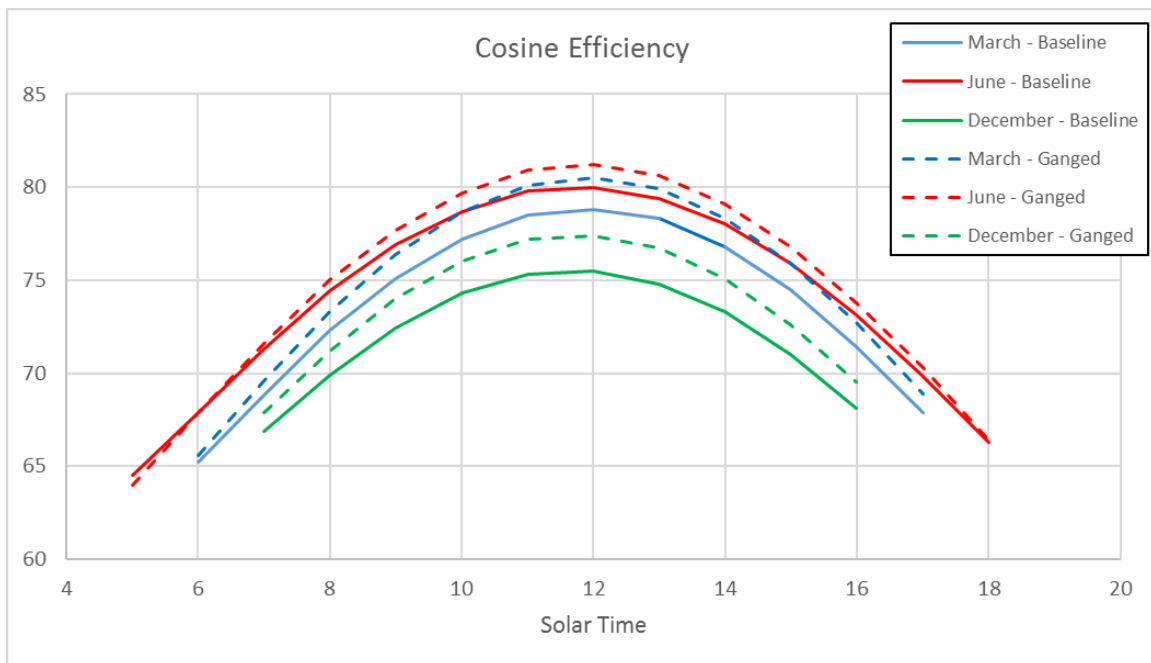


Figure 46. Cosine efficiency.

5.2.1. *Field Configuration for Minimal Blockage with Constraints*

Figure 47 below illustrates placement of the heliostats along the catenary, formed by the two guide cables, for zero to minimal blockage. Blocking refers to the ability of each heliostat to “see” the receiver. If the heliostats are obscured by other neighboring heliostats, then the blocking efficiency is reduced. As mentioned above, initial ganged heliostat field model with equal spacing on the heliostats showed high blockage, which drastically reduced the overall annual optical efficiency. It made sense to reduce the blockage first. The heliostat span shown in Figure 47 is the first span just north of the receiver tower. The heliostat with the blue outline is first heliostat placed at 10 m away from the end post. The next heliostat (green outline) is moved along the cable catenary until the zero blockage condition is met. The initial catenary profile was determined from the design cable span distance and the span-to-sag ratio, which initially was set to 20. The red dashed box is the projection of the previous heliostat onto the plane of the current heliostat being moved while the heliostats are pointed directly at the receiver. The heliostats are assumed focused to slant range (i.e., distance to the receiver). If the red projected outline clears the next heliostat (i.e., no intersection), zero blockage is satisfied. This process is repeated for the rest of the heliostats and all other spans in the field. To satisfy the no blockage condition, the heliostats must become unequally spaced.

The weight load constraint on the cables allowed up to 14 heliostats per span. To maintain a cost advantage a minimum of six (6) heliostats on a span was also applied. For spans that are further away from the tower, the heliostat spacing need to be increased to keep the blockage to a minimum thus the heliostat density can get low (e.g., < 6 per span). For these spans, blockage of up to 15% was allowed to add extra heliostats until the constraint of six heliostats per span was reached.

For unequal heliostat spacing, the catenary profile becomes nonsymmetrical as shown in Figure 12 in Section 4.1.2 because the weight load shifts to one side. This coupled mechanical-optical process was not incorporated into the heliostat layout code but will be incorporated in future work. The unbalanced catenary will cause the heliostat positions to shift slightly from the initial hyperbolic profile.

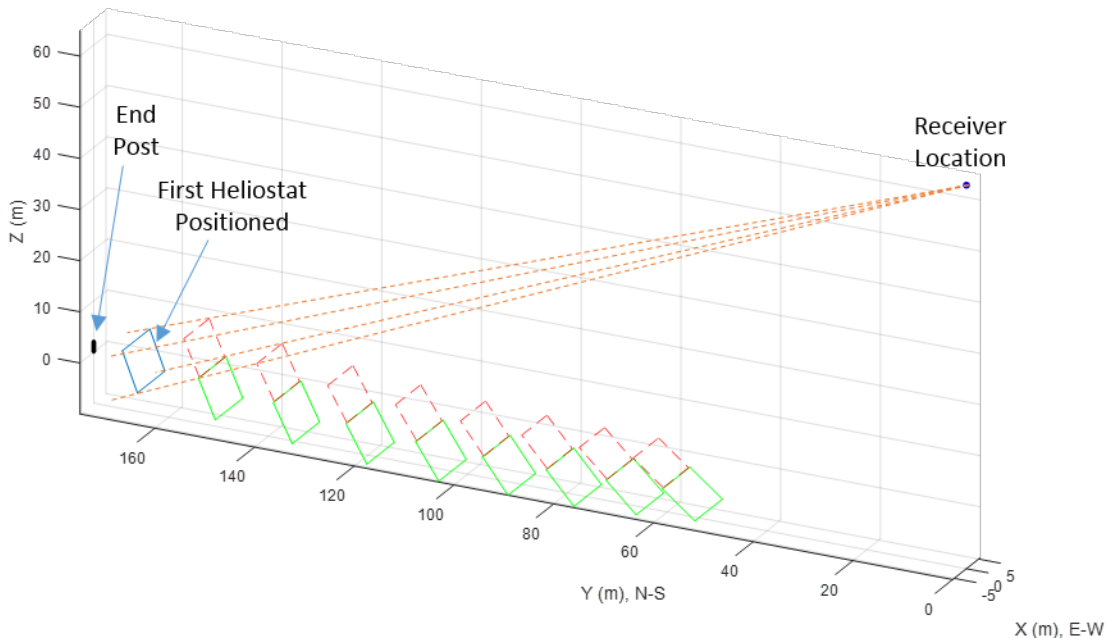


Figure 47. Illustration of heliostat placement along the catenary for no blockage. The cables are not drawn in the figure. The first heliostat (blue outline) is positioned first 10 m from the end post. Subsequent heliostats are placed for no blockage. The heliostats become unequally spaced.

5.3. Alternative Field Layouts

A tensile based cost-effective ganged heliostat presents a substantial shift from the current art in heliostats. The design space is large which allows for further cost reduction as this method evolves. Utilizing the same patented methodology described in this report, namely tensile members acting as both supporting structure and focusing means, three variations emerged showing promise to further reduce system cost. These variations are: radial span layout, diagonal spans in conjunction with described parallel spans and cable supported spans. All three variants reduce the number of required posts/foundations, which account for just over 10% of installed collecting field cost. These alternative heliostat layouts were not evaluated in this work, but Skysun, LLC looks forward to continuing development of these cost-saving design variations.

Radial Spans

Here, multiple cable-supported ganged-heliostat spans radiate from the power tower base. The tower base, up to a height of 15 m to 20 m, is augmented with increased mass of non-engineered steel and concrete to survive the increased forces imposed by the multiple spans. The augmented base height of 15 m to 20 m would be adequate to accommodate 32 spans, including rotational arms, supporting 700 to 800 heliostats, each 64 m². The far ends of the spans terminate to a post assembly as previously described. Such a unit, when optimized for 4 hours thermal energy storage (TES), would be capable of 4 to 5 MWe. Similar sub-units without a power tower surround the central unit with the power tower, with span ends sharing posts. This layout significantly decreases the number of posts required for collecting fields capable of producing 40 MWe and up to 100

MW_e. A radial span approach promises additional savings of \$4.50/m² to \$5.50/m² reducing the glass on metal baseline to below \$70/m² and the lightweight heliostat baseline to below \$60/m².

Additional Diagonal Spans

Additional ganged heliostat spans run diagonally between posts shown in Figure 48 below. The majority of collecting field posts support four spans instead of two decreasing the number of posts required, however post assembly mass increases. This indicates best placement of diagonal spans will likely be in the span areas with fewer heliostats and lower tensional forces, particularly north and south central areas of the collecting field. Preliminary field testing, April 2017, demonstrated similar tracking and focusing compared to the north/south aligned spans.

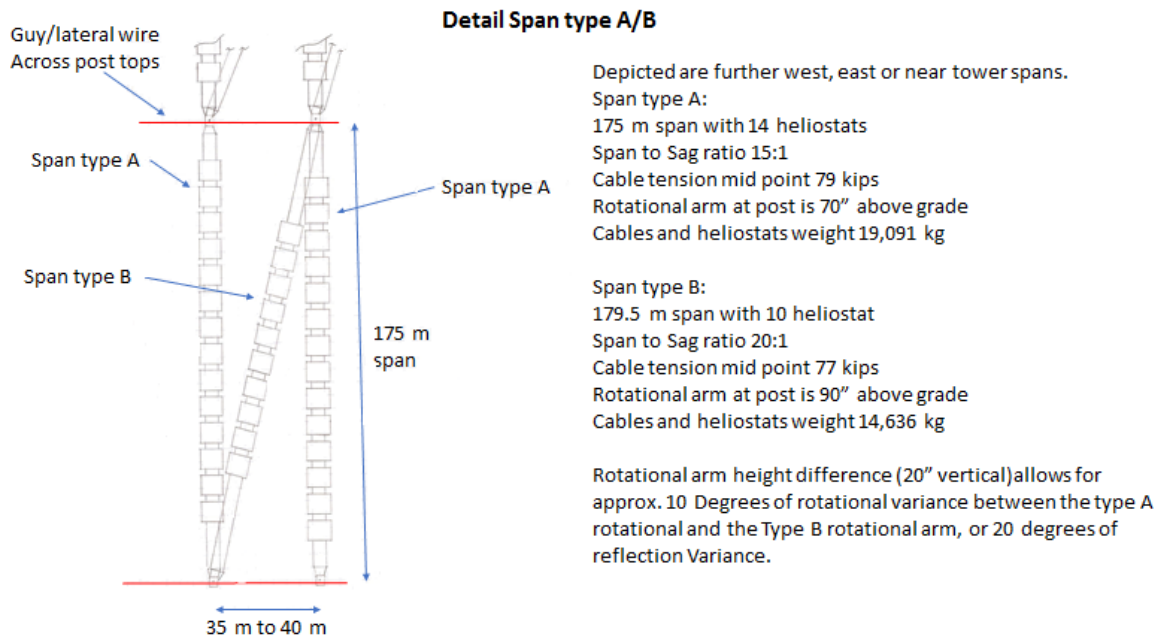


Figure 48. Additional diagonal span to increase heliostat density per land area.

Cable Supported Spans

Like the diagonal span variant, cable supported ganged heliostat spans are best situated in areas of fewer heliostats per span in the north/south central portions of the collecting field. Here, cable(s), transversely strung from one post to its adjacent counterpart post, carry a ganged heliostat span. To minimize shading/blocking the supporting posts must be higher to accommodate cable sag, this drives up post cost.

Table 11. Advantages and potential drawbacks of adding diagonal spans.

Pros	Cons
<ul style="list-style-type: none"> Added stability from guy wires Field physical size about the same with 13% more heliostats Significant drop in post count, was 244, for the 10 MWe with 4 hrs. TES, now 162 with cost savings implied, greater than the cost increase of taller posts and increased mass/foundation to withstand new tension forces. 	<ul style="list-style-type: none"> Spans with most heliostats have increased sag to roughly 17:1 to keep tension acceptable Shading and blocking increases.

5.3.1. Layout Over Actual Terrain

Several possible site locations were investigated utilizing topographical information generated by the United States Geological Survey (USGS) and Google Earth. Sites were chosen to be similar in characteristic to the idealized array presented above. Sites incorporated ganged heliostat lengths of 125 m to 205 m. Reflector area is expected to be 25% of site area. High insolation areas of the U.S., with suitable terrain, offer multiple GWe potential. Reflector area of larger surrounding field expected to be 10% to 25% of the site area. This may be substantially increased by using taller posts over flatter terrain, although at a cost penalty. High insolation areas of the U.S., with suitable terrain, offer multiple GWe potential. Two sites are presented in Figures 49 and 50.

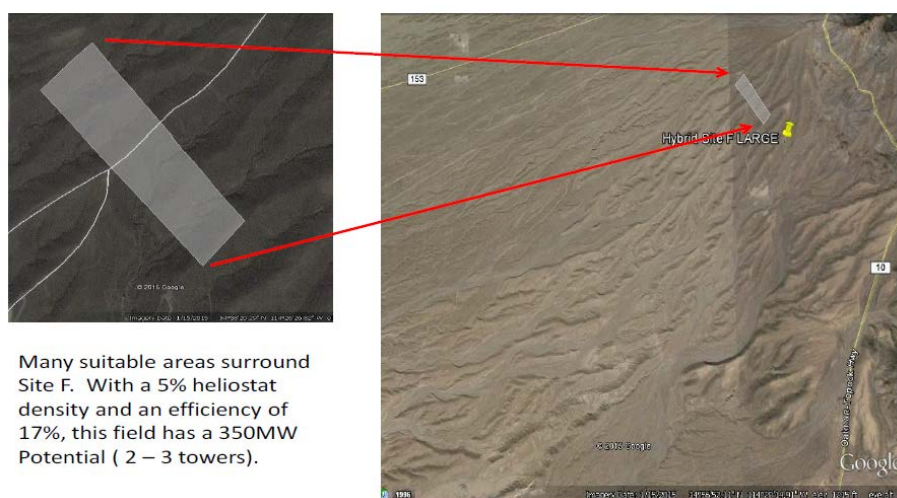


Figure 49. Site F – gray highlighted area (25% heliostat density), located just south of Bullhead City, AZ (943 m x 250 m) with 10-12 MW potential.

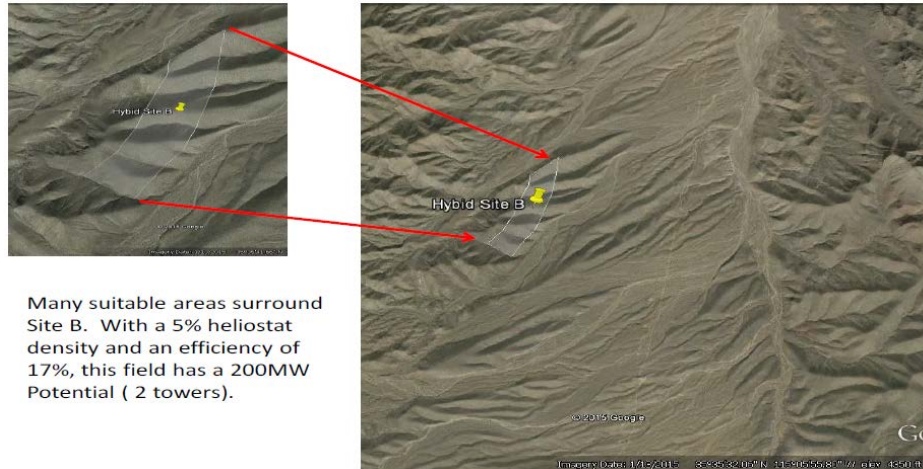


Figure 50. Site B – gray highlighted area (25% heliostat density), located just northwest of Searchlight, NV (1327 m x 314 m) with 15-20 MW potential.

Other Possible Siting Candidates

Earlier research focused on utilizing relatively steep grades and to accommodate lower span/sag ratio values, typically having a value of 10 to 15. However, it was found that to optimize optical efficiency, and improve accuracy, a higher Span/Sag ratio is preferred. A span/sag of 20 is the current design point, this significantly increases the number of likely sites. Table 12 lists 12 potential sites situated in the Southwestern United States. Additionally, numerous site candidates exist in Mexico, Southern Spain, MENA, China, Australia and Chile.

Table 12. Potential sites in the US Southwest for ganged heliostats deployment.

Latitude	Longitude	Site Capability (MW _e)	Nearest Larger City	Distance to that City (Miles)
32.27	-105.24	100 to 200	Albuquerque	200
32.98	-105.26	750 to 1000	Albuquerque	150
34.60	-107.3	50 to 100	Albuquerque	50
31.86	-110.56	300 to 400	Tucson	30
31.64	-110.74	400 to 500	Tucson	40
34.98	-113.74	300 to 500	Las Vegas	100
35.12	-114.5	500 to 700	Las Vegas	60
36.6	-115.27	150 to 200	Las Vegas	35
36.12	-115.6	150 to 250	Las Vegas	25
36.56	-117.3	150 to 200	Los Angeles	175
37.86	-117.91	100 to 200	Fresno	125
38.71	-118.41	100 to 200	Fresno	150

5.4. On-Sun Tracking Evaluation

The development of the tracking algorithm was outside the scope of the work, which would require developing mathematical algorithms and control schemes to perform autonomous on-sun tracking. However, the evaluation of the on-sun tracking was started, and manual on-sun tracking was demonstrated, first by Skysun and then by Sandia. Unlike conventional heliostats which each have rotation drives that provide independent azimuth and elevation control, the tracking on the cable-suspended ganged heliostats is nontrivial in terms of angle motions which could be coupled. The rotation actuators at the end-posts provide rotations of the cables in roll to mimic azimuth for ganged heliostats aligned north-south; elevation if aligned east-west. For the north-south orientation, the pitch angle rotation on each heliostat provides some elevation motion. Initial characterization showed the actuators do not provide pure azimuth and elevation motion but are coupled. The azimuth and elevation coupling becomes significant for large roll angles on the cables.

The small-scale prototype system installed at Sandia was used to help develop an understanding of the on-sun tracking control of the system. The prototype system, however, was a crude system with linear actuators (Figure 52b) for rotations of the end points that was manually controlled. The individual mirror pitch rotation was manually adjusted by hand and locked in position using a set screw. The cable tensions were also controlled with linear actuators (Figure 52c). The cable tensioning compensated for the toroid needed in the reflective strip for accurate on-sun tracking. When both rotation arms were rotated unevenly, a toroid was formed in the reflective strip. It is suggested the shape of the toroid depended on the coupled cable dynamics, which are impacted by the weight load distribution on the guide cables. This hypothesis was not studied because it was outside the scope of the work. In future studies, this will be studied to develop a better understanding. Figure 51 demonstrates the angle and tension adjustments.

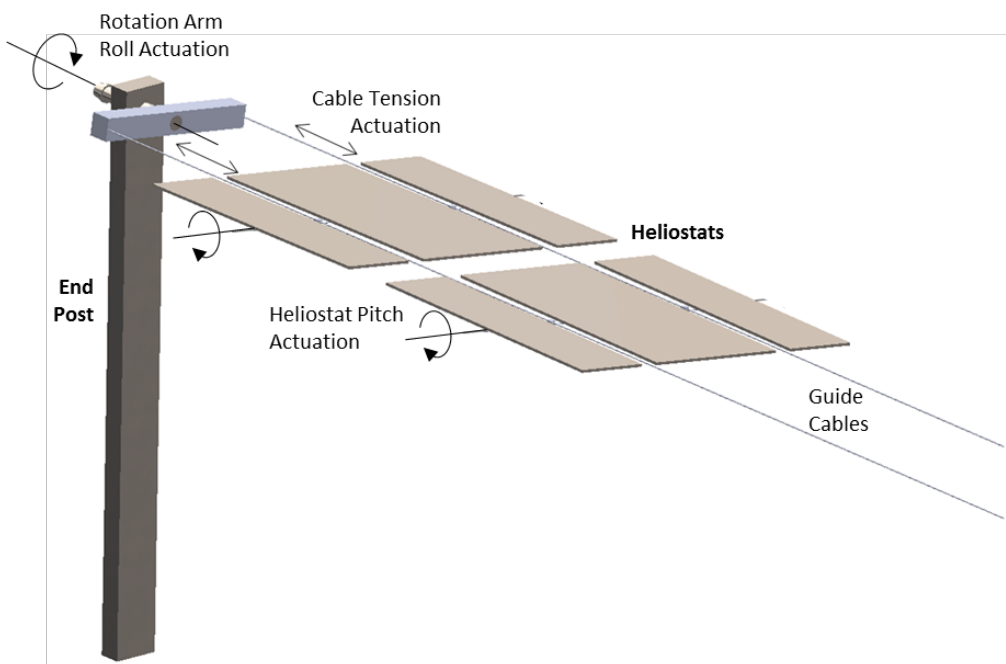
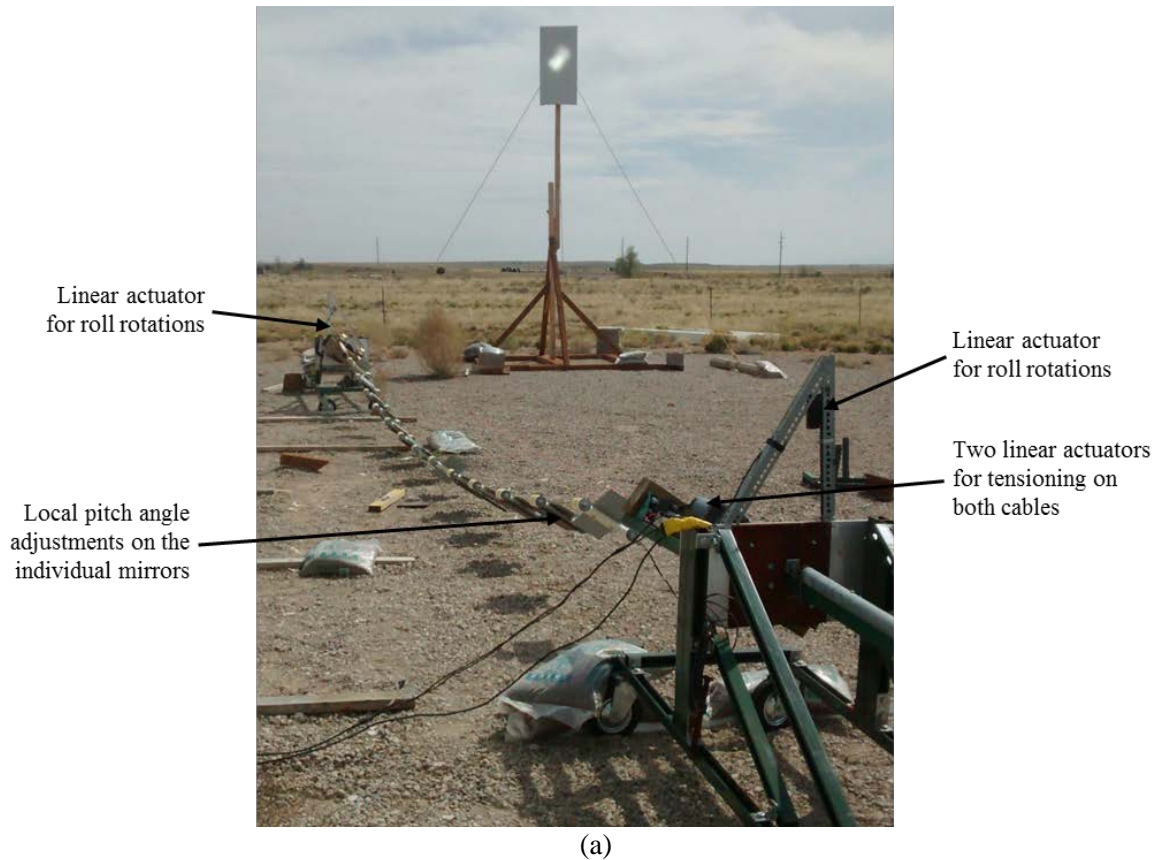




Figure 51. Schematic of actuations on the ganged heliostat that provide the degrees-of-freedom for accurate on-sun tracking. The end post at the other end also has roll actuation.



	Parameter	Specification
	Model	LIN-ACT1-12
	Stroke length	12"
	Power requirements	12 V DC
	Max load capacity	225 lbs.
	Travel speed	10 mm/sec
	Duty cycle	25%
	Shaft diameter	20 mm
	Material	6061 Aluminum

24" weather resistant power cord

(b)

	Parameter	Specification
	Model	HB4500; HB3000
	Max lift capacity	4,500 lbs. / 3,000 lbs.
	Retracted height	31-3/8"
	Vertical travel	18"
	Power requirements	12 V DC
	Outer tube diameter	2 1/4"
	Foot pad diameter	5 1/2"

(c)

Figure 52. (a) First on-sun test of diagonal-span method, Prototype 3, 4/10/2017, 3:21 pm MT 3 of 13 mirrors utilized, both ends and middle. (b) Linear actuator for roll rotations. (c) Linear actuator for cable tensioning.

In the Prototype 3 system, the tracking accuracy was estimated to be about 4 mrad from the on-sun tracking experiments. However, this is with the crude actuations as mentioned. With better control mechanisms the tracking accuracy can easily be improved by 2-3x. A tracking accuracy of 1.65 mrad ($\sim 4/2.5$) was then assumed for the large scale system. If all other slope errors are

kept the same as the baseline case, except for the structural stability, the total optical errors for the ganged heliostat case comes out to 2 mrad, which was used in the power tower plant modeling.

Figure 52 shows testing of Prototype 3 for on-sun tracking while the span was slightly in a diagonal orientation (i.e., span is rotated slightly from its original north-south orientation). Steel weights were removed from the three utilized mirrors (mirrors at the ends at the one in the middle). Similar focus was maintained duration of test, 2:45 pm to 3:45 pm MDT.

Table 13. Optical errors per heliostat tracking axis used in SAM.

Optical Errors	SunShot (mrad)	Ganged Heliostats (mrad)
Mirror Slope Error	1.1	1.1
Canting Error	0.25	0.25
Tracking Error	1.04	1.65
Structural Stability	0	0.25
Total (RSS)	1.53	2.0

There were five tri-axial accelerometers mounted on the mirrors. Figure 53 schematically shows an accelerometer mounted on a mirror with its coordinate axes labeled. Figure 54 shows the mirrors with accelerometers attached. The y-axis of the accelerometers monitored mostly the roll angle movement of the mirror, and the x-axis of the accelerometers measured mostly pitch angle movements. However, the accelerometers did not measure pure roll or pitch angles. Due to the motions of the mirrors, roll motions have a coupled x, y movement of the accelerometers. Similarly, pitch angle movement of the mirrors has coupled x, y accelerometer readings.

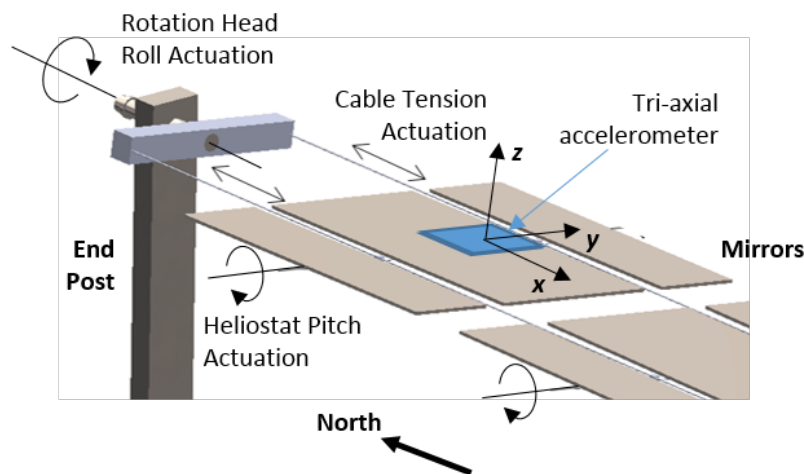


Figure 53. Schematic of a tri-axial accelerometer mounted on a mirror and showing its coordinate axes.



Figure 54. Prototype 2 set up with accelerometers attached to the five mirrors. In the Prototype 3 set up the same mirrors had accelerometers attached to them.

Figure 55 shows the roll angles measured on both rotation arms (on Prototype 2) for on-sun tracking on 02/08/2017. This only shows the roll angles. To put the reflected beams on the target, the pitch angles on the mirrors also need adjustment. We did not have a test setup to measure pure pitch angles on the mirrors. This would require encoders mounted directly on the drive mechanism for pitch motions. As seen in the figure, the roll angle motions follow a smooth second order polynomial very well. This example dataset is specific for the prototype system position relative to the target plate. Other spans in other positions or orientations will have different roll angle dependencies. The idea is then to build up a database of the roll angles for all spans in the field, and either develop a mathematical model or lookup table, which would be the basis for a passive automatic on-sun tracking for the roll angles on the rotation arms. A similar approach can be developed for the local pitch angle adjustments on the individual heliostats.

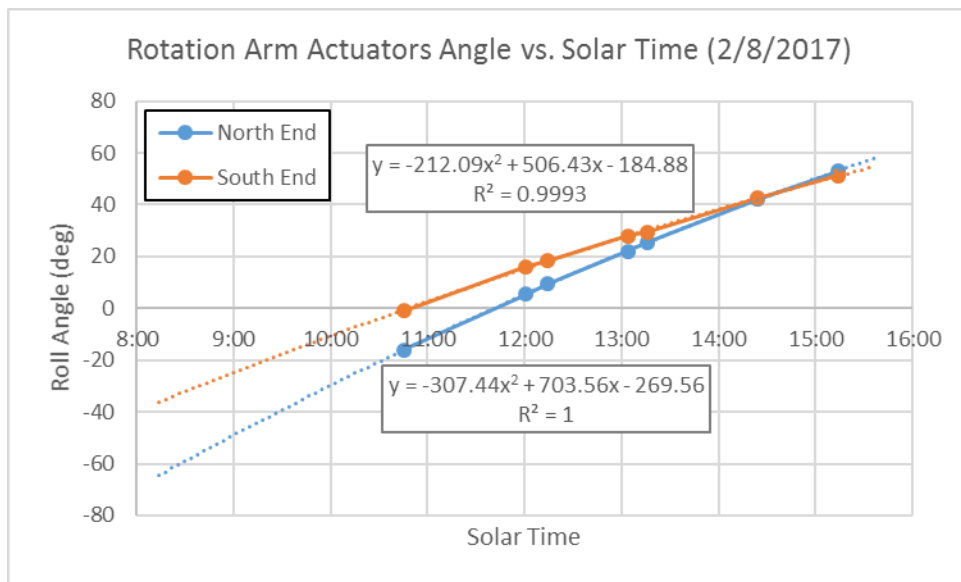


Figure 55. Rotation arms (both ends) roll angles measured with an electronic level for on-sun tracking on 02/08/2017. At 0° roll angle (i.e., horizontal position) rotation arms are leveled to gravity.

Another thing to note is if the heliostat span was directly north of the target stand, at solar noon (12:00) the roll angle on the rotation arms should be zero when the sun is reflected onto the target

plate. However, the prototype span was positioned north and slightly to the east (by about 3 m). This can be seen in Figure 55. The roll angles cross 0° before solar noon.

Figure 56 shows the accelerometer mirror angle measurements on the Prototype 2 set up. The data was collected on 2/8/2017. As mentioned above, the accelerometers angle measurements are coupled between the mirror pitch and roll angles. It is nontrivial to decouple the mirror pitch and roll angles from the accelerometer measurements. This study is left for future work. It is only when both rotation arms are at 0° that the accelerometers x-axis will measure pure mirror pitch angles, which would be the equivalent of elevation angle motion in a conventional heliostat with independent azimuth and elevation motor drives. For increasing rotation arms roll angles, the coupling becomes stronger between the pitch and roll angles. When the rotation arms both reach 90° , then the mirror pitch angles are more equivalent to azimuth angle motion on a conventional heliostat. However, due to the cable dynamics under weight loads, pure azimuth motions may not be achieved.

In Figure 56, the accelerometer angles in x- and y-axes are provided. The five tri-axis accelerometers are attached to five mirrors as shown in Figure 54. Although these measurements couple the mirror pitch and roll angles, the trends in both axes appear to follow smooth curves. A second-order polynomial fit to the Accelerometer #1 data shows a good fit with R^2 equal to 0.9993 in the x-axis and 0.9995 in the y-axis. This informs us the actual mirror pitch and roll angles will also follow smooth curve trends, and mathematical models or lookup tables can be developed for automatic on-sun tracking. Only Accelerometer #4 is showing a non-smooth curve. Around 1:00 pm solar time, the angles shift in both x- and y-axes. The phenomena of the PVC pipes chaffing in Prototype 2 was mentioned above. This is the cause of the angles shift. The PVC pipes that support the mirrors are butted up against each other to provide the spacing between mirrors. The PVC pipes are 2 inches in diameter and slide over the cables that are 3/8-inch thick. Through friction, the butted pipes can stick to each other. As the rotation arms are rotated, the PVC pipes in contact can slip causing a change in mirror angle. This is what happened to the mirror with Accelerometer #4, and this was one reason for development of Prototype 3 where the PVC were cut short and they were no longer in contact.

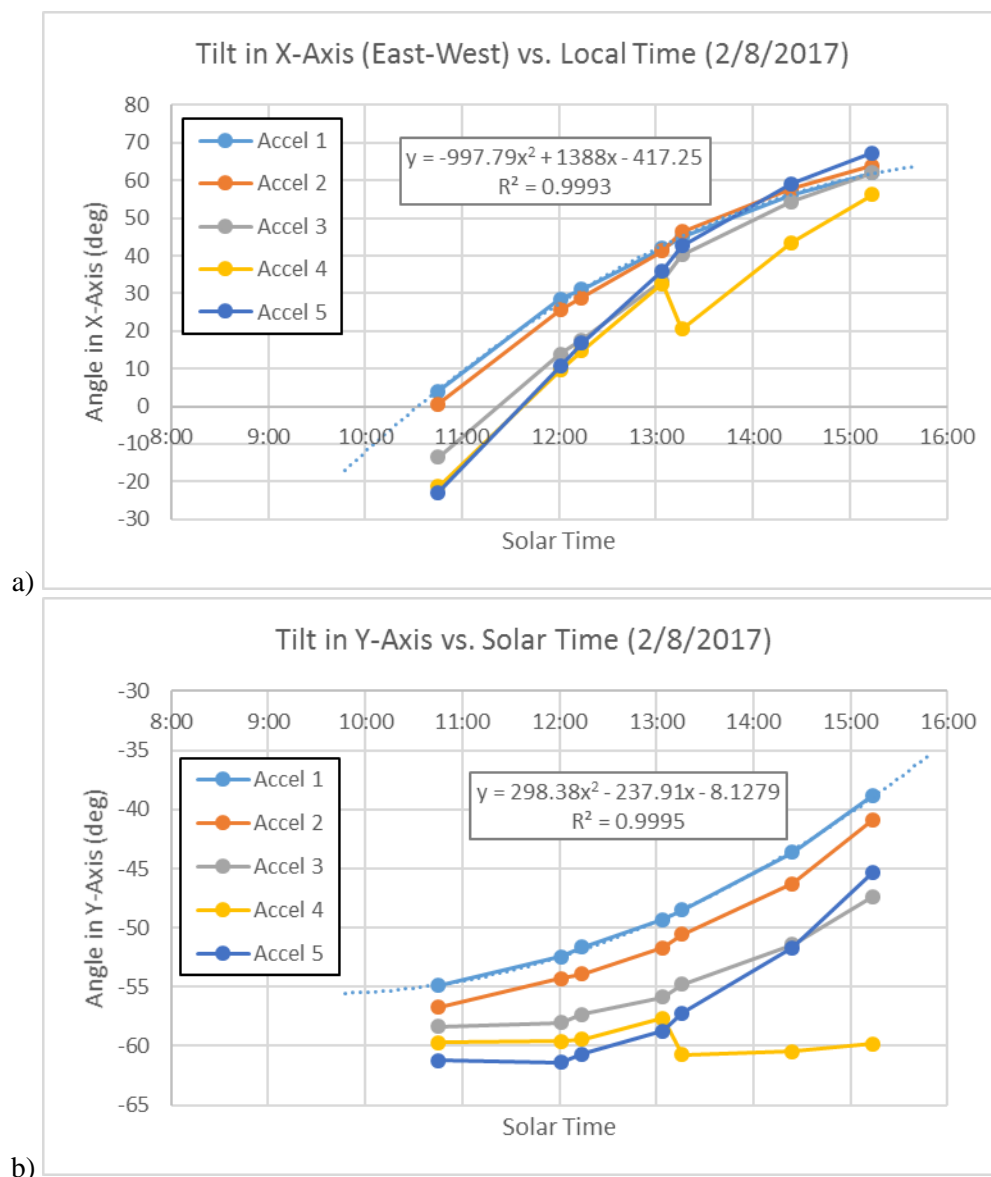


Figure 56. Accelerometer mirror angle measurements on Prototype 2 during on-sun tracking experiments on 2/8/2017.

5.5. Future Work on Tracking Development

Although manual on-sun tracking was demonstrated, demonstration of automatic on-sun tracking is a critical piece in the development of the tensile-based ganged heliostat concept. The development of the tracking algorithms was outside the scope of this work, but the initial work performed here is a start and lays the foundation for future work. In future work, further understanding will be developed for heliostat roll and pitch angle motions. Test setups will include installing encoders on the rotation arms and each heliostat for measuring the angles. The angle data can then be used to develop mathematical models or lookup tables, so the measured angles can provide feedback to the control system for passive automatic on-sun tracking. In addition, drive mechanism must be improved on. The current prototypes used linear actuators and hand

OFFICIAL USE ONLY

adjustments for crude mirror angle adjustments. In the next prototype, better drive mechanisms will provide finer control and improve on the tracking accuracy.

6. COST ANALYSIS OF THE COLLECTOR FIELD (SKYSUN)

This cost study is expected to provide an overview or roadmap directing further research into the ganged heliostat design, construction and operation. Although not exhaustive in scope, salient features are presented and costed. The following analysis was guided in part by the in-depth heliostat cost study [4]. Pricing changes from the 2007 report have been updated with Bureau of Labor Statistics (BLS) values for Consumer Price Index (CPI) and Producer Price Index (PPI) where appropriate. Heliostat production run is assumed to be 50,000 heliostats per annum which in the ganged methodology would produce annually a collecting area capable of supplying a 250 MW sized plant with 4 hours of thermal energy storage. Heliostat design, in keeping with the SAND2007-3293 report [9], is glass on metal style with the substitution of aluminum for steel to reduce heliostat weight.

Table 14. Collecting field characteristics.

Parameter	Value
Ganged Heliostat Solar Field Reflective Area	127,232 m ²
Number of Heliostats	1988
Heliostat Aperture	64 m ²
Tower Height	75 m
Receiver	External
Thermal transfer fluid	Molten Salt
Storage Capacity	4 Hours
Power Capacity	10 MW _e

6.1. Cost Tables

Table 15. Heliostat cost: weight and cost of the heliostat components. Heliostat cost for 1988 heliostats 64 m² each with aluminum frame construction at 16.78 kg/m² or 1074 kg/64 m².

Component	Material	Weight (kg/m ²)	Cost (\$/m ²)	Source
Mirrors	Glass, 3mm	7.58	11.96	SAND2007-3293, CPI 1.17 to 2017
Fasteners/ Adhesive		0.73	1.00	Estimated
Actuators	Linear Actuator 1500 kg Thrust	0.4	1.56	Prototype Actuator 3 years of operation
Mirror Cell	Aluminum 6061	3.37	10.58	SAND2007-3293 steel volume x 1.5 to Alum. Vol., \$1.90/lb
Cross Braces/ Trusses	Aluminum 6061	3.25	10.20	SAND2007-3293 steel volume x 1.5 to Alum. Vol., \$1.90/lb
Axle Clamp/ Bearing	Aluminum 6061	1.45	4.56	SBV Prototype Design
Fabrication	Man-hours/m ² 2.3 MH @ \$25/hr		0.89	SAND2007-3293, CPI 1.17 to 2017, 0.027MH/m ²
Total		16.78	40.75	

In the large-scale design concept, the heliostats are 64 m² each, comprised of four similar sub units, each sub-unit being 2 m x 8 m of reflective surface area. Mirror sub-unit construction is 3 mm thick glass (nominally 1 m x 1 m) upon mirror cell supported by open web joists and cross bracing. Two sub-units are joined for the inner half of the heliostat between cables and one sub-unit each outside of cable. All four sub-units are mounted to an axle located at the heliostat's neutral axis and perpendicular to the supporting cables. The axle is supported by two bearing surfaces, one on each cable. A linear actuator, with 1500 kg thrust, rotates the heliostat about the heliostat's neutral axis. See Figures 57 and 58 below for the design concept.

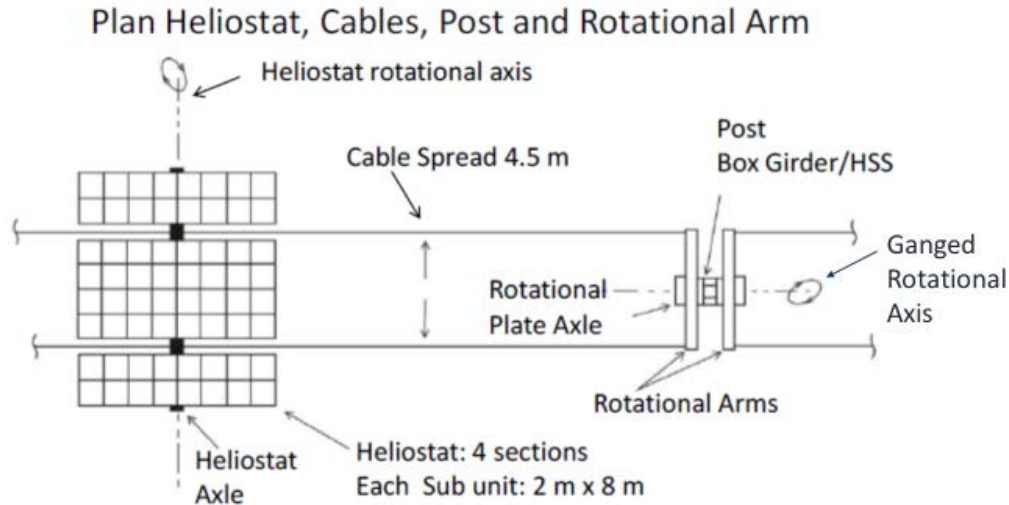


Figure 57. Heliostat plan layout.

Mirror Module Sub Assembly
4 Sub Assemblies comprise
1 Heliostat

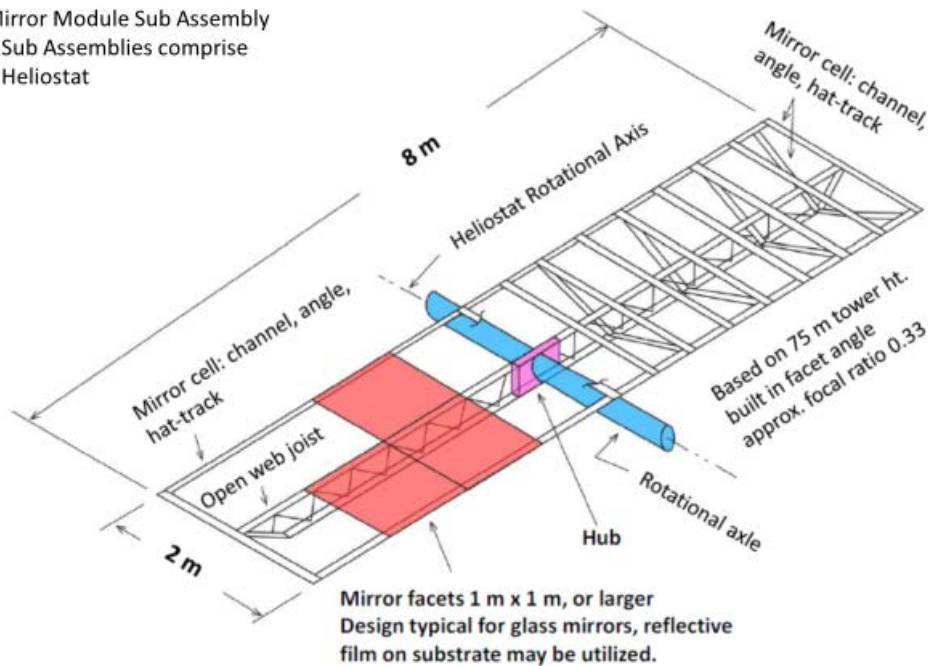


Figure 58. Heliostat sub-assembly.

OFFICIAL USE ONLY

Table 16. Support cable cost: Ganged support cables, 205 spans at 175 m each, 71,750 m of cable various sizes.

Heliostats per Span	Number of Similar Spans	Span Weight (Heliostats and Cables, kg)	Single Cable Max Tension at Mid-Point, Max Rotation 60° (kips)	Cable Dia., 6 x 19, 25 or 26 IWRC (inches)	Safety Factor MBS/Max Tension	West Tech Rigging x 0.85 Bulk Cost per ft. (\$)	Cost per Type of Span (\$)
14	8	17,653	84	1 5/8"	3.14	4.66	43,990
13	28	16,193	77	1 1/2"	3	3.97	131,169
12	24	15,119	72	1 1/2"	3.17	3.97	112,430
11	32	13,691	65	1 3/8"	3	3.29	124,230
10	22	12,617	60	1 3/8"	3.2	3.29	85,408
9	12	11,216	53	1 1/4"	3	2.61	36,958
8	12	10,142	48	1 1/4"	3.3	2.61	36,958
7	46	8,773	42	1 1/8"	3.1	2.27	123,216
6	21	7,436	35	1"	3	1.87	46,339
							740,698
205 Spans cable cost (\$/m²)				5.82			

Table 17. Transverse guying cable cost.

Total Cable Length (ft.)	Cable Diameter (in.)	MBS (kips)	Cable Tension (kips)	Safety Factor	Cost per ft. x 0.9 Bulk	Rigging Multiplier	Total (\$)
38,280	5/8	37	12	3.1	1.16	1.8	79,929
Transverse Guying Cost (\$/m²)				0.63			

OFFICIAL USE ONLY

Table 18. Transverse guying cable cost for varying number of heliostats per span.

Number of Heliostats per Span	Number of posts experiencing this tension	Weight Non-Engineered Steel, lbs. per post assembly x # of posts	Cost in \$ Non-engineered steel Lumia Study Sandia 2007-3293 \$0.72 x PPI to 2017 = \$0.74/lb.	Cost in \$ Eng. steel (400lbs each) Schuff Steel Study - SAND2007-3293 \$1 x 1.17 CPI 2007 to 2017	Cost in \$ Drilled shaft 30" Dia. x X ft \$320/ft Gneiss w/1.25 cu yds concrete (PPI 1.195) x # of posts
14	12	54912	40635	468	24840
13	42	186900	138306	468	86940
12	30	129750	96015	468	62100
11	44	184800	136752	468	91080
10	25	101875	75388	468	51750
9	12	47400	35076	468	21000
8	12	45900	33966	468	21000
7	46	170200	125948	468	80500
6	21	75096	55571	468	36750
		996,833	737,657	4,212	475,960
Cost in \$ Steel placement \$0.50/lb. x 741869 lbs.			370,935		
Cost in \$ Post Assembly Infrastructure Installed			1,588,764		
Total Cost Post Assemblies Installed (\$/m²)			12.49		

The post assembly includes post (11.5 to 12.5 feet depending on foundation depth with 6.5 feet unsupported), drilled shaft 30 inches by 5 to 6 feet depth with concrete fill, rotational arms, cable spreader and bearing plates. The high tension post, supporting 14 heliostats, is comprised of two HSS 12 x 12 x 0.5 inches, 76.1 lbs./feet each as box girder with four plates, each 24 x 36 x 0.5 inches, 125 lbs. each. All are seams welded.

- 1 or 2 (1.6 avg.) rotational arm 10 feet, HSS 14 x 14 x 0.5 inches, 89.16 lbs./feet
- 1 or 2 (1.6 avg.) cable spreader 16.4 feet, HSS 3.5 x 3.5 x 0.375 inches, 14.72 lbs./feet
- 1 rotational arm axle 6 feet x 4" solid 1018 cold finish 43 lbs./feet
- 4 pressure/bearing plates 18 inch diameter x 1.75 inch thick with braces, 161 lbs. each

The post assembly mass decreases incrementally with tension reduction to low tension posts, supporting six heliostats.

OFFICIAL USE ONLY

Table 19. Longitudinal and transverse anchors cost.

Span Longitudinal Anchors				
Number of Heliostats	Tension (kips)	Number Required	Cost per Anchor (\$)	Cost per Type (\$)
12	72	6	4000	24,000
11	65	4	3666	14,664
10	60	8	3333	26,664
9	53	8	3000	24,000
8	48	8	2666	21,328
7	42	27	2333	62,991
6	35	21	2000	42,000
Sub-Total		82		215,647
Transverse Ground Anchors				
	25	12	1500	18,000
Anchor Cost (\$/m²)			1.84	

Longitudinal anchors are drilled shaft with concrete fill about center post. Transverse anchors are “Earth Anchors” mechanically installed.

Table 20. Main cable and heliostat rigging labor.

4 MH @ \$40/hr. per Span	205 Spans	Cost (\$)	Cost (\$/m²)
		32800	0.26
Heliostats: 1 MH/heliostat @ \$35/MH	1988 heliostats	69,580	0.55
Main Cable Rigging Cost (\$/m²)		0.81	

Table 21. Rotational arm actuation cost.

Number of Actuators	Gearing Cost (\$)	Number Required	Rated HP Electric	Motor Cost (\$)	Installation 2.5 MH Each, \$40/hr.	Total Cost (\$)
410	250	79	3/4 hp	110	100	28,519
	250	83	1 hp	160	100	42,330
	250	84	1 1/2 hp	170	100	43,680
						114,529
Rotational Arm Actuation Installed (\$/m²)				0.90		

OFFICIAL USE ONLY

Table 22. Control, active tracking opto-mechanical design by Skysun, LLC.

1988 Units, One per Heliostat	Unit Cost: \$50.00	Cost: \$99,400
Active Tracking Installed (\$/m²)		0.78

Table 23. Dampening, tensile method.

1/4" Cable, 6x19 IWRC	157,167 feet	0.116 lbs./ft.	\$0.40/ft.	Rigging Mult. 1.33	\$ 83,613
Dampening Cost (\$/m²)				0.66	

A series of 1/4-inch cables, 230 m (average) of cable between adjacent spans attached at critical points identified by Sandia.

Table 24. Final installed collecting field estimated cost.

Ganged Heliostat Component	Heliostat Production 50,000 Units/Year (\$/m²)
Heliostat Cost	40.75
Cable Cost for 205 Spans	5.82
Transverse Guying Cost	0.63
Total Cost Post Assemblies Installed	12.49
Anchor Cost	1.84
Main Cable Rigging Cost	0.81
Rotational Arm Actuation Installed Cost	0.90
Active Tracking Installed Cost	0.78
Dampening Cost	0.66
Sub-Total	64.68
Profit/Overhead 15% of Sub-Total	9.70
Ganged Heliostat Collecting Field Installed Cost (\$/m²)	74.38

6.2. Heliostat Weight Reduction and Cost Savings

The tensile nature of the ganged heliostat, especially with the long spans described, make heliostat weight reduction critical to system cost reduction. As mentioned, the above cost analysis based the heliostat design on the well-researched study [9] with the substitution of aluminum for steel. However, significant advancements in mass reduction for heliostats has taken place over the last decade. Reflective film on substrate and suspension designs hold the promise to achieve mirror/cell/support weights much lighter than typical glass on metal designs. A weight reduction of 1/3 for the above described heliostat reduces heliostat weight from 16.78 kg/m² to 11.19 kg/m² and substantially reduces forces acting on the system. Savings are achieved by lowered capacity requirements in both cable strength and post assembly mass, and decreased material weight of the

OFFICIAL USE ONLY

heliostat cell and support structure. The cost implications of such a light weight heliostat are shown in the table below.

Table 25. Cost saving weight reductions and potential cost savings.

Heliostat Mirror/Cell/ Support, 11.19 Kg/m²	Savings % from Baseline	Savings (\$/m²)	Installed Field Cost (\$/m²)
Cable Spans	25%	1.46	
Post Assemblies	20%	2.49	
Heliostats	10%	4.08	
Sub-total		8.03	56.65
Profit/Overhead 15%			8.50
Ganged Heliostat Collecting Field Installed Cost (\$/m²)			65.15

7. PRELIMINARY COMMERCIALIZATION PLAN

As part of this work, Skysun has started developing a commercialization plan, which will evolve as the technology matures. Skysun, LLC is committed to sourcing required materials, components and labor from U.S. suppliers and manufacturers whenever possible. Table 26 shows the materials and components required for developing the ganged heliostat collector field and the labor required for installation.

Table 26. U.S. sourced and manufactured products.

Materials	Components	Labor
Steel, engineered and non-engineered	Actuators, linear and rotary, controlling hardware	All contract and sub-contracted
Cables	Mirrors	Technical/Skilled
Anchors/Ballast	Mirror cells	Installation/Construction

Transition Plan

The current technology has produced an operational prototypes in a relevant environment as a sub-system of a solar power plant. The prototypes were operated, evaluated and improved over the course of twelve months in an exterior environment, subject to seasonal variation and substantial wind loads. Building on this technology level and commercialization path, the next project will produce a lab verified level prototype. The lab verified prototype will also be operated and evaluated in a relevant exterior environment at Sandia NSTTF. Successful deployment of a lab verified prototype will meet baseline requirements necessary for both attractions of strategic industrial partners and placement of the verified prototype sub-system into a demonstration plant. A more detailed 5-10 MW demonstration plant will be described as a project deliverable.

Utility scale CSP plants are capitally intensive undertakings. Attempts to implement a vertically integrated business model would likely prove both time consumptive and capitally intense. Skysun, LLC will likely license its technology and/or develop relationships with industrial players. The project goals of vetting the technology prior to licensing will decrease future partner risk exposure enhancing the probability of adoption. This transition plan targets U.S. corporations or corporations with a substantial U.S. presence. This is likely the more direct path to commercialization.

Targeted Markets for Commercialization

The project verified ganged heliostat will have applications in CSP, specifically in Power Tower style utility power plants, as well as, remote thermal power employed in mining and enhanced oil recovery. Additionally, the ganged heliostat will offer a low cost alternative for both dual-axis PV and CPV tracking, as well as, single-axis PV tracking.

Prospective Partner Organizations

Skysun, LLC has reached out to prominent CSP plant developers: eSolar, BrightSource, and SolarReserve. The Director of Heliostat Design from SolarReserve responded and has expressed the need for improved optical accuracy (~3 mrad), which is one of the goals in future projects.

It should be noted that the ganged heliostat design, in addition to CSP applications, can also align all facets to be perpendicular to the source and maintain that alignment throughout the day,

OFFICIAL USE ONLY

creating applications in both PV and CPV dual axis tracking. This capability broadens marketability to include organizations such as SunEdison, SunPower, First Solar, Emcore, Soitec and Amonix amongst others. Skysun, LLC has already reached out to several of these companies.

Time to Commercialize, Commercial Readiness Level (CRL)

Currently Skysun, LLC's heliostat design is at CRL 4, with one of the project goals being to raise this to a CRL 6 by the end of the next project. A commercially viable product is expected at the completion of the project late in 2018.

Commercial Readiness Factors

Skysun has already identified a partial list of key solar companies and has begun initial communications. No formal agreements have been developed at this time. CSP Solar collecting field design and installation is a young market where proprietary knowledge is both closely held and evolving. PV tracking has similar needs.

After initial communications with solar companies, Skysun has learned that collecting field operators require:

- Reliability: 30+ year life expectancy
- Replicability: tens of thousands plus units
- Optical accuracy: ± 3 mrad
- Survivability: 90 mph wind loads

Approach and Prototype Development

Skysun, LLC's heliostat design gangs many mirrors together and focuses them in unison. The design is inexpensive but capable of complex geometries. The heart of Skysun, LLC's intellectual property covers methodologies that cost-effectively solve tracking challenges, while providing significant installation savings and advantages.

Early small models demonstrated the effectiveness of the Skysun method. Innovation Fund A Grant funds enabled us to demonstrate scalability, performance and survivability with a larger prototype. Roughly half of the grant was expended on prototype construction and testing. The prototype was located on the Lorain County Community College (LCCC) campus for 18 months. Subsequently, we worked with NASA GRC engineers to test an operational real-world design. Although we expected some degradation of accuracy, we found that our design offered similar performance to existing concentrator field designs. Currently the SBV program has shown that Skysun's ganged heliostat methodology merits continued development. Hands on prototype experimentation results have closely agreed with high fidelity modeling bolstering the case for commercialization.

Product Concept and Value Proposition

Our initial product ideas focused on reducing costs for large CSP power plants. The many mirrors, or collecting field, represent the largest sub-system cost of a solar utility power plant – about 40% of capex. These mirrors must move, or track the sun's movement, throughout the day. 73% of the collecting field cost is accounted for by drive unit motors and the mirrors support posts and foundations. Currently, these installations require one post, one foundation and two drive units per heliostat, accounting for approximately 30% of the utility plant's capex. Our design can

OFFICIAL USE ONLY

save substantial capital on these immense installations – our prototype has proven that 24 mirrors can be controlled by only 6 motors all supported by just 2 posts, with minimal performance degradation.

Manufacturing and Scalability

A cost study was performed assuming a mid-size production run of 50,000 heliostat sub-units per annum, each with an area of 64 m². Four such sub-units comprise one heliostat. Each ganged heliostat carries 6 to 14 heliostats depending on blocking and shading constraints.

8. CONCLUSIONS

Sandia National Laboratories has evaluated a novel tensile-based ganged heliostat concept developed by Skysun, LLC. The work was performed under the Small Business Vouchers Pilot program operated by Department of Energy (DOE). It has been reported that the heliostat collector field cost, including installation cost, make up about 40% of the plant capital cost. A reduction in the collector field cost can immediately reduce the plant installed cost and thus lower the levelized cost of electricity (LCOE). The DOE SunShot goal for collector cost is \$75/m², combined with cost/performance targets of the other subsystems reaches a LCOE of \$0.06/kWh. Industry has been working to reduce the collector cost since the inception of the SunShot program in 2011. However, this aggressive cost target has proven difficult to achieve. Current cost estimates on conventional heliostats are between \$120-150/m². This cost seems to have leveled off or near leveling off when conventional heliostats are considered. Ganged heliostats have the advantage of grouping multiple heliostats and have the heliostats share components, specifically the pedestals and rotational drives which are the highest cost components in collector field cost. The reduced number of components can drastically reduce the materials cost and can also simplify the installation, thus reducing the workforce needed for installation. With these advantages, however, ganged heliostats have not yet gained traction for commercial development and deployment. There are several design concept variants of ganged heliostats. Most concepts use linkage bars or chained gears to move the heliostats in angle to perform on-sun tracking. The novel Skysun ganged heliostat concept uses suspended guide cables to support multiple heliostats, thus the cable tensile-based ganged heliostat label. The cables connect to rotation spreader arms that are attached to end posts. In a commercial plant, a single horizontal span of the cables can be 125-200 m long. The heliostat frame is attached a rotational torque tube which is attached to the cables. The rotation arms and the local heliostat pitch angle adjustments provide the angles needed to perform on-sun tracking.

The mechanical and optical performance of the small-scale prototype systems were evaluated. The main questions to address in this project were the survivability of the suspended system under wind loads, performance in windy conditions, on-sun tracking capability, and tracking accuracy estimate, and cost feasibility.

One concern that was consistent was the likelihood of a Tacoma-Narrows bridge type event, where the suspension bridge went into a wind-induced violent oscillation that destroyed the bridge. In reports after the event, it was determined the torsional oscillation became resonant in 80 mph winds, instead of the expected longitudinal oscillation, which the bridge was designed for. The frequency that was excited was around 0.2 Hz. The Prototype 1 small-scale ganged heliostat was well-instrumented with tri-axial accelerometers. The modal/vibrational behavior was evaluated with this setup. The frequency response of the structure was measured after an impulse input using an instrumented hammer and after wind-induced (up to 20 mph) vibrations. The lowest order natural frequency measured was about 1 Hz, above the 0.2 Hz destructive frequency in the Tacoma-Narrows bridge. The measured torsional mode had an even higher frequency, > 2 Hz. Prototype 3 showed similar modal/vibrational behavior. At the small-scale at least, it is unlikely a Tacoma-Narrows bridge event will take place. However, these modal analyses should be repeated at larger prototypes scales and eventually commercial scale where heliostats with larger surface areas may impose different modal behavior due to increased drag and lift on the larger heliostats. From these same analyses, the modes oscillate strong enough to cause sufficient offsets in the mirror positions, which will impact tracking performance. Damping will be needed for heliostat stability especially in windy conditions. From the analyses, damping at strategic locations

were identified; these locations have the highest oscillation amplitudes. With these oscillation amplitudes reduced, stability can be improved.

Manual on-sun tracking was demonstrated on the small-scale prototype setups. The degrees-of-freedom for the mirror angle motions were described in the Optical Analysis section. Since the degrees-of-freedom for the angle motions on a group of heliostats are limited, the on-sun tracking becomes non-trivial. This means a single drive mechanism when adjusted will move all the mirrors at once but at varying angle rates on the mirrors. Tracking algorithms for such tensile ganged heliostats do not exist. The manual tracking was developed from trial and error. The available angle adjustments were varied to get a “feel” for the response on the reflected beams. Each angle adjustment provided a coupled vertical and horizontal response on the reflected beam motion. After developing an understanding of the adjustments, a set of mirrors were put on-sun in an iterative process (i.e., the reflected sunlight from the set of mirrors were directed to a point on the flat target plate). The successful manual on-sun tracking informed us this can be done autonomously. In future work, developing the mathematical algorithms that will be used for autonomous passive on-sun tracking will be addressed. This function is critical for future development of the tensile-based ganged heliostat.

The methodologies described show promise for cost-efficient CSP collector fields that can utilize rough terrain as an advantage by reducing the infrastructure cost of the collecting field. This reduced cost price point is expected to meet or beat the DOE SunShot collecting field goal of \$75/m² installed (see Table 24). Due to shadowing constraints, optimal field size is likely to be up to 25 MW_e given the assumed 75 m tower height. A tower height of 150 m could scale in excess of 100 MW_e. Multiple adjacent fields may be combined. Numerous potential sites exist throughout the high insolation areas of the United States.

The ganged heliostat may be rotated to the vertical for ease of robotic cleaning and water reclamation. The ganged heliostat may also be inverted, with the reflective surface downward, to protect against weather events such as hail. Finally, the ganged heliostat may be secured to protect against high wind conditions.

9. FUTURE WORK

For future work in the near term, we recommend building another prototype at similar scale as the ones studied here or slightly bigger. The main purpose would be to move the technology from its current TRL 4 position to TRL 6. The new prototype must have more certified components, particularly for the tracking drive mechanisms, and mimic more what the large scale system will look like. Encoders must be included for each drive axis to read the angles directly. It would be prudent to demonstrate autonomous passive on-sun tracking. This will involve developing algorithms for daily and annual tracking. A control system (e.g., Arduino based) is needed to initially manually drive the mirrors/heliostats, and eventually use it to autonomously control the heliostats for on-sun tracking after the algorithms are developed. This can be extended to further explore an active tracking system to optimize cable tensioning levels and ganged rotational orientations. Research with the existing prototype demonstrated that alignment of three facets (near middle and end facets), of the 24 facets, was adequate to maintain tensioning levels and ganged orientations when operated with vertical array displacement. Research with the prototype also showed the surface geometry varied smoothly from facet to facet of the reflective surface.

If a larger prototype is built, the study of modal/vibrational behavior under wind load will be repeated to verify if the findings on the small-scale prototype are valid. The new results can be used to update the models and use the models to estimate the behavior of the large-scale system. In addition, wind tunnel testing will be explored particularly on the large scale heliostat in different orientations.

In the current study, it was determined wind induced oscillations would need to be addressed with dampeners. Strategic locations for dampeners were identified, but this was not implemented because it was outside the work scope. In the next prototype system, various damping systems will be explored, and based on performance-cost trade-off one or two system damping will be developed and demonstrated. In addition, further study on wind mitigations methods will be performed such as wind fences and/or vortex shedding. Developing and testing actual wind mitigation hardware will have benefits on stability improvements.

Also in future studies and work, trade-offs between north-south orientation versus east-west orientation will be performed. In addition, algorithms will be developed that optimize the field layout to maximize optical efficiency (i.e., reduce shading and blocking). For the optical modeling, a probabilistic modeling approach can be used. The analysis will determine the sensitivity on heliostat parameters (span length, sag depth), tower height, and day/time. The sensitivity on the parameters will narrow the design space to identify a system with high optical performance and shows economic viability.

Finally, eventually project prototype hardware and hardware connections will be designed as to satisfy wind loading requirements as set for in American Society of Civil Engineers ASCE 7-10.

OFFICIAL USE ONLY

OFFICIAL USE ONLY

REFERENCES

1. REN21 (2015), Renewables 2015: Global Status Report.
2. DOE (2012), SunShot Vision Study.
3. Kolb, G.J., Ho, C.K., Mancini, T.R., & Gary, J.A. (2011), Power Tower Technology Roadmap and Cost Reduction Plan, SAND2011-2419, Sandia National Laboratories, Albuquerque, NM.
4. Kolb, G.J., Davenport, R., Gorman, D., Lumia, R., Thomas, R., & Donnelly, M. (2007), Heliostat cost reduction, Proc. ASME 2007 Energy Sustainability Conference, Long Beach, CA, USA, July 27–30.
5. Industry representatives, personal communications, 2013-2014.
6. Mancini, T.R. (2000), Catalog of Solar Heliostats, SolarPACES No. III-1/00, Albuquerque, NM.
7. Pfahl, A. (2014), Survey of Heliostat Concepts for Cost Reduction, J. Sol. Energy Eng, 136(1), 014501.
8. Blackmon, J.B. (2013), Parametric determination of heliostat minimum cost per unit Area, Solar Energy, vol. 97, pp. 342-349.
9. Kolb, G.J., Jones, S.A., Donnelly, M.W., Gorman, D., Thomas, R., Davenport, R., & Lumia, R. (2007), Heliostat Cost Reduction Study, SAND2007-3293, Sandia National Laboratories, Albuquerque, NM.
10. Ambeck, L., Buck, R., Pfahl, A., Uhlig, R. (2008), Optical Performance and Weight Estimation of a Heliostat with Ganged Facets, J. Sol. Energy Eng 130(1), 011010.
11. Clair, J. (2015), CSP Ganged Heliostat Technologies, Investigations in a Tensile Based Non-imaging System, Academia.edu.
12. Hilton, R.D. (1978), Ganged Heliostat, Patent: US4110010.
13. Mills, D.R. & Schramek, P. (1999), Multi Tower Solar Array (MTSA) with Ganged Heliostats, J. Phys. IV France, 09(PR3), pp. 3-83 – 3-88.
14. Dominguez-Bravo, C.-A., Bode, S.-J., Heiming, G., Richter, P., Carrizosa, E., Fernandez-Cara, E., Frank, M., and Gauche, P. (2015), Field-Design Optimization with Triangular Heliostat Pods, Proc. SolarPACES, Cape Town, South Africa, Oct. 13-16.
15. Yang, M.-G., Chen, Z.-Q., & Hua, X.-G. (2009), A New Two-Node Catenary Cable Element for the Geometrically Non-Linear Analysis of Cable-Supported Structures”, *Proc. IMechE Vol. 224 Part C: J. Mechanical Engineering Science*, DOI: 10.1243/09544062JMES1816.
16. Nayfeh, A.H., & Pai, P.F. (2004), Linear and Nonlinear Structural Mechanics, Wiley.
17. Rega, G. (2004), Nonlinear Vibrations of Suspended Cables – Part I: Modeling and Analysis, Applied Mechanics Review, 57, No. 6, pp. 443–478.
18. Rega, G. (2004), Nonlinear Vibrations of Suspended Cables – Part II: Deterministic Phenomena, Applied Mechanics Review, 57, No. 6, pp. 479–514.
19. Ibrahim, R.A. (2004), Nonlinear Vibrations of Suspended Cables – Part III: Random Excitation and Interaction with Fluid Flow, Applied Mechanics Review, 57, No. 6, pp. 515–549.
20. Irvine, H.M., & Caughey, T.K. (1974), The Linear Theory of Free Vibrations of a Suspended Cable, Proc. Royal Society of London, 341, pp. 299–315, 1074.
21. Arioli, G., & Gazzola, F. (2013), Old and New Explanations of the Tacoma Narrows Bridge Collapse, In Atti XXI Congresso AIMETA, Torino, p. 10.

22. Macdonald, J.H.G. (2016), Multi-Modal Vibration Amplitudes of Taut Inclined Cables Due to Direct and/or Parametric Excitation, *J. of Sound and Vibration*, 363, pp. 473-494.
23. Pinto da Costa, A., Martins, J., Branco, F. & Lilien, J.L. (1996), Oscillations of Bridge Stay Cables Induced by Periodic Motions of Deck and/or Towers, *ASCE J. of Engineering Mechanics*, 122, pp. 613–622.
24. Moya, A. (2013), Modal and Optical Characterization of a Concentrating Solar Heliostat, M.S. Thesis, Univ. of Wisconsin, Madison.
25. Hensley, D.P. & Mayes, R.L. (2006), Extending SMAC to Multiple References, *Proc. 24th International Modal Analysis Conference*, pp 220-230.
26. Akin, J.E. (2010), *Finite Element Analysis Concepts*, SolidWorks. World Scientific Publishing Co Inc.
27. Moya, A. (2016), Memo to K. Armijo and J. Yellowhair, subject: Ganged heliostat modal memo, April.
28. Von Kármán, T. (1911). Über den Mechanismus des Widerstandes, den ein bewegter Körper in einer Flüssigkeit erfährt. *Nachrichten von der Gesellschaft der Wissenschaften zu Göttingen, Mathematisch-Physikalische Klasse*, 1911, 509-517
29. Mayes, R.L. (2005), Memo to T.J. Baca (Org. 1525), dated September 30, 2005, subject: Data Acquisition Uncertainty Procedure.
30. Easton, C., & Blackmon J., Economic implications of a low cost heliostat design. *Sun II*, 1161-1165.
31. Collado, F.J., & Guallar, J. (2009), Design of Solar Tower Plants Heliostat by Heliostat: The Blocking Factor, *Proc. SolarPaces*, Berlin, Germany, Sept. 15-18.
32. Sanchez, M. & Romero, M. (2006), Methodology for Generation of Heliostat Field Layout in Central Receiver Systems Based on Yearly Normalized Energy Surfaces, *Solar Energy*, 80, No. 7, pp. 861-874.
33. Gilman, P., Blair, N., Mehos, M., Christensen, C., Janzou, S., & Cameron, C. (2008), *Solar Advisor Model User Guide for Version 2.0*, NREL/TP-670-43704, National Renewable Energy Laboratory, Golden, CO.
34. Wendelin, T., Dobos, A., & Lewandowski, A. (2013), *SolTrace: A Ray-Tracing Code for Complex Solar Optical System*, NREL/TP-5500-59163, National Renewable Energy Laboratory, Golden, CO.

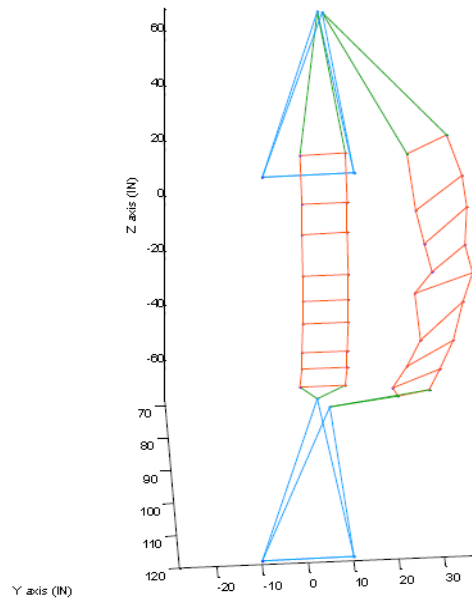
OFFICIAL USE ONLY

OFFICIAL USE ONLY

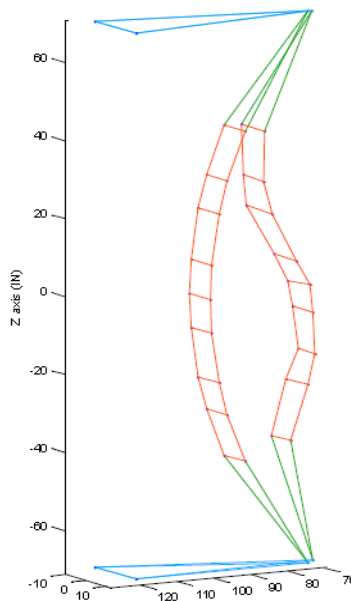
APPENDIX 1: PROTOTYPE 1 MODE SHAPES FROM ANALYTICAL FITS TO EXPERIMENTAL DATA

0° Orientation Mode Shapes

Mode 1
Frequency: 1.193 Hz
Damping: 1.021 %Cr
IDrive T: Generated from reference 3022+



Mode 2
Frequency: 18.15 Hz
Damping: 0.524 %Cr
IDrive T: Generated from reference 3022+

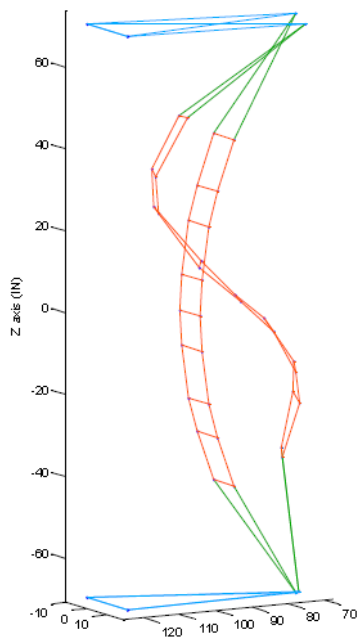


X axis (IN)



OFFICIAL USE ONLY

Mode 3
Frequency: 2.065 Hz
Damping: 0.682 %Cr
IDLine 1: Generated from reference 302X-



<< ? >>

X axis (IN)

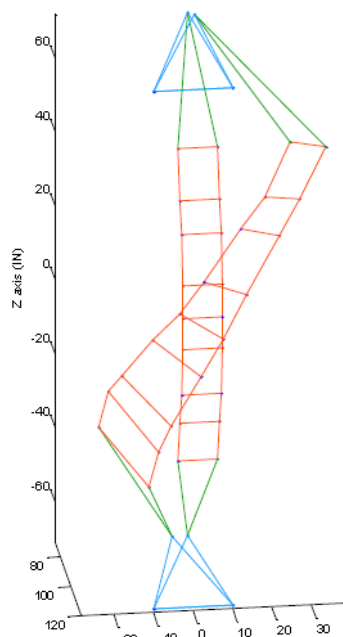
Animate

Stop

Y axis (IN)

Close

Mode 4
Frequency: 2.585 Hz
Damping: 0.459 %Cr
IDLine 1: Generated from reference 302Z+



<< ? >>

Y axis (IN)

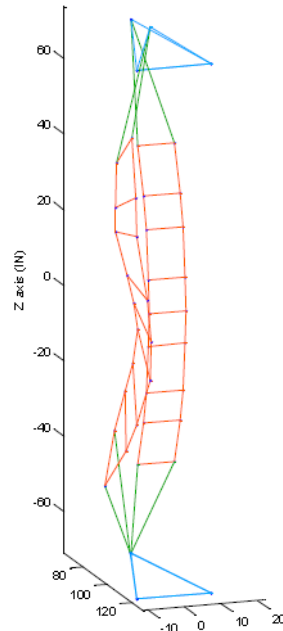
Animate

Stop

Close

OFFICIAL USE ONLY

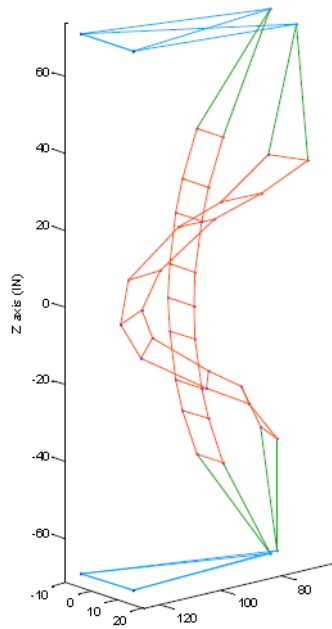
Mode 5
Frequency: 2891 Hz
Damping: 1.874 %Cr
IDLine 1: Generated from Release 3022+



Y axis (IN)



Mode 6
Frequency: 2998 Hz
Damping: 1.743 %Cr
IDLine 1: Generated from Release 3022+

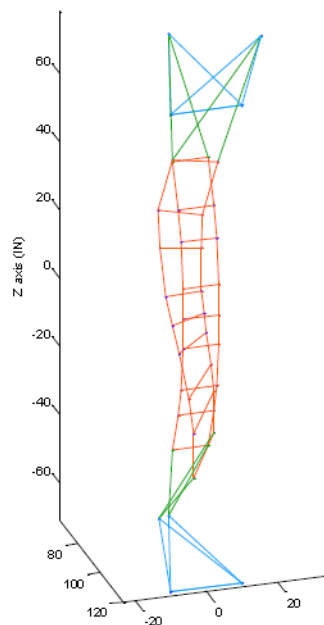


X axis (IN)



OFFICIAL USE ONLY

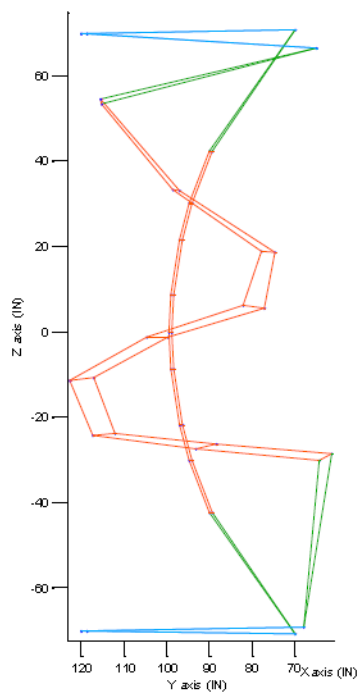
Mode 7
Frequency: 37.13 Hz
Damping: 3.619 %Cr
IDrive 1: Generated from reference 3022+



Y axis (IN)

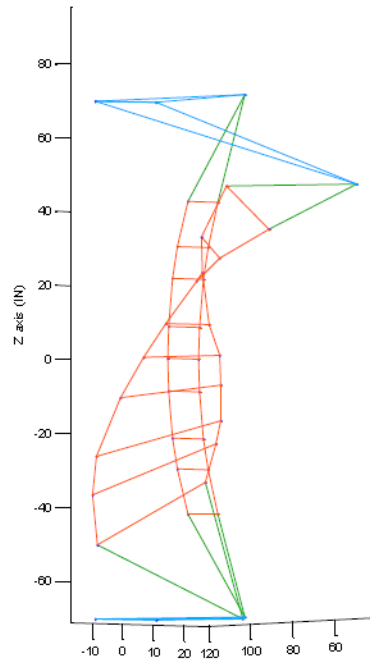


Mode 8
Frequency: 40.69 Hz
Damping: 0.170 %Cr
IDrive 1: Generated from reference 3022-



OFFICIAL USE ONLY

Mode 9
Frequency: 4.429 Hz
Damping: 1.545 %Cr
IDLine 1: Generated from release 302X-



<<

?

>>

X axis (IN)

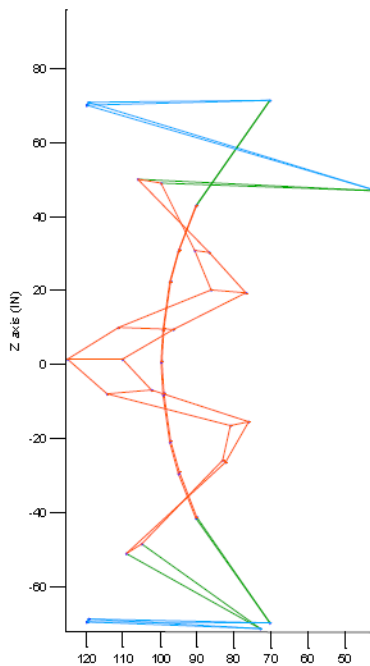
Animate

Stop

Y axis (IN)

Close

Mode 10
Frequency: 5.060 Hz
Damping: 0.288 %Cr
IDLine 1: Generated from release 302X-



<<

?

>>

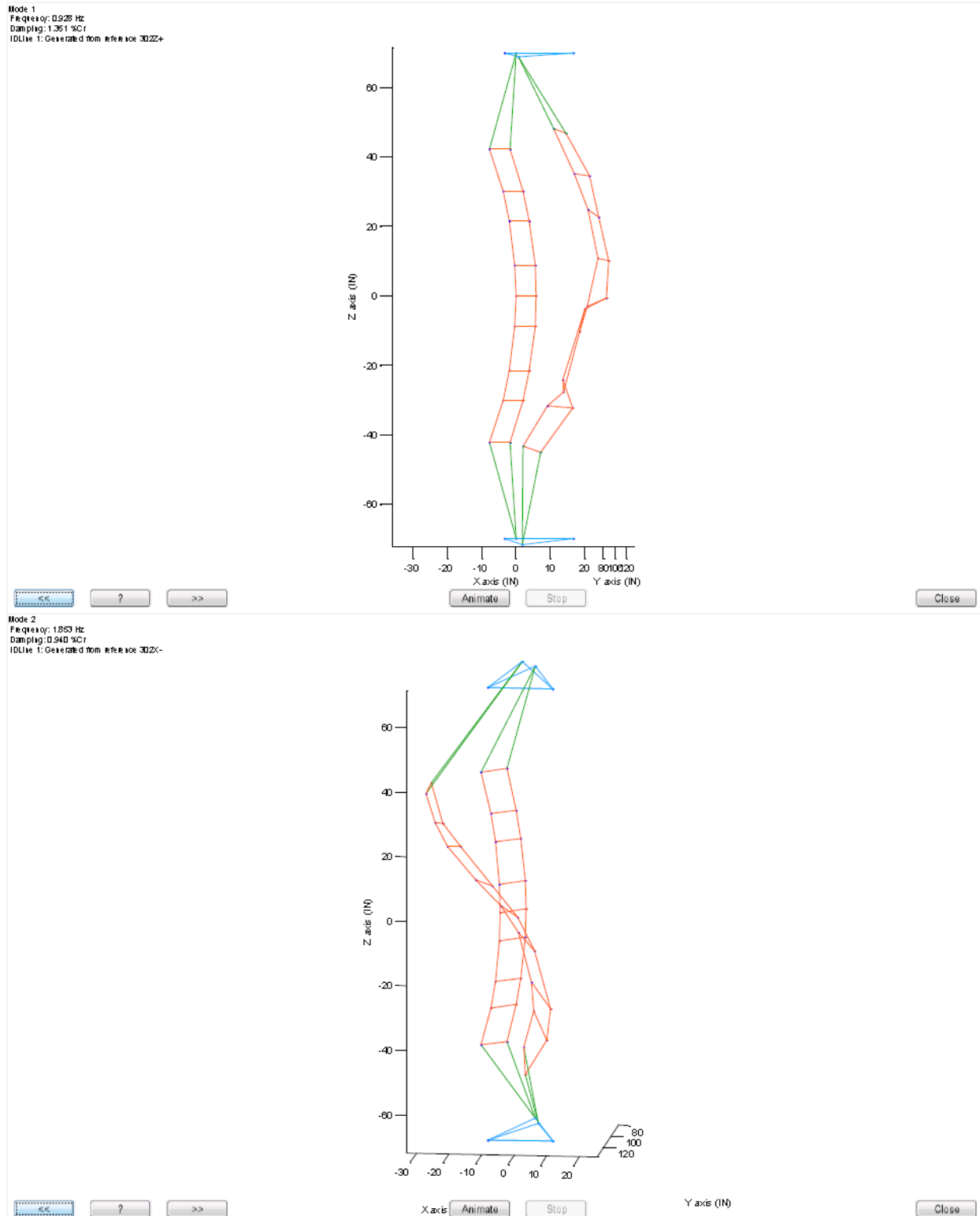
Animate

Stop

X axis (IN)

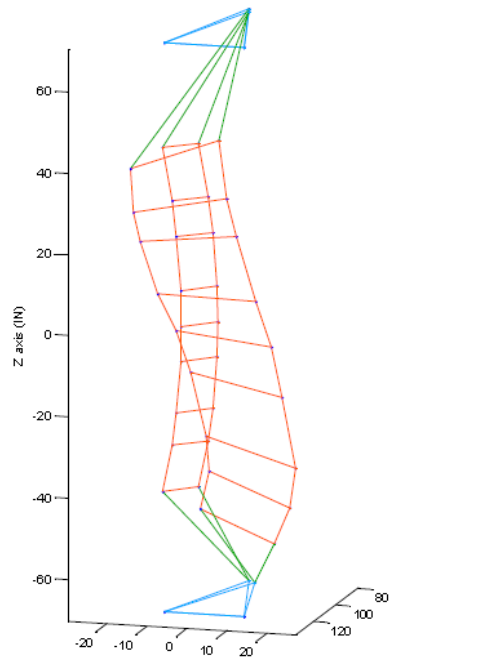
Close

45° Orientation Mode Shapes



OFFICIAL USE ONLY

Mode 3
Frequency: 1.941 Hz
Damping: 0.310 %Cr
IDLine 1: Generated from reference 3DZ2+

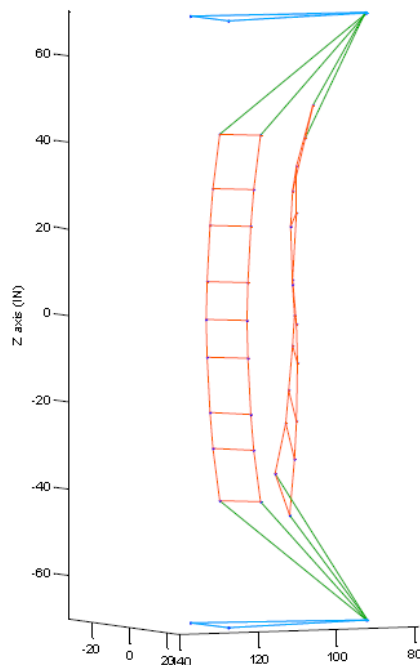


<< ? >>

X axis (IN)

Y axis (IN)

Mode 4
Frequency: 2.068 Hz
Damping: 1.545 %Cr
IDLine 1: Generated from reference 3DZ2+

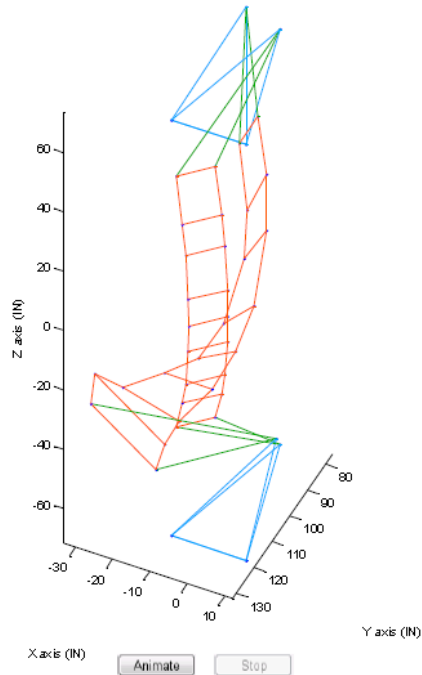


<< ? >>

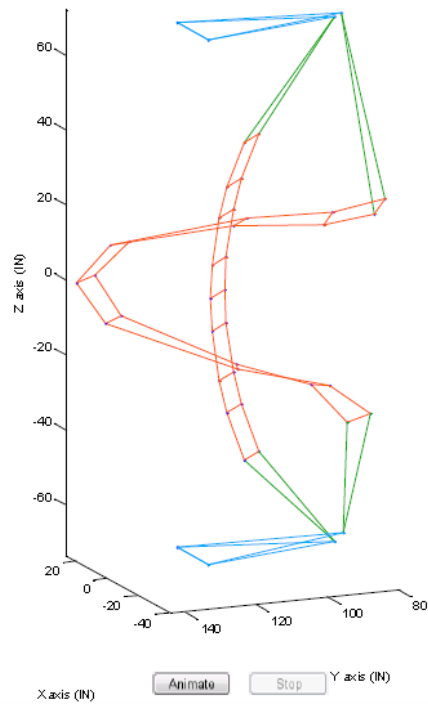
X axis (IN)

OFFICIAL USE ONLY

Mode 5
Frequency: 27.46 Hz
Damping: 0.695 %Cr
IDUte 1: Generated from reference 302<-

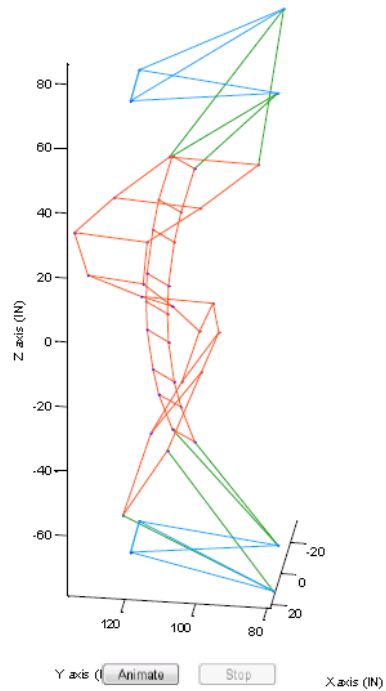


Mode 6
Frequency: 28.62 Hz
Damping: 0.240 %Cr
IDUte 1: Generated from reference 302<-

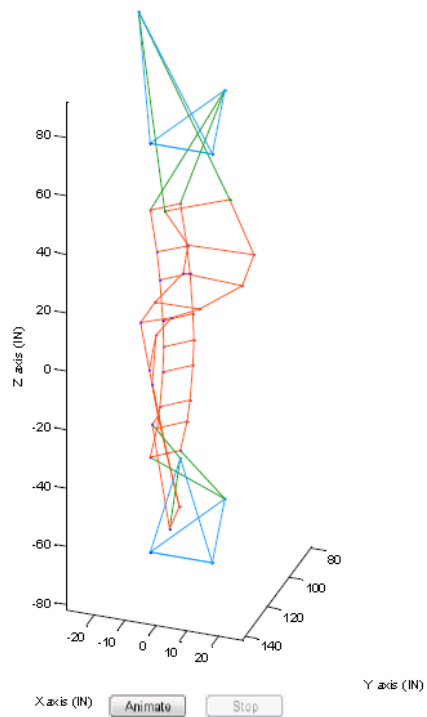


OFFICIAL USE ONLY

Mode 7
Frequency: 3550 Hz
Damping: 2.107 %Cr
IDUte 1: Generated from reference 3DZ2+

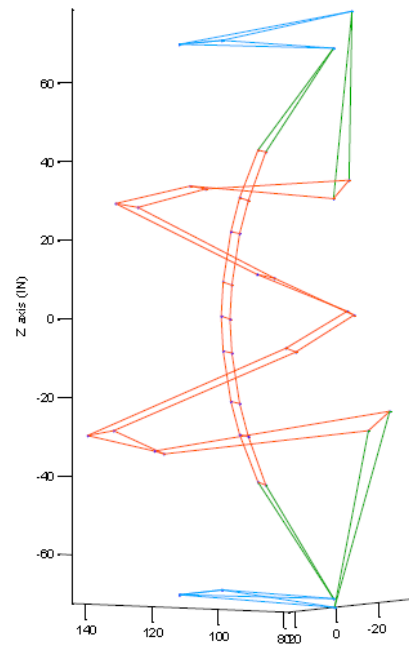


Mode 8
Frequency: 3809 Hz
Damping: 1.248 %Cr
IDUte 1: Generated from reference 3DZ2+



OFFICIAL USE ONLY

Mode 9
Frequency: 4.923 Hz
Damping: 0.366 %Ct
IDrive 1: Generated from reference 302Z+



?

?

>>

Y axis (IN)

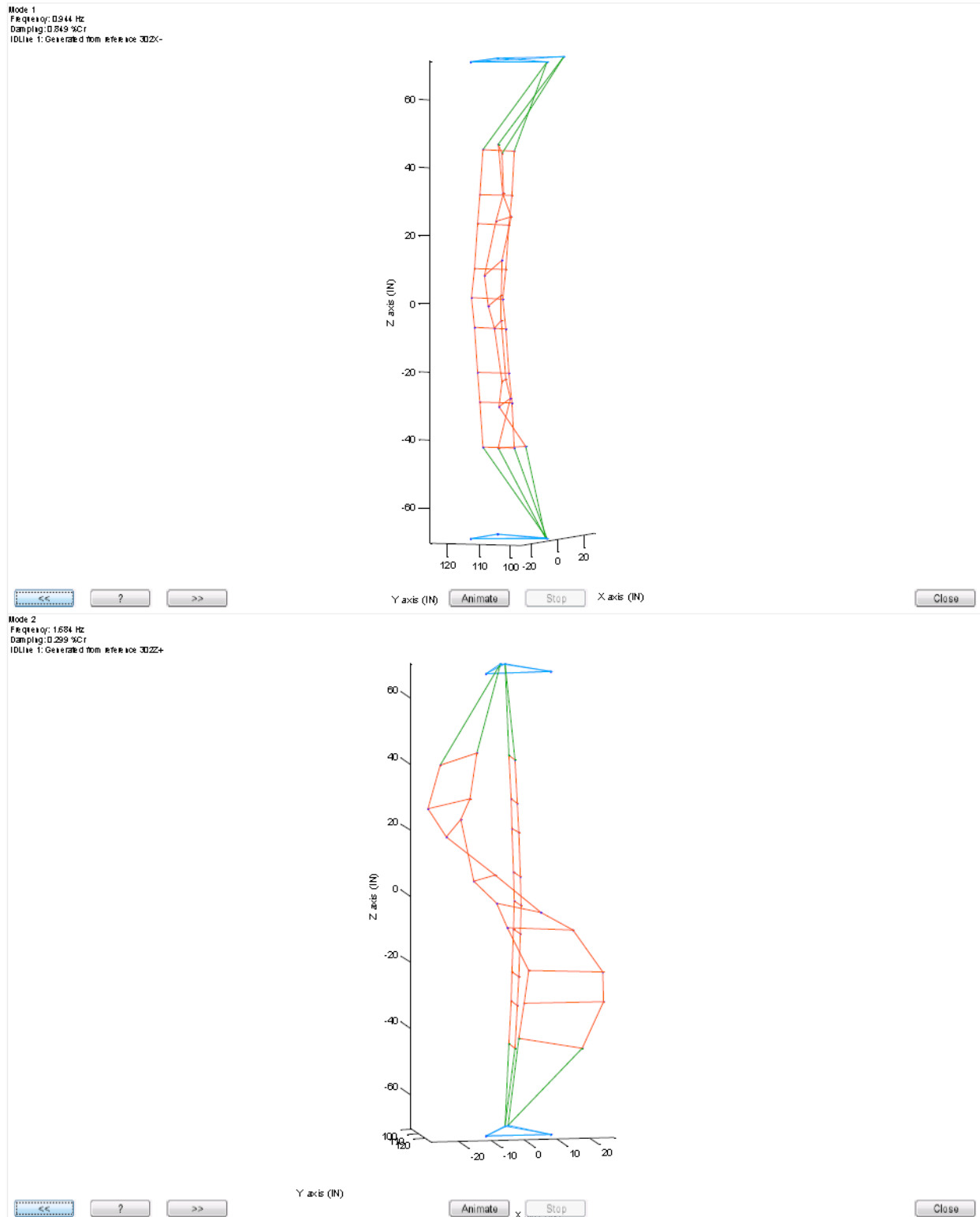
Animate

Stop

X axis (IN)

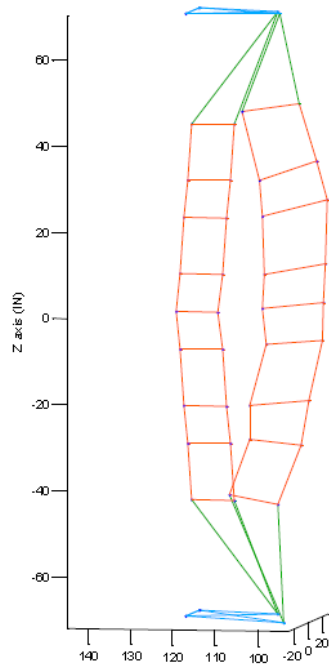
Close

90° Orientation Mode Shapes



OFFICIAL USE ONLY

Mode 3
Frequency: 1.896 Hz
Damping: 1.556 %Cr
IDrive 1: Generated from reference 3DZ2+



<<

?

>>

Y axis (IN)

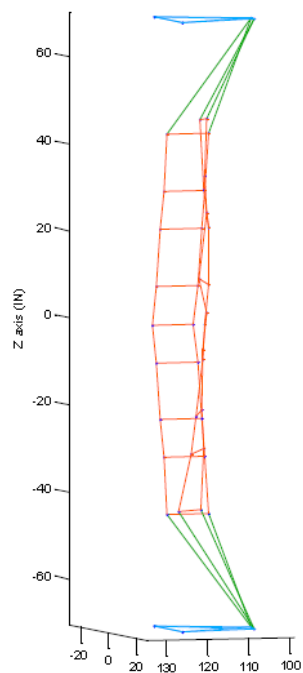
Animate

Stop

X axis (IN)

Close

Mode 4
Frequency: 2.105 Hz
Damping: 3.162 %Cr
IDrive 1: Generated from reference 3DZ2+



<<

?

>>

X axis (IN)

Animate

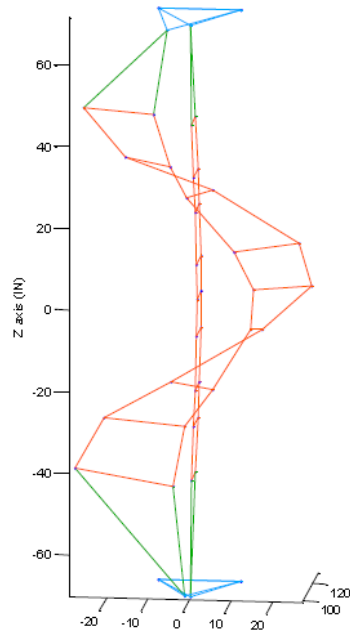
Stop

Y axis (IN)

Close

OFFICIAL USE ONLY

Mode 5
Frequency: 2.476 Hz
Damping: 0.203 %Cr
IDLine 1: Generated from reference 3D2/-

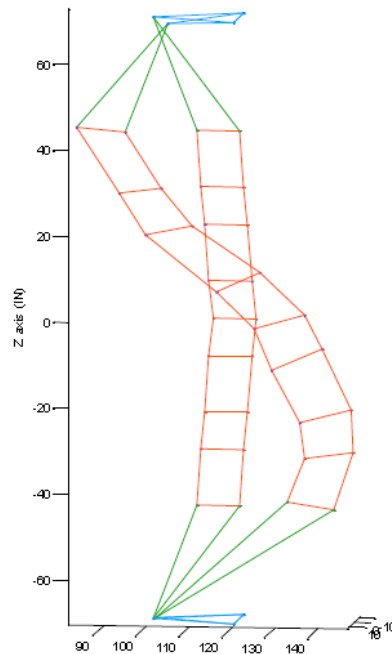


Navigation buttons: <<, ?, >>

Buttons: **Animate**, **Stop**

Buttons: **Close**

Mode 6
Frequency: 2.686 Hz
Damping: 0.263 %Cr
IDLine 1: Generated from reference 3D2/-



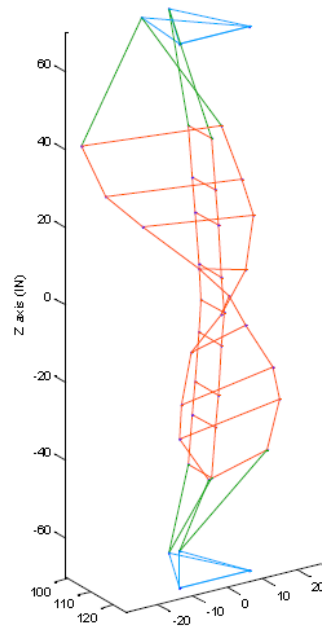
Navigation buttons: <<, ?, >>

Buttons: **Animate**, **Stop**

Buttons: **Close**

OFFICIAL USE ONLY

Mode 7
Frequency: 3216 Hz
Damping: 2.634 %Cr
IDLine 1: Generated from reference 302X-



←←

?

→→

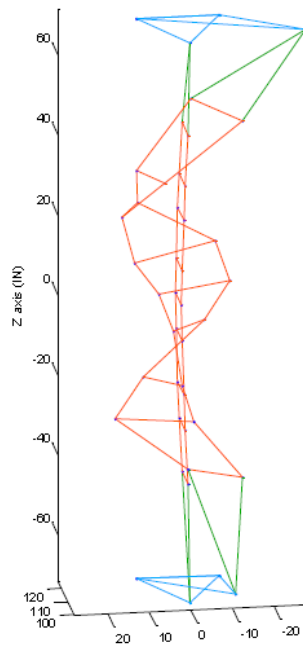
Y axis (IN)

Animate

Stop

Close

Mode 8
Frequency: 3839 Hz
Damping: 1.484 %Cr
IDLine 1: Generated from reference 302Z+



←←

?

→→

Y axis (IN)

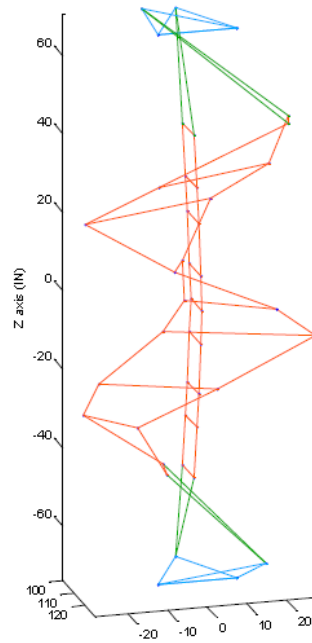
Animate

Stop

Close

OFFICIAL USE ONLY

Mode 9
Frequency: 3934 Hz
Damp ing: 0.481 %Cr
IDUte 1: Generated from reference 3022+



←←

?

→→

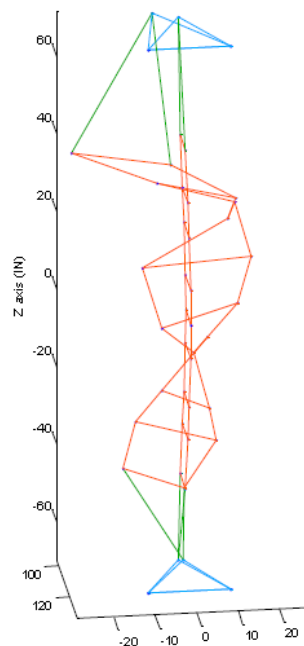
Y axis (IN)

Animate

Stop

Close

Mode 10
Frequency: 4599 Hz
Damp ing: 1.563 %Cr
IDUte 1: Generated from reference 3022+



←←

?

→→

Y axis (IN)

Animate

Stop

Close

OFFICIAL USE ONLY

OFFICIAL USE ONLY

OFFICIAL USE ONLY

DISTRIBUTION

1	Skysun, LLC Attn: Jim Clair 24126 Bruce Road Bay Village, OH 44140		
1	MS1127	Julius Yellowhair	8823
1	MS1127	Kenneth M. Armijo	8823
1	MS1127	Charles E. Andraka	8823
1	MS1127	Jesus D. Ortega	8823
1	MS1127	Paul Gauche	8823
1	MS0899	Technical Library	9536 (electronic copy)

OFFICIAL USE ONLY



Sandia National Laboratories

OFFICIAL USE ONLY